Preparation and Characterization of Spinel-based Interpenetrating Phase Composites via Transformation of 3-D Printed Precursor Shapes

by

Monica Victoria Ramunno

Submitted in Partial Fulfillment of the Requirements

for the Degree of

Master of Science

in the

Chemistry Program

YOUNGSTOWN STATE UNIVERSITY

August 2016

Preparation and Characterization of Spinel-based Interpenetrating Phase Composites via Transformation of 3-D Printed Precursor Shapes

Monica Victoria Ramunno

I hereby release this thesis to the public. I understand that this thesis will be made available from the OhioLINK ETD Center and the Maag Library Circulation Desk for public access. I also authorize the University or other individuals to make copies of this thesis as needed for scholarly research.

Signature: _____

Monica Ramunno, Student Date

Approvals:

_____

Dr. Timothy Wagner, Thesis Advisor Date

_____

Dr. Virgil Solomon, Committee Member Date

_____

Dr. Ruigang Wang, Committee Member Date

_____

Dr. Salvatore A. Sanders, Dean of Graduate Studies Date

Abstract

Interpenetrating phase composites were produced via the reactive metal penetration of ceramic precursor materials. This work was done in collaboration with the TCON division of Fireline, Inc., whose research and development focuses on slip cast silica shapes immersed in molten aluminum. During this process, the silica is transformed into alumina and a network of aluminum channels forms throughout the new ceramic. The interpenetrating nature of these composites yields impressive mechanical and thermal properties, making them valuable materials for ballistic, automotive, and refractory applications. There is new interest, however, in creating composites that contain materials other than alumina as the ceramic phase. The research described in this thesis sought to incorporate magnesium aluminate ($MgAl_2O_4$) and aluminum oxynitride (Al_3O_3N) spinels into IPCs with aluminum. Magnesium titanate and silica in a 2:1 molar ratio was found to produce the $MgAl_2O_4$/Al composite when transformed in an aluminum bath containing 5% silicon by weight. SiAlONs were utilized as potential precursors for the Al_3O_3N/Al materials, though all proved ineffective and the desired IPC was not created.

Ceramic precursor shapes for the $MgAl_2O_4$/Al composites were created via 3-D printing. The effect this process had on final composite microstructure was investigated using scanning electron microscopy and compressive testing. Furthermore, X-ray diffraction and energy dispersive X-ray spectroscopy were utilized extensively for phase identification and material characterization.

Acknowledgements

Not once in high school did I ever think I would become a chemist. Then, even as an undergraduate, I never thought I'd be seeking a Master's degree. Yet, here I am. It's 2016, and I am finally graduating despite my parents' fear that I would become a professional student. They never thought this day would come!

Now that I have completed my degree, there are many people whom I would like to thank. My parents, Mark and Nancy Ramunno, are first. I know that graduate school came as a surprise, but you supported me all the same. Mark, Michael, and Mario… I always wanted sisters, but I'm glad to have you as brothers anyway! Furthermore, I need to thank my grandmother, Carol, and my godparents, Carla and David. I love you all.

Graduate school has proven to be a significant undertaking, and I could not have done it without two of my dearest friends, Gretchen and Heather. Gretchen, in the nine years we have been friends you have encouraged me and all of my dreams, no matter how often they've changed. Even a thousand miles away in Oklahoma, I know I can always count on you. As for Heather, I can't say how glad I am to have met you in physical chemistry. You encouraged me to get my Master's and that has been one of the best experiences of my life. When I think of my favorite times in the last three years, most involve you. I don't know how I got lucky enough to have both of you as friends!

I owe much thanks to the departments of Chemistry and Materials Science, as well as my friends therein. I learned so much from the faculty and staff, and I would like to thank Dr. Virgil Solomon and Dr. Ruigang Wang, in particular, for serving on my committee. As for my friends, you guys helped make some very difficult classes very enjoyable. Victoria, Laurie, Beth, and Caputo, in particular.

Having worked in collaboration with Fireline for two years, I am very thankful for the experience I had with them. I really loved working with the TCON composites, and I learned so much in the process. Thank you Brian Hetzel, in particular, for answering many of my questions, and Eddie Stride for transforming my materials.

One person to whom I owe significant gratitude is Dr. Kyle Myers, my friend and a former student in the Wagner group. Without his help and mentoring, I could not have finished this project or written this thesis. Truly, I owe him a great deal. I thank him for his friendship, and for his advice. Both have proven invaluable.

In reviewing my years at Youngstown State, both as an undergraduate and graduate student, I look most significantly upon my experiences working for Dr. Timothy Wagner. He has, at all times, been the best advisor I could ever have hoped for. I could write multiple pages thanking him for his encouragement and guidance, but it would still feel insufficient. Instead, I will simply say thank you. I hope you know how much I appreciate everything.

Table of Contents

Chapter 1
Interpenetrating Phase Composites

1.1 Introduction

From nature to industry, composite materials are everywhere. When a cement foundation is poured, it is reinforced with rebar. When Kevlar armor is produced, it is strengthened by aramid fibers. And when a tree grows, the very wood of which it is made is a composite of cellulose and lignin. These composites—like all composites—are materials composed of two or more distinct phases. Such constituent phases donate their own unique properties to the whole, producing a material superior to either on their own.

Composites first emerged thousands of years ago, when early civilizations used mud bricks reinforced with straw to build structures. Now, composites are used in ballistic and aerospace applications, to name a few [1, 2]. This shift of simple composites to those that would facilitate man's voyage into space began in the 1940s. As new military technology took hold in the decades surrounding the World Wars, the need for materials of high strength and light weight arose [3]. By using such materials, military vehicles could be adequately reinforced while also increasing their carrying capacity and decreasing overall weight.

In the following decades, the field of composite materials would expand to include those comprised of ceramic and metal. By combining these phases, each very different from the other, an improved class of structural materials was created. These materials saw applications in the automotive and aerospace industries, as well as in ballistic armor due to their low density, high stiffness, strength, and wear resistance [4]. The production of such ceramic-metal composites is the basis of this thesis, and special

attention will be paid to one method in particular: reactive metal penetration as preparation for interpenetrating phase composites.

1.2 Ceramic Matrix Composites

It has been said that need drives innovation, and the need to overcome inherent deficiencies in both ceramics and metals spurred the creation of their composite material. Ceramics, despite their exceptional hardness and temperature resistance, are brittle and do not have great resistance to shock. Metals are incredibly strong and durable, however their weakness lies in their extremely high densities. Furthermore, they fare poorly at high temperatures. As a composite, each phase can contribute its own unique advantages to the new material. For example, improved electrical conductivity and toughness can result from the metal component, whereas low density and thermal stability are supplied by the ceramic [5]. Furthermore, ceramics have greater tolerance than metals to harsh and corrosive environments, whereas the metal's tensile and impact properties greatly exceed those of the ceramic [1, 6]. The primary advantages of this class of composite materials are summarized below [1]:

1. High strength and stiffness
2. Fatigue resistance
3. Impact resistance
4. Thermal Conductivity
5. Corrosion Resistance

These benefits and mechanical properties will be discussed in greater depth in Chapter 3.

To understand the unique advantages of ceramic-metal composites, one must understand composites as a class of materials. Above, it was mentioned that composites

contain a mixture of two or more phases, and these phases can be further classified as the matrix and the reinforcement(s). Typically, the matrix component is continuous, meaning it is one cohesive and wholly-connected phase [1]. The reinforcement is then dispersed throughout this continuous matrix as discrete, isolated particles [4]. The types of materials used greatly affect the properties of the whole, yet the matrix phase nearly always fulfills the same four functions [1]:

1. Binds the reinforcement together.
2. Protects the reinforcement from the environment.
3. Shields the reinforcement from damage during handling.
4. Distributes load to the reinforcement.

Distribution of load from matrix to reinforcement is perhaps the most important aspect of a composite. As a matrix's ability to share the applied load increases, so does strength of the overall material [7]. This is a characteristic of all composites, regardless of their constituent phases, and the ability to transfer load depends on the strength of the interface between components.

The importance of a strong interface between matrix and reinforcement cannot be underestimated, and it has spurred significant interest in how ceramics and metals are joined. One of the simplest methods involves the layering of one to the other using polyurethane glues [2]. In order for the two materials to adhere properly, the adhesive must sufficiently wet both metal and ceramic, a task which often proves difficult [8]. Furthermore, this method fails in terms of size, shape, and thermal expansion [9]. Should there be any curvature or fine detail in one layer, it would have to be exactly and identically matched in the second layer, which is often impractical and unattainable. This

limits layered composites typically to flat plates [2]. For the applications in which ceramic-metal composites are needed, flat plates generally will not suffice. The great differences in thermal expansion also reduce the efficacy of layered composites. Metals are known for their high coefficients of thermal expansion, contrary to their ceramic counterparts [1]. At the high working temperatures of ceramics, the metal component will expand far more than the ceramic, putting stress on the adhesive that binds them. This inevitably leads to creep and structural damage in the material, as well as a decreased lifetime [10]. These failings represent the primary reasons for the popularity of class of materials known as Ceramic Matrix Composites (CMCs).

Like layered composites, CMCs join ceramic and metal, however the method of joining them varies greatly. Here, the ceramic is the continuous matrix phase, while the metal is dispersed as a reinforcement in the form of particles, flakes, continuous fibers, or non-continuous fibers [1, 11]. The morphology of the ceramic can vary, as can relative concentrations of matrix and reinforcements [12]. One thing all CMCs have in common, however, is that neither phase may be soluble in the other [1]. This allows for both ceramic and metal to remain isolated and pure components.

However valuable the CMCs are, they can prove difficult and expensive to produce. Direct sintering proves inadvisable due to the differing thermal properties of ceramic and metal, so other methods have been created [13]. Two of the most popular are as follows:

1. High Pressure Infiltration: Porous ceramic shapes are produced by the sintering of coarse ceramic powders. These shapes are then immersed in a metal bath, and gaseous pressure is applied to the surface of that bath. External pressure forces the

metal inward, and the speed of infiltration is proportional to applied pressure [14, 15]. The produced composite has a metal content that corresponds to the porosity of the original ceramic shape, meaning that greater porosity leads to a greater metal content.

2. Reactive Metal Infiltration: A sacrificial preform is immersed into a bath of molten metal and infiltration occurs as a result of chemical reaction.

The first method allows for greater control over ratio of ceramic to metal, as the second route is, on average, 70% ceramic and 30% metal [12, 16, 17]. Despite this, there is often more control over final microstructure with reactive synthesis [18]. The second method can also produce larger composites because it does not require a high pressure reaction vessel [19]. Most importantly, though the first method is a physical process and the second a chemical, both result in the formation of a type of CMC known as the Interpenetrating Phase Composite (IPC).

1.3 Interpenetrating Phase Composites

Also known as Co-Continuous Ceramic Composites (C^4), IPCs are defined as having both phases continuous and interpenetrating, as opposed to only the matrix like other CMCs [12, 17]. Topologically, each phase of the composite is interconnected, and each is so small that they can only be discerned under the high magnification provided by an electron microscope [4, 5]. In Figure 1.1 below, one can see a scanning electron micrograph of an alumina (Al_2O_3)/aluminum (Al) IPC taken at 1500x magnification [20]. This image shows the interwoven and microscopic nature of the ceramic and metal phases, with ligaments being less than 20 μm wide. Those ligaments represent individual colonies whose growth during synthesis was determined and restricted by impingement

of one onto the other [16]. Such is the interwoven and interpenetrating nature of the ceramic and metal that to separate one from the other would leave two self-supporting foams with open porosity [21]. This stands in stark contrast to layered composites whose phases can be easily isolated and observed by the naked eye.

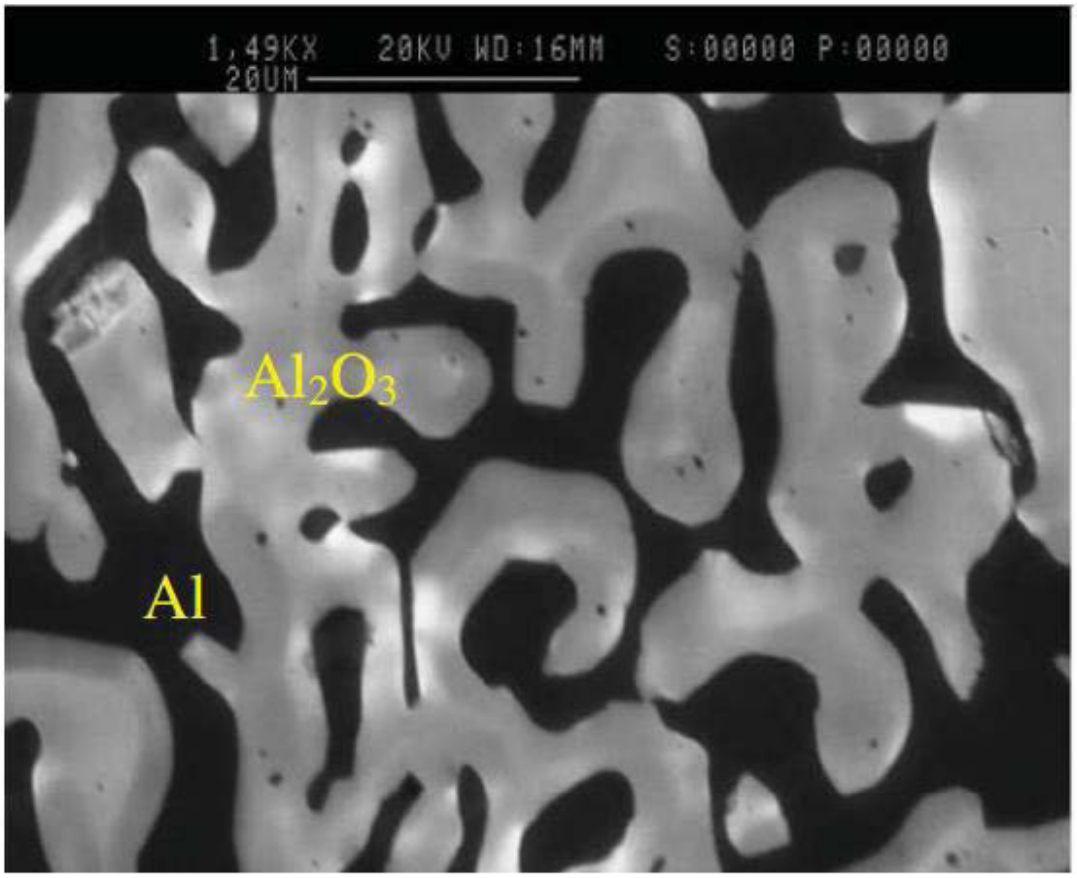

Figure 1.1: Scanning electron microscope image of an aluminum/alumina IPC formed by reactive metal penetration [20].

Reactive Metal Penetration (RMP) is the most popular method for producing interpenetrating phase composites, and the specifics of this technique will be discussed in great detail. In 1955, this near net shape technique was patented using silica (SiO_2) preforms and a metal of choice following Reaction Scheme 1.1 [22]. The metal serves to

reduce the ceramic preform and though aluminum is the most often utilized, other metals such as magnesium, iron, nickel, and titanium can be used successfully [5, 17, 23]. As for the ceramic, it can comprise oxide, carbide, nitride, and boride ceramics [5]. By varying the ceramic and metal phases used, one can produce a great many different ceramic-metal composites.

Reaction Scheme 1.1: $SiO_2 + M \rightarrow MSi^n + MO_x$

Easily the most popular version of reactive metal penetration is the immersion of a silica preform into a molten aluminum (Al) bath. By this method, the silica transforms into alumina (Al_2O_3) and an interpenetrating network of aluminum forms throughout the new ceramic. It is an incredibly reliable synthesis, and provides an excellent example for explaining RMP. The stoichiometry is presented in Reaction Scheme 1.2 [5].

Reaction Scheme 1.2: SiO_2 (*s*) + 4/3Al (*l*) → 2/3Al_2O_3 (*s*) + Si (*s*)

Reaction of the preform begins immediately upon its contact with the molten metal. First, a new oxide layer forms at the interface between the two components to create the reaction front [5]. The newly formed alumina stretches across the exterior of the preform then cracks [17]. Such cracking is a result of the size difference between alumina and silica. The size of the former is smaller than that of the latter, and this decrease in volume causes the alumina to form a porous, cracked skeleton across the exterior of the preform. The net-shape processing benefits of RMP can be attributed to this skeleton. As it forms, a bridging structure is created to compensate for the size decrease between the sacrificial and produced oxide [24]. This skeleton will continue to grow as more cracks form, and any size difference between preform and final product are typically less than 0.5% [17]. It is important to note that the original shape is retained as

well, and that any shrinkage is isotropic and occurs to the same extent in all directions [12]. This is attributed to the silica precursor, both in the formation of the alumina skeleton and that fact that silica serves as the limiting reagent for this process. The silica is the sole source of oxygen in the reaction, meaning that alumina can only form from the oxygen that is freed when the silica is reduced [9]. This forces the reaction to occur according to the strict stoichiometry presented in Reaction Scheme 1.2. A depiction of this silica/aluminum reaction is presented in Figure 1.2.

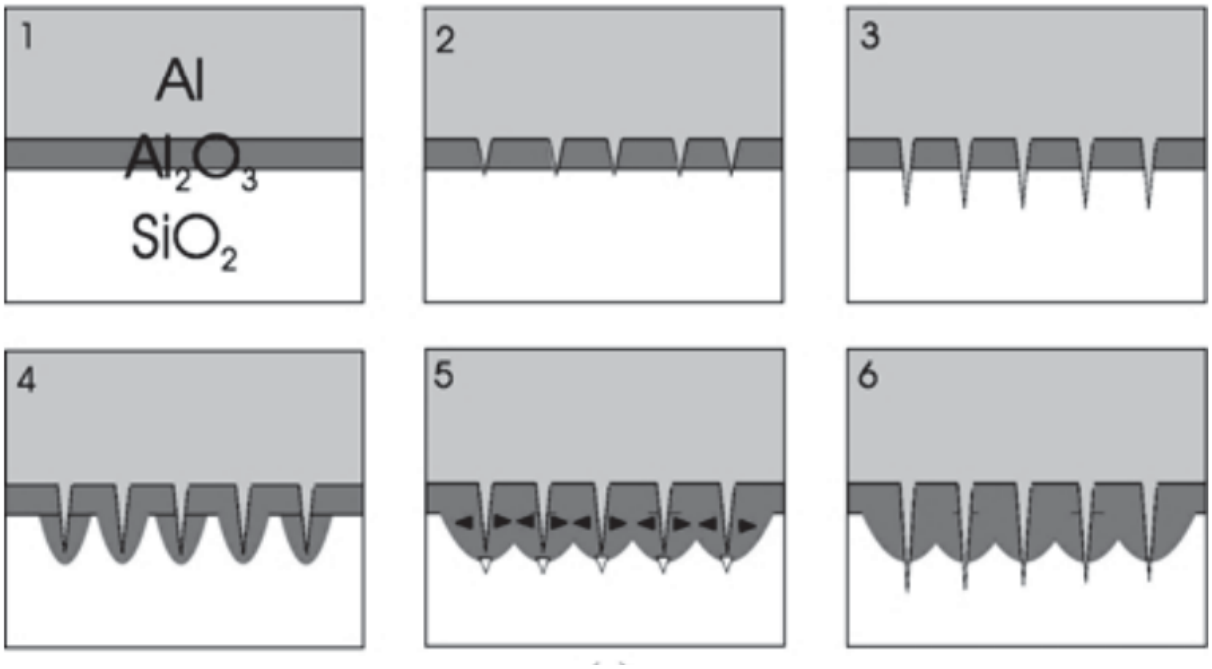

Figure 1.2: Depiction of reactive metal penetration of aluminum in a silica preform [17].

As cracks propagate through the new alumina phase, the interpenetrating metal network is being created. Such cracks form perpendicular to the sample surface, and facilitate aluminum's further infiltration [17]. When wetting is sufficient, this reaction and infiltration are spontaneous such that both further reaction and capillary action are able to pull the metal inward [4, 25]. This allows the reaction front to reach unreacted

silica and transform it into alumina, leaving a mixture of solid reaction products and fluid in its wake [18]. During such a transformation, silicon is being released into the melt. Its diffusion out of the preform and into the metal bath is countered by the diffusion of aluminum inward [24]. Upon complete transformation, the cracks and channels formed in this skeleton hold the aluminum network, which penetrates the entirety of the new ceramic. The scanning electron micrograph in Figure 1.1 represents a composite produced by this reaction of aluminum and silica.

As seen in Figure 1.1, the metal constituent's microstructure looks like a mixture of pools and ligaments [13]. These pools can be attributed to the porosity of the silica preform, where molten metal settled in small holes left open by that porosity. The ligaments represent the channels that opened as the reaction front moved inward and they stretch in the direction of infiltration [17]. As seen in Figure 1.3, whether the preform is immersed or floated has an important impact on growth direction. Those that are floated have one direction of infiltration normal to the surface of the bath. Those that are immersed have multiple growth fronts that converge in the center of the preform. Whether one chooses to immerse or float one's preform is immaterial, however, as the properties of an IPC are typically constant regardless of the direction of infiltration [10].

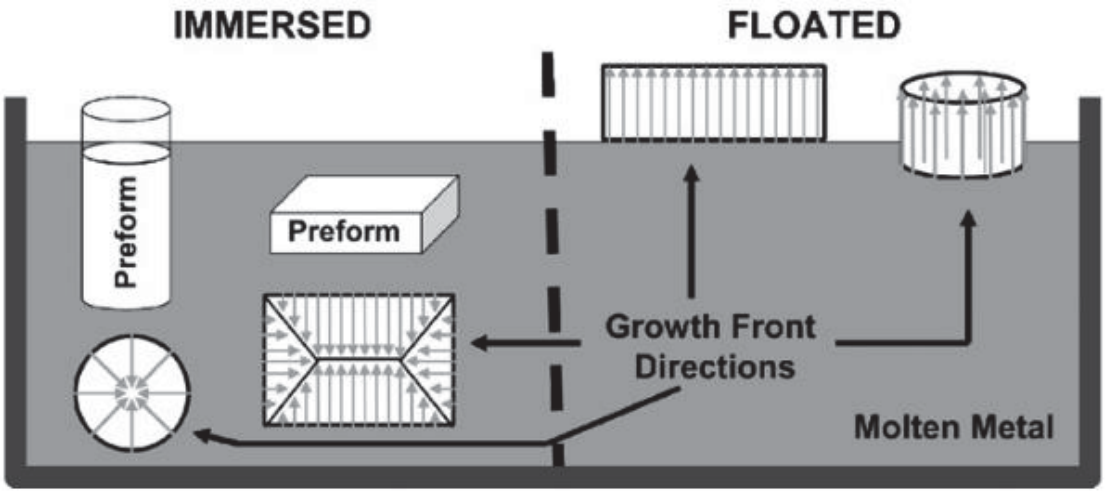

Figure 1.3: Growth directions in reactive metal penetration [10].

Far more important than growth direction is the temperature at which the silica is transformed. Above, it was mentioned that reactive syntheses give better control over final microstructure, and temperature is perhaps the most important aspect in that regard. Though RMP of silica can occur at all temperatures in the range of 800-1200℃, there is no guarantee the desired alumina phase will be produced [17]. For example, θ-Al_2O_3 forms below 1000 ˚C, but the stronger and more desired α-Al_2O_3 occurs above 1000 ˚C. Temperature controls not only composition of particles formed but their size. With increasing temperature, particle size increases and this is evident in Figure 1.4 below [17]. There, one can see scanning electron micrographs taken at the same magnification of C^4 materials produced at 1100 and 1200 ˚C. Notice that the latter produces ligaments of significantly larger diameter. Particle size increase with increasing temperature can also have a detrimental effect on the synthesis of IPCs. It has been discovered that at temperatures above 1300 ˚C, those particles can become so large that they create a barrier to further infiltration [18]. In this case, metal pockets are formed and interpenetrating

channels cannot proceed inward. It is clear that temperature gives one great control over final microstructure.

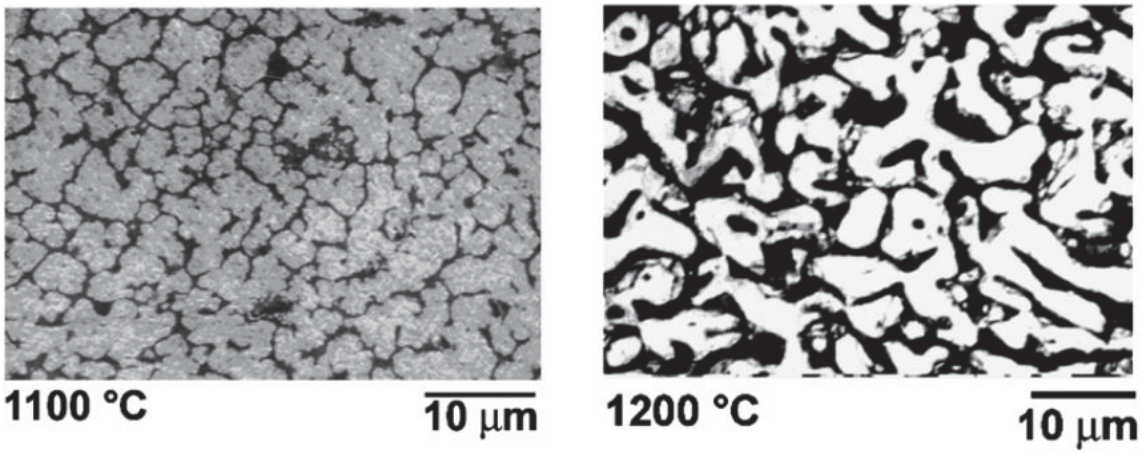

Figure 1.4: Microstructure of C^4 materials produced at 1100 and 1200 ˚C [17].

Microstructure depends not only on immersion method and temperature, for preform composition and density play significant roles as well. Final volume of aluminum in the composite, for example, can be increased by using a more porous preform [4]. IPCs need not contain only one ceramic or one metal as well. Inert ceramic additives may be added to the precursor if they are desired in the final composite. They will have no effect on the reactive metal penetration occurring, and will be bound to the composite by the matrix formed by the produced ceramic to create a multiphase system [20]. Even the melt can contain more than one constituent. Popularly, aluminum-titanium alloys are used for RMP. The aluminum will act as the reductant while the titanium is present only to improve the strength of the final metal layer. This represents one's ability to target specific ceramic and metal phases for specific applications [14]. Different ceramics and metals have drastically different properties within their respective classes, and by choosing materials that meet one's needs one can create composites to one's exact

specifications. The possibilities for tailoring IPCs by combining different ceramics and metals are nearly limitless.

While both the metal of the bath and the ceramic of the preform may vary widely from the oft-used aluminum and silica, it is also expected that the reaction will proceed in a manner identical to the one presented above. This is not to say, however, that any metal or any preform could result in an interpenetrating composite. The criteria for successful RMP must be met, or no reaction will occur.

In 1995, Liu and Koster published a paper outlining the criteria for formation of interpenetrating phase composites made by reactive metal penetration. They proposed the following reaction scheme (1.3) as a method to determine the stoichiometry of RMP utilizing any oxide ceramic and any metal [5]:

Reaction Scheme 1.3: $\frac{2}{y}Sa_xO_y\ (s) + \frac{2p}{q}Me\ (l) \rightarrow \frac{2}{q}Me_pO_q\ (s) + \frac{2x}{y}Sa\ (s \text{ or } l)$

Sa_xO_y: Sacrificial Oxide

Me_pO_q: Produced Oxide

Me: Reactive Metal

Sa: By-Produced Metal

While the stoichiometry of the synthesis can be determined, it is no guarantee that successful RMP will occur. To determine whether the reaction is viable, Liu and Koster further proposed a set of three rules which are as follows:

1. The produced oxide must have a smaller volume than the sacrificial oxide.
2. The produced oxide must be more thermodynamically stable than the sacrificial, with a more negative free energy of formation.

3. The reaction must proceed at a temperature above the melting point of the metal while remaining below the melting point of either oxide [5].

To explain the importance of Rule 1, we can once more look to the example of silica and aluminum. In order for the metal network to form, cracks must from throughout the newly formed ceramic, which can only be done if that ceramic is of a volume smaller than that of the sacrificial oxide. Had the silica been immersed in a melt of molten calcium, for example, the reaction would not have proceeded to completion [5]. While the exterior of the preform would have transformed into calcium oxide (CaO), that oxide would create a barrier to infiltration. This is due to the fact that calcium oxide is of a larger volume than silica. As such, it would not crack as alumina does and no interpenetrating metal network would form. Rather, a hard barrier of CaO would form around the preforms exterior and protect silica from further effects of the reducing metal environment.

To understand Rule 2, one must understand Gibbs Free Energy of formation. It is a quantity that can be used to assess the spontaneity—or lack thereof—for a particular reaction. Determining this is simple, as negative ΔG_f signifies spontaneity, a positive ΔG_f non-spontaneity, and a ΔG_f of zero describing a reaction at equilibrium. In regards to Rule 2, the reaction of the metal with the preform must have a negative free energy such that the reaction will be spontaneous [26]. Upon complete reaction of the preform, Gibbs free energy will become zero and the reaction will be at equilibrium. If the free energy is positive, no reaction will occur.

The relationship between Rules 1 & 2 can be seen in the formation-condition diagram (Figure 1.5). In such, volumes of various ceramics are plotted against the Gibbs

Free energy of those ceramics. In choosing a reactive system, one must identify both the proposed sacrificial and produced materials on the diagram. A reaction is viable when the produced oxide is below and to the left of the sacrificial one. This would mean that the produced oxide has a smaller volume as well as a more negative free energy of formation. As such, Rules 1& 2 would be satisfied.

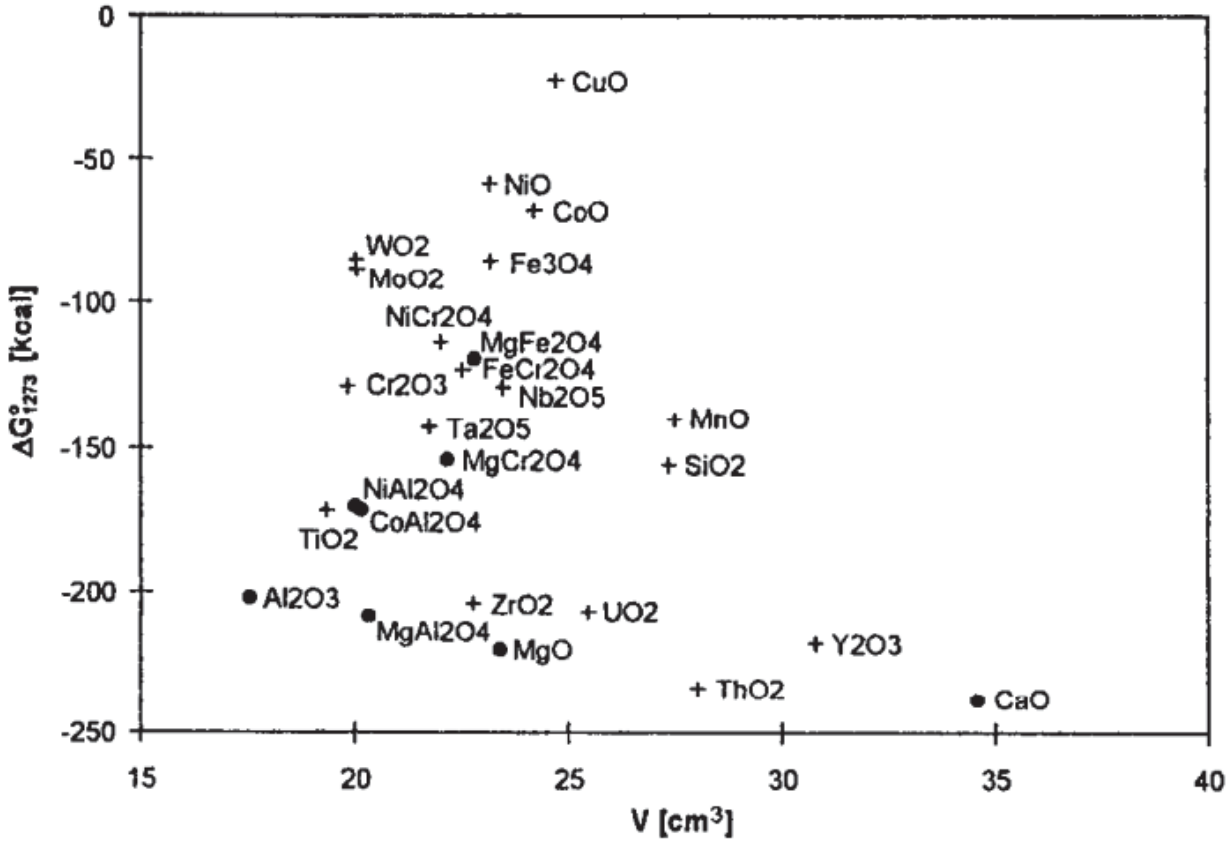

Figure 1.5: Formation-condition diagram for various ceramics at 1273 K [5]

As for the temperature requirements of Rule 3, the reactive metal is only reactive if it's molten, hence the temperature needing to be above the melting point. In terms of the oxides, retention of shape is crucial. Should either melt, the reaction will fail and a composite material that retains the original preform shape will not be made.

If the three rules above are satisfied, one can now concern oneself with the rate at which such a reaction will occur. Growth kinetics for RMP are described as follows:

1. A larger free energy difference between the produced and sacrificial oxides will speed the process.
2. The volume of the metal channels formed is proportional to the difference in volume between the produced and sacrificial oxides.
3. The concentration of by-produced metal in the reactive metal dictates how much of the former can be dissolved into the bath [5].

An increasing difference in free energy increases the spontaneity of the reaction. The increasing difference in size between the sacrificial and produced oxides opens wider channels for the metal to fill. As the channels widen, it increases the speed at which reducing metal can reach the unreacted preform. It also increases the speed at which the by-produced metal can move away from the reaction front and into the bath. The temperature of the bath is also important in this regard, for high temperatures decrease the viscosity of the molten metal and allow quicker infiltration [19]. Capillary action also pulls the metal and reaction front inward, a process which is further improved by better wetting of metal on ceramic [4]. This wetting can also increase spontaneity of the reaction by decreasing the free energy. Furthermore, an increase in the size of the bath lowers overall concentration of by-produced metal while increasing its diffusivity allowing most—if not all—of the metal to dissolve into the melt [18, 22]. All of these factors contribute to the rate and success of RMP, and by taking them into consideration one can better tailor the method to fit one's needs.

To assess the rate determining step of reactive penetration, the synthesis can be divided into three primary steps:

1. Penetration of metal into the reaction front.
2. Reaction of metal with sacrificial preform.
3. Diffusion of by-produced metal into the melt [18].

The slowest of these three represents the rate determining step of the reaction. In this regard, the by-produced metal plays an important role. As the reaction begins, rate is primarily dependent on how fast the metal can reduce silica into alumina [18]. However, should a small metal bath be used the diffusion of silicon outward may slow as reaction time increases. As a result, movement of the reaction front inward will also slow. Such events can lead the RMP to transition from reaction-controlled to diffusion-controlled. Decreasing size of the metal bath can, therefore, lead to longer reaction times in the production of a C^4 material.

Throughout this section, it has been shown that reactive metal penetration is an effective and versatile method for the synthesis of IPCs. In obeying the three rules outlined by Liu and Koster, one can predict with reasonable certainty the products formed by most RMP syntheses. There is one aspect that must still be discussed, however: wettability.

1.4 Wetting

Earlier, it was mentioned that sufficient wetting is necessary for reactive metal penetration. Wetting refers to a liquid's ability to maintain its contact with the surface of a solid, something that is crucial for RMP. If there is insufficient contact between the metal and sacrificial oxide, production of the new oxide will be hindered. As wetting is

also responsible for capillary action, poor wetting will not provide the forces necessary to draw metal into the channels for further penetration.

Wetting is a process that can be divided into two branches: physical and chemical. The former is a non-reactive process that results in a reversible movement of liquid mass through the interface of a solid with little effect on interfacial energies [27].
Van der Waals and dispersion forces provide the necessary energy to drive this wetting [26]. However, in many processes they prove inefficient and external pressure is required to drive metal—which is known for poor wettability—into unreactive ceramics [14, 28].

Wettability in a non-reactive system can be assessed by the contact angle of liquid on solid. Young's Equation (Equation 1.1) relates this contact angle (θ) to the surface energies of the solid-liquid, solid-vapor, and liquid-vapor interfaces (γ_{sl}, γ_{sv}, γ_{lv} respectively) [27, 28].

Equation 1.1: $\cos(\theta) = \frac{\gamma_{sv} - \gamma_{sl}}{\gamma_{lv}}$

$\cos(\theta) > 0$, Wetting

$\cos(\theta) < 0$, Non-Wetting

For a wetting system, meaning $\cos(\theta) > 0$, contact angles may not exceed 90° [14]. A depiction of this contact angle, as well as the three interfaces can be observed in Figure 1.6. The top image represents a wetting system, and the bottom a non-wetting.

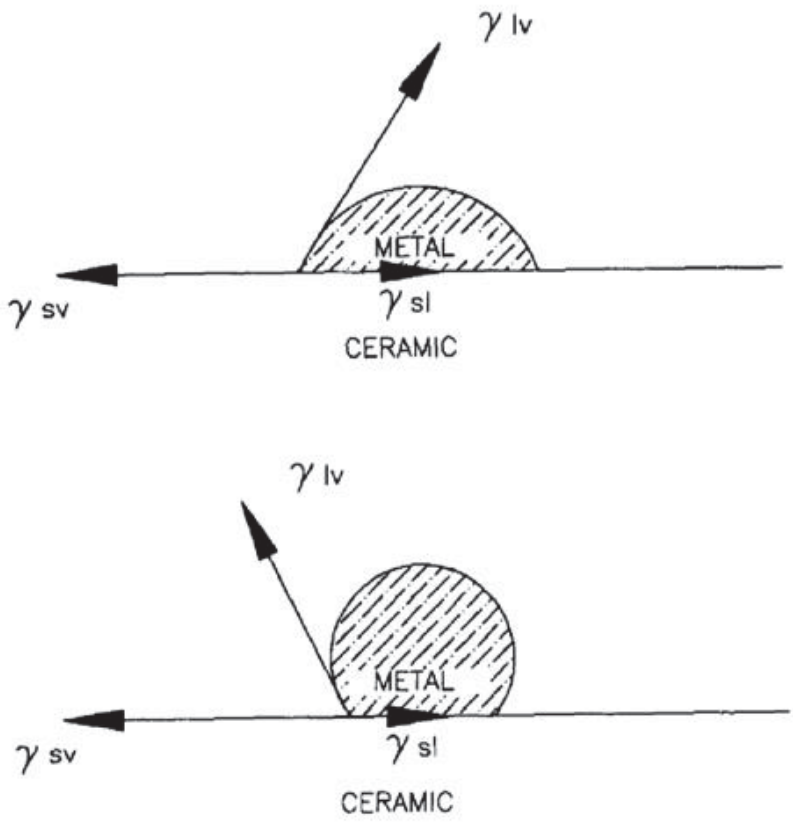

Figure 1.6: Visual representation of good wetting (top) and bad (bottom) [26].

In comparing the top and bottom images, one will notice that the top, with its contact angle less than 90°, has a larger solid-liquid interface. As wettability measures a liquid's ability to maintain contact with a solid, a larger interface means more contact and therefore better wettability.

Should any reaction occur and a new phase is formed at the interface of solid and liquid, the wetting is deemed chemical and reactive. That interfacial reaction is what drives the wetting, as opposed to physical forces, and the stronger the new bonds formed the better the wetting [26, 27, 28]. In such wetting, the effects of chemical interaction are much more significant than physical forces [28]. As a result, chemical wetting is the primary driving method for the wetting of ceramics onto metal [26]. Such wetting can be

improved by increasing temperature and adding inert additives to the metal melt. The contact angle of aluminum on silica, in particular, is lower at higher temps and the reaction proceeds more quickly [29]. Inert additives do not affect contact angle, but rather reduce the interfacial energy between the metal and its substrate [29]. Magnesium and silicon are among the most popular additives in RMP [4]. Small amounts of either may be added to the reactive melt to increase reaction rate without affecting the final composite.

All reactive wetting systems require a negative Gibbs Free Energy (ΔG_w) as a driving force [28, 40]. Reactive wetting will occur until the equilibrium is achieved ($\Delta G_r = 0$) and the chemical potentials of all components are the same in the bulk as well as the interface [28]. In terms of interpenetrating phase composites, reactive wetting will occur until the sacrificial preform is entirely consumed. At that point, the new composite will be fully formed. The case of IPCs is also unique in how contact angle changes as the RMP progresses. To begin, one must consider the ceramic preform to have two components: the surface and the bulk. Free surfaces are technically considered to be defects, as the atoms at the surface are missing half of their nearest neighbors [26]. The result is that the surface has a lower energy than the bulk ceramic, which makes the interfacial reaction fastest when metal contacts a fresh surface [30]. As the reaction front proceeds inward to the bulk, with its higher associated energies, the contact angle increases and slows the reaction.

With sufficient knowledge of wetting and reactive metal penetration, interpenetrating phase composites can be easily produced. The methods used to shape preforms for this technique—as well as the mechanical properties of the final composites—will be discussed in the ensuing chapters.

Chapter 2
Ceramic Shaping Methods

2.1 Introduction

Interpenetrating phase composites prove to be valuable materials in a variety of industries. This value depends not only on their mechanical and thermal properties, but their ability to be produced with desired and varied geometries. Such varied geometries result from the ceramic precursor. The method by which one shapes those ceramic precursors depends on the future IPC's uses and specifications. Considerations such as geometry, density, microstructure, material properties, and cost will determine the shaping method [31]. The last is particularly important as high purity ceramics are often expensive to process [6]. Additionally, one must consider the number of parts to be produced. The image in Figure 2.1 relates complexity of the ceramic shape to the number of parts that can be easily produced [32]. From this diagram, one may determine the shaping method that best fits one's needs.

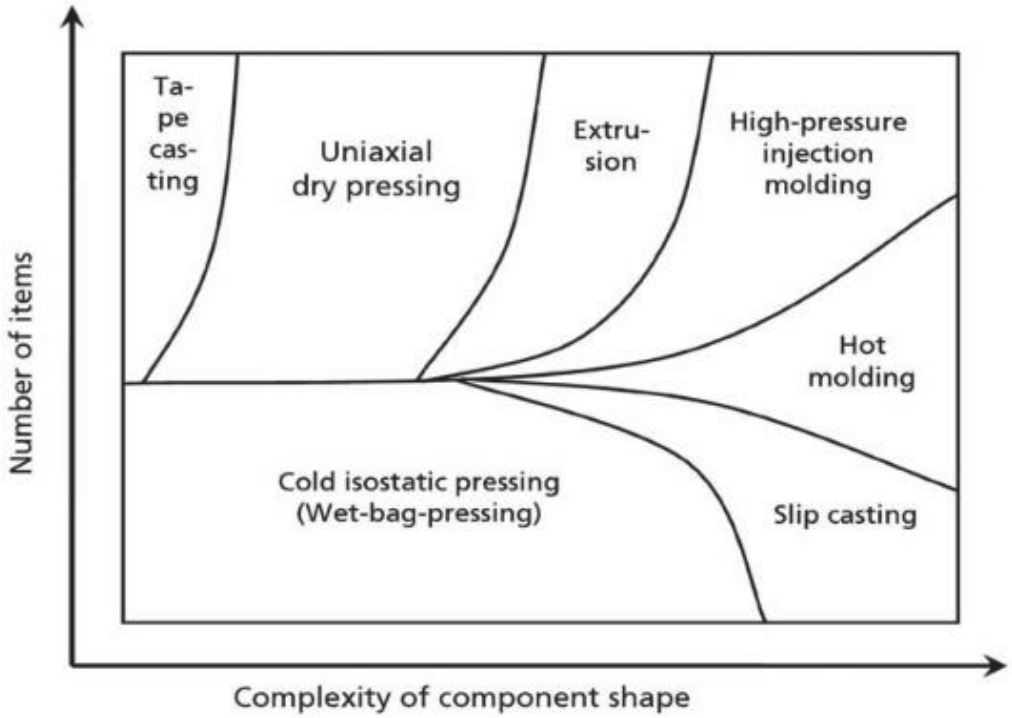

Figure 2.1: Complexity of Ceramic Shape vs. Number of Items to be Produced [32].

The methods by which ceramics are shaped can vary greatly, and each has its own benefits. To look at Figure 2.1 above, one would assume that injection molding is the superior method as it can produce complex shapes in large numbers. This thinking, however, is far too simplistic. Like all other methods, injection molding has its drawbacks. One must understand not only the advantages of a method, but the disadvantages if one hopes to make the best choice for a C^4 precursor. For this reason, a variety of ceramic shaping techniques will be discussed below.

2.2 Ceramic Injection Molding

An overwhelmingly popular method for shaping ceramics is ceramic injection molding (CIM). It is the process of choice for complex shapes as there is no need for additional mechanical treatment after molding [6, 32]. However, this technique cannot

shape raw ceramic powders. A great deal of preparation must occur before any shaping may begin, and post-processing must occur afterward. For this reason, ceramic injection molding has four primary steps [33]:

1. Preparation of Feedstock
2. Injection Molding
3. Debindering
4. Sintering

Each step requires significant care and attention to prevent defects in the produced ceramic shape. When all are done correctly, ceramic injection molding can produce large quantities of strong parts with complex geometries.

The first step of CIM is the production of a feedstock. This is a mixture of ceramic powders and organic additives [32]. The four main additives are as follows: dispersants, binders, plasticizers, and lubricants [32]. As fine ceramic powders flow poorly, dispersants are added to minimize surface tension and agglomeration before the addition of binder [32]. Agglomeration among ceramic particles can cause additive pools to form in the green part, which can lead to defects that are incapable of being later removed [32]. Then, the binder serves to affix the ceramic particles together and form a slurry. Minimum amounts of binder are desired so as to minimize shrinkage in later steps [32]. However, the slurry is often thick and does not flow well. This necessitates the addition of plasticizers to reduce viscosity [32]. Lubricants are the last additive, and their sole purpose is to reduce wear on the injection molding tools [32]. As organic compounds typically have low melting points, the additives are combined with the ceramic powders above their melting points [32]. At these temperatures, the low viscosity allows for

improved mixing and homogeneity in the feedstock. Once sufficiently combined, the mixture is cooled and chopped into pellets [32]. These solid feedstock pellets are the material that will enter the ceramic injection machine.

The ceramic injection molding technique can be divided into two branches: low pressure and high pressure. Low pressure results in less wear on the machine, and has a lower associated cost [32]. It also gives one improved control over feedstock flow, and does not require pelletizing of the feedstock before the molding process can begin. High pressure CIM, on the other hand, is easily automated and is excellent for large scale production [32]. Shapes may be molded in a fraction of the time necessary for low pressure. This results in high pressure CIM being the more popular method. In this branch of CIM, the feedstock is fed into the machine and simultaneously heated and pressurized to a semi-fluid state [32, 33]. This heating is a result of either convection or the friction produced by movement of the machine. A screw or plunger mechanism—the former presented in Figure 2.2—then forces that fluid feedstock into a mold of the desired shape. Though the part has been formed, significant processing is still required.

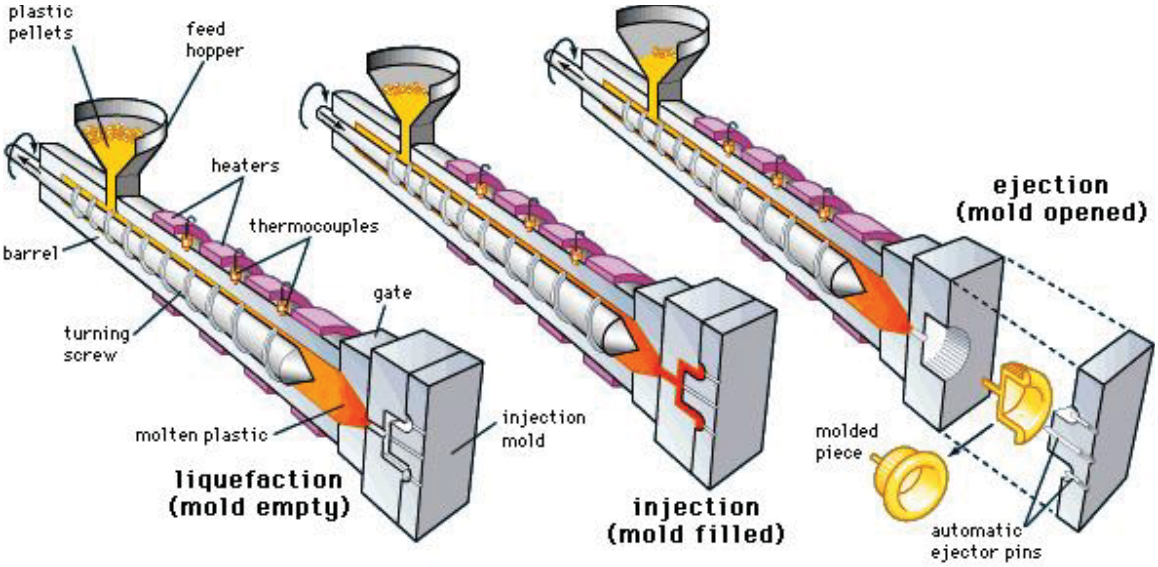

Figure 2.2: Ceramic injection molding process [34].

The third step in injection molding is of critical importance. The molded green bodies may not be sintered directly after shaping, as the organic binder will expand at high temperatures and ruin the shape. For this reason, production of the green bodies must be followed by debindering [33]. CIM has two steps in the debindering process, the first being immersion of the green bodies to remove the soluble component [33]. This is done either in water or other organic solvents, and it allows the soluble components of the binder to dissolve out of the green body [32]. The end result is large pores in the green body that allow easier removal of the other constituent organics with heating. Such heating is a thermal debindering step, which removes the insoluble components through the newly produced pores [33]. This long debindering stage has a propensity for section cracking and results in size limitations for the green body, often a diameter of less than 3 cm [6]. Furthermore, to minimize the risk of the cracking, heating must be carried out over long times [32]. This also minimizes the amount of voids produced. Such attention

to detail is important, particularly because once defects form there is no way to remove them later [32]. As the insoluble components decompose, the brown body is produced.

Sintering of the brown body is the final step in ceramic injection molding. The shrinkage that results typically has a magnitude of 14-22% [32]. Such a change in dimensions must be taken into account when designing the mold. This, coupled with the size limitations mentioned above, means that CIM can only be used to produce shapes with small dimensions. However, complexity and number of parts produced still make this an incredibly valuable method for producing ceramic shapes.

2.3 Slip Casting

An overwhelmingly popular method for the shaping of ceramics is slip casting. By this method, large shapes can be produced with good uniformity throughout [6, 35]. This is especially true in the production of hollow shapes, when wall thickness must be constant across the whole part [36]. Slip casting's ability to produce solid shapes as well further contributes to its popularity.

A wet process, slip casting begins with a slurry. This slurry involves a suspension of ceramic particles, most commonly in water [35]. The suspension, once prepared, is poured into porous molds that draw the water out via capillary action. This forces the ceramic particles against the walls of the mold, and the final shape begins to take form. As this point, it can also be decided whether a solid or hollow shape will be produced. Once a suitably thick layer has formed against the mold walls, the excess suspension can be poured out to leave a hollow shape [35]. This is a variation of slip casting known as drain casting. If the suspension is not poured off, capillary action will continue to pull

water into the mold until a solid shape has formed. An overview of this process is presented in Figure 2.3.

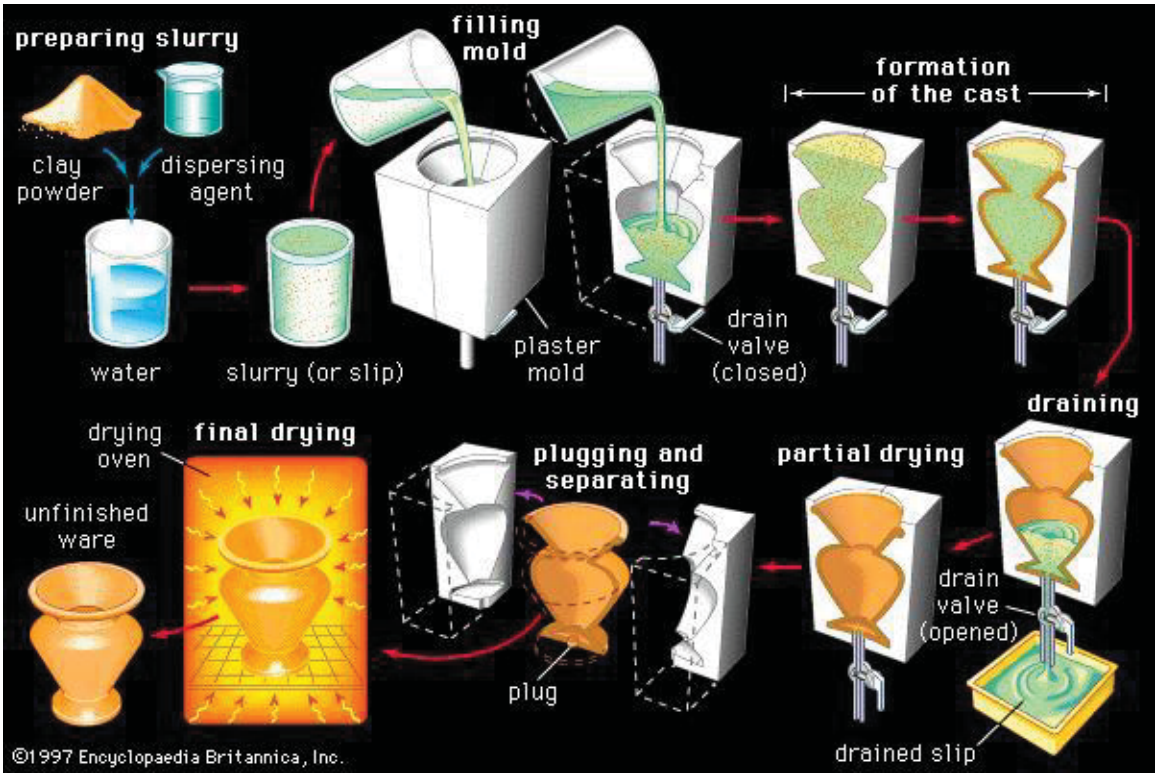

Figure 2.3: Visual depiction of the drain casting process for a clay shape [37].

A second variation of slip casting is pressure slip casting. Whereas standard molds are plaster, the ones used in this method are a porous polymer [35]. External pressure then forces water from the suspension, rather than capillary action. The end result is a much faster drying step, and less time between pouring of the suspension and demolding [35]. However, the faster rate also produces variation in density throughout the final part. This is, of course, undesirable. One must then decide whether time or part density is more important when choosing a branch of slip casting to use.

Having discussed the production of hollow and solid parts, a novel way of producing porous ceramics can be presented. Like pressure slip casting, this method

utilizes a polymer mold. However, this mold is in the shape of a reticulated foam [14]. Once the suspension is poured and the ceramic has dried, the polymer is burnt out at high temperatures [14]. This leaves a final shape that is a negative replica of the mold, with a maximum porosity of ~10% [14]. One's ability to tailor the polymer foam can lead to great diversity in the porous ceramics produced.

When one takes into account the ease and variability of slip casting, its popularity is easily understood. This is not to say, of course, that it has no disadvantages. While plaster molds are cheap and easily produced, they have short lifetimes and must be replaced often [35]. Furthermore, for large scale production, there must exist a great number of molds as well as sufficient space in which to house them [6, 35]. The mold's ability to produce only a single shape at a time, combined with the significant time it requires to dry, is responsible for this. Though, if slip casting suits ones needs the disadvantages can prove minor.

2.4 Gel Casting

Another "wet" shaping technique is gel casting. Its value lies in its ability to combine the benefits of ceramic injection molding and slip casting into one method. Like CIM, gel casting produces complex shapes, yet it uses a low cost molding method akin to slip casting [38]. Shapes produced by this method are notable for their homogeneous density and properties throughout [38]. They surpass slip casted parts in this respect. Such is due to the way in which they are molded.

Before molding, a slurry must be produced. Ceramic particles, organic monomers, and small concentrations of binder are thoroughly combined in an aqueous medium [38]. The slurry is poured into nonporous molds and the mixture is set by gelation with no

removal of liquid [38]. Polymerization is the result of the organic monomers. Vinyl monomers have rapid setting times, so they are popular for use in gel casting though a variety may be used [6]. Typically, there will be one monomer to form a linear chain, and a second to serve as a cross-linker [6]. This forms a cohesive gel of polymer and solvent that entraps the ceramic particles.

In gel casting, shapes are limited only be one's ability to design a mold. As these molds can be made of a variety of materials—metal, glass, wax, or plastic, to name a few—they are often easily and inexpensively produced [6]. Certain materials, however, can impede gelation and must be avoided. Silicone is the major culprit in this respect [38]. Furthermore, as gel cast green parts are weaker than those produced by CIM, the mold must be removed from the shape rather than vice versa [38]. Release agents may be required for this, however they may impede polymerization and must be selected carefully [38]. The combination of mold, additives, and release agents make gel casting an extremely variable process, allowing one to choose each based on their specific needs.

While gel cast green parts are weaker than those produced by CIM, they still exhibit exceptional strength compared to other methods. This high strength allows green parts to be easily machined into a variety of more complex shapes [38]. This machining may occur before or after sintering, however it is easier and less time consuming to machine the green part as opposed to the sintered one [6]. Before any additional machining may occur, however, the shape must be dried.

Drying of green parts represents a significant amount of time in the gel casting process. This step must occur at controlled temperatures and humidity, such that removal of water does not damage the part or alter its shape [38]. Slight shrinkage from removal

of water occurs during the first part of drying, but that shrinkage ceases early and from then on the drying process can be sped up [6]. Once the water is removed, the part can move straight to the sintering step. The polymer is removed by pyrolysis at these high temperatures, and the binder is also burned out at this point [6]. The lack of a separate debindering step is a result of the low content of organic binder, typically less than ~4% by weight [38]. Such a low additive content makes this a near net shape process [6]. Gel casting is one of the few ceramic shaping techniques to exhibit this trait, and it is yet another incentive for choosing this method.

2.5 Tape Casting

As the name suggests, tape casting is a method for producing ceramic tapes. It is particularly useful for production of thin ceramic parts, and can produce shapes with thickness as small as 100 μm [39]. These tapes are pliable and have large surface area to volume ratios [40]. Once produced, they can serve as stackable lamina or be further detailed by punching, milling, or cutting [39, 40]. So, even though the original tape has limited dimensions, a variety of shapes may still be produced.

Tape casting occurs across multiple steps, the first being production of a slurry. Ceramic particles are suspended in water or organic solvents and combined with binders, dispersants, and plasticizers [39]. To produce such thin tapes, ceramics with fine particle size must be used. However, their large surface area to volume ratio results in electrostatic repulsive forces that diminish flowability. The dispersant remedies this by coating the particles and allowing those fine particles to move over one another with greater ease [39]. High binder concentrations allow for a flexible tape that retains its shape even after solvent has evaporated [39, 40]. Plasticizers then soften the binder and

increase the tapes strength upon drying [39]. This allows it to be easily handled and machined. This high content of organic additives will heavily affect later steps in the tape casting process.

Once the slurry is created, casting of the tapes may begin. This can occur in one of two ways, the first being the spreading of the slurry onto a stationary surface [39]. From this point, a mobile blade will move over the slurry and spread it. The blade's height above the surface determines the thickness of the tape being produced. The second method is merely a reversal of the first. A blade is held stationary, and a mobile surface covered in the ceramic slurry moves below it [39]. Identical tapes may be produced from either method, and the latter variation is presented in Figure 2.4.

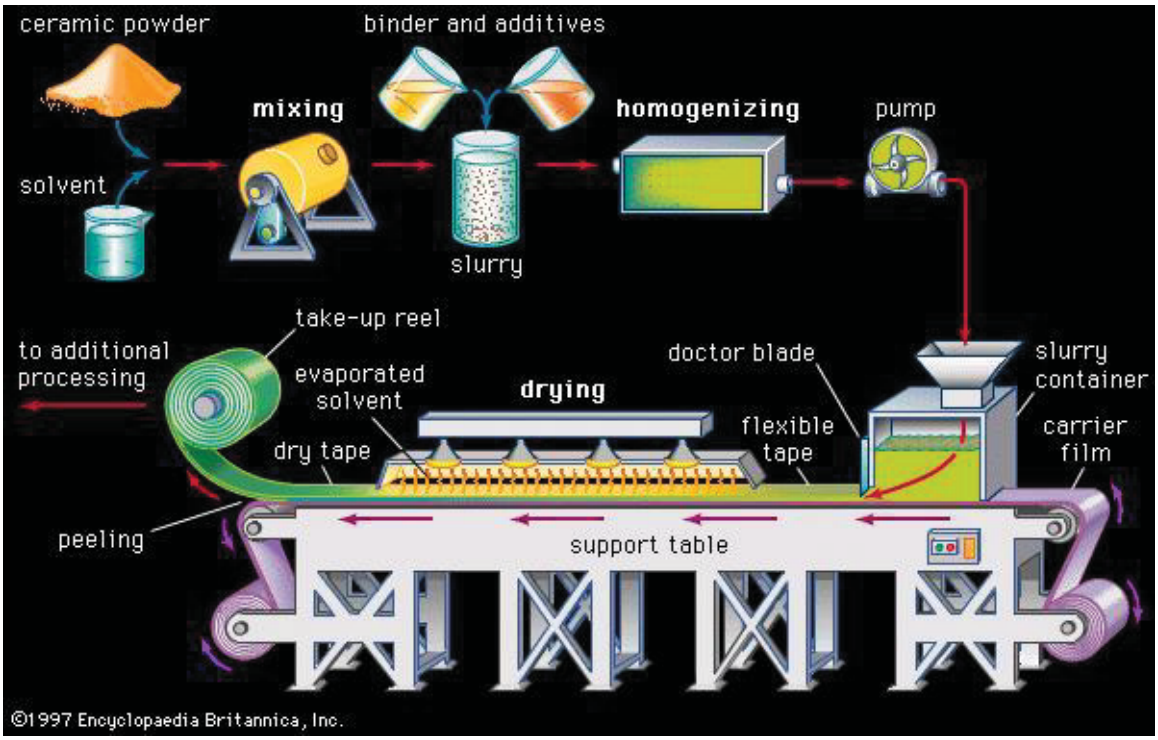

Figure 2.4: Tape casting process with mobile stage [41].

Once the tapes are produced, they will be machined into the desired shape and dried. Due to the high additive content, a separate debindering step must occur so as to prevent damage during the drying phase [40]. Even though the binder has been removed, the large moisture content still requires strict control of its removal. Often, this drying must be done at ~85℃, with high (50-70%) humidity [39]. Such careful control produces a green part that is sturdy enough for sintering and thermal degradation of any remaining additives [39]. This is the final step in tape casting, and—if all previous steps have been done correctly—a high strength ceramic shape has been produced.

2.6 Uniaxial Pressing

Of all the techniques discussed in this chapter, Uniaxial Pressing requires the least amount of additives. It has the advantage of being a "dry" process, meaning that no moisture is incorporated into the ceramic shape [31]. Powder, as depicted in Figure 2.5, enters the chamber and an external force compacts it into the desired shape. Unlike the methods above, there is no need for a drying or debindering step, and the part can be sintered immediately upon shaping [31]. This is due to the strength of the green parts, which have exceptionally high density [31]. Such strong green parts also allow for machining prior to sintering, and the lack of additives means there is no residual waste to be disposed of.

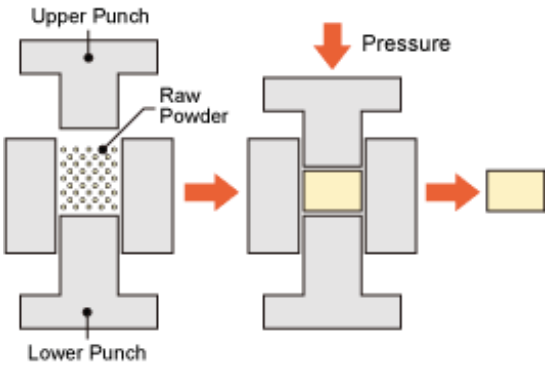

Figure 2.5: Uniaxial pressing of powder [42].

Although strong parts can be produced by uniaxial pressing, dimensions and geometries are quite limited. Large pressing area and limited height characterize this process [40]. For that reason, it is a method best suited to the production of tiles, slabs, or plates with smooth and uniform surfaces [31, 40]. Though a valuable method that produces high density parts, it also produces non-uniform density across the shape [31]. Furthermore, the dimensional accuracy is limited [31]. However, if additives must be avoided uniaxial pressing can be the method of choice.

2.7 3-D Printing

Additive manufacturing (AM) is a materials shaping method that has garnered much attention of late. The American Society for Testing and Materials (ASTM) defines this as “the process of joining materials from three dimensional (3-D) model data in a layer by layer fashion to form objects” [43]. This stands in stark contrast to traditional subtractive manufacturing, which involves the removal of material from a solid block to produce the desired part [44]. Even compared to the techniques presented above, it is truly unique in the way it produces ceramic shapes, not only because it may also process metals and plastics by the same method. Truly, additive manufacturing is a versatile and

useful technique for producing shapes of any material. The reasons for this—particularly as they pertain to ceramics—will be presented below.

Perhaps the greatest achievement of additive manufacturing is how it decreases the time between design and production. Standard manufacturing may produce a great many shapes, however specialized molds and machinery must be produced for each and every one of those shapes [43]. Furthermore, additional machining may still be required after shaping as the complexity of the part increases. Additive manufacturing, in contrast, can produce virtually any shape in a single step with no additional machining as soon as the 3-D model has been created. Such shapes have virtually limitless complexity and design without the need for specialized tools or post-processing [44]. This gives scientists "complexity for free," allowing ever changing demands to be quickly and effectively met [43, 45]. The only significant limit is in regards to the size of the part. Each additive manufacturing machine has a limit to size of the shape it can produce, while intricacy has virtually no limit.

Like other shaping methods, additive manufacturing may be broken up into separate and distinct branches. While these different branches have their own individual methods and benefits, they follow the same five steps [43]:

1. Creation of the design as a CAD (computer-aided design) model.
2. Conversion of the CAD file to an STL (standard triangulation language) file.
3. STL file is prepared for printing by configuring the model into 2-D slices which can be layered upon one another to produce the final shape.
4. Layer upon layer building of the 3-D shape.
5. Removal of the shape from the machine for final processing.

The primary way in which all additive manufacturing branches differ is during step 4. Though layer upon layer building occurs in all, it can be done in a number of ways.

All additive manufacturing techniques fall into two categories: laser based AM and non-laser based AM. Laser based methods utilize a laser that selectively melts powder into one cohesive shape that rapidly solidifies upon the laser's removal [43]. The laser fuses materials at specific heights and locations as designated by the CAD model while pistons move the sample stage [46]. This method, however, is typically for materials with low melting points. Ceramics have the highest melting points of nearly any class of material, and for that reason laser based methods are not popular in their shaping.

The second branch—non-laser based—binds the shape and particles together by methods other than the mere melting of material. As this pertains to ceramics, the 3-D printing (3DP) method of shaping is perhaps the most popular of the additive manufacturing techniques. Developed by the Massachusetts Institute of Technology in 1993, 3DP allows for the shaping of any material in powder form [44, 47]. What's more, it can produce ceramics with an unparalleled level of complexity [45]. Other shaping techniques simply cannot compete with 3-D printing in this regard, and that is particularly evident in Figure 2.6 below. There, one can see an open honeycomb structure in which the layers are staggered and distinct. No other shaping method is capable of producing such a part.

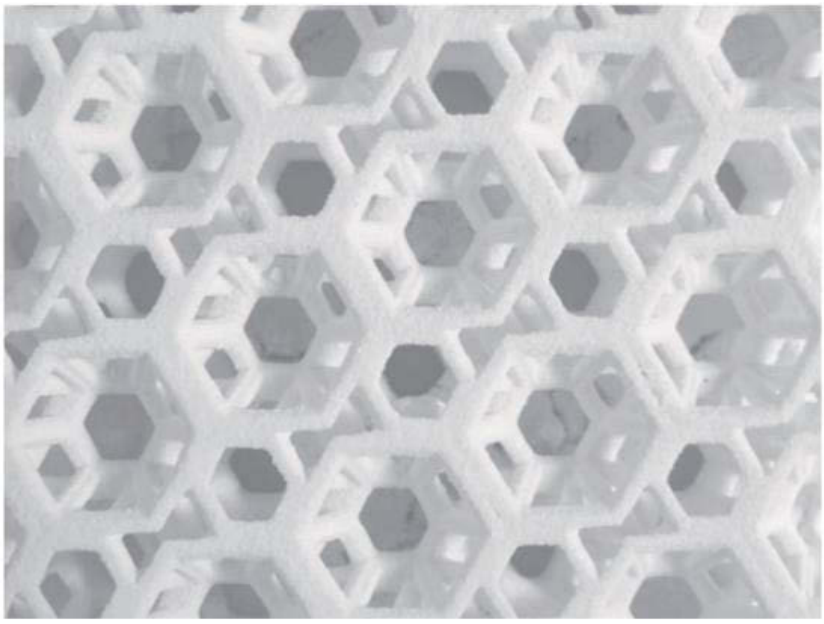

Figure 2.6: 3-D printed ceramic honeycomb [45].

The 3-D printing of ceramics is achieved using an ink-jet printing method. In this technique, liquid binder is sprayed onto a powder bed and rapidly cools to fuse particulates together [43]. It was mentioned above that an STL file cuts the final shape into 2-D slices, and now one must understand how these slices correspond to the ink-jet printing method. To put it simply, each 2-D slice represents an individual layer of binder. According to the STL, the first layer is sprayed into the ceramic build bed. The binder adheres to the powder below it, and powder from the feed supply is then rolled over it. Now, that layer of binder is adhering ceramic particles both above and below it in the shape of that 2-D layer. The second layer of binder is now dispersed directly over the last, and more powder is rolled. At this point, one has five alternating layers of ceramic and binder each adhering to one another. The process will then continue this alternating

dispersion of binder and rolling of powder until the entire part has been created. Upon completion of the green part, the powder bed is raised and loose powder is removed.

An image of the 3DP technique is presented in Figure 2.7. One will notice the pistons under both the feed supply and powder bed. As the shape begins to grow upward in the powder bed, the build area is lowered to maintain a constant distance between build surface and print head. Then, after each successive layer of powder is rolled, the feed supply will move upward, ensuring a constant supply of powder. The distance by which the build bed lowers with each jetting of binder determines the thickness of the ceramic layer rolled. When high layer thickness is used, fewer layers are needed to produce the corresponding part. Too thick layers, however, prevent proper lamination and the printing process will fail. Yet, the need for smaller layers often produces defects. Fine particle size is required to produce thin lamina, and the high surface area to volume ratio decreases flowability [47]. This, in turn, reduces the efficacy of the rolling motion and can produce gaps in the layers of ceramic.

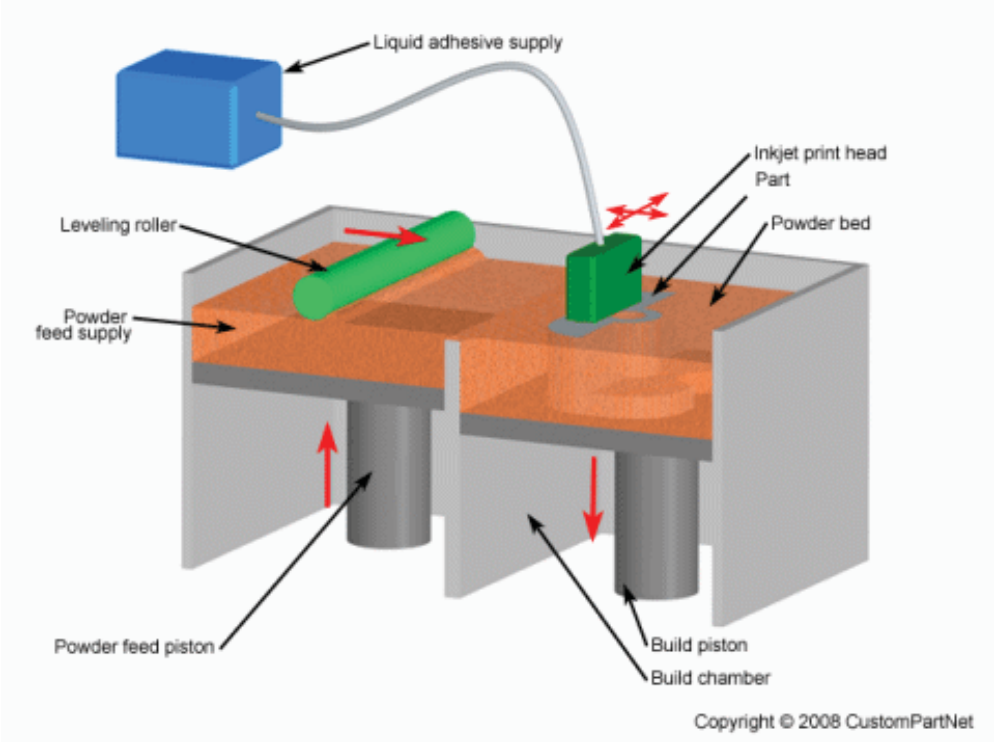

Figure 2.7: Depiction of the 3-D printing process [48].

Having completed the ink-jet printing process, the green part may be removed from the print bed for sintering. The powder rolling technique does not produce high densities, and these parts are typically very porous. Ideally, there must be less than 40% porosity for solid-state sintering to succeed [47]. The green part should also have uniform microstructure, so as to avoid defects in the final, sintered shape [47]. Sintering must occur at high temperatures to both burn out the binder and fuse the particles, however a large degree of shrinkage occurs [44]. The culprit behind this shrinkage is the significant porosity inherent to the 3DP process.

Binder saturation levels may also create defects in the printed shape. The amount of binder also determines the shape of the 3D printed part and affects the degree of shrinkage during sintering [44]. High binder concentrations make strong green parts, but

they tend to have non-homogeneous geometries and microstructures [44]. The geometric defects result from downward drift of excessive binder, resulting in unwanted expansion at the shape's base [44]. Excessive binder can also cause sintering issues, as it will act as a physical barrier to contact of ceramic particles [47]. In contrast, too little binder produces green parts that are weak and difficult to handle, despite having accurate geometries [44, 47]. The ideal binder concentration will produce strong shapes with good dimensional accuracy. While parameters such as this may be difficult to optimize, additive manufacturing continues to be a popular shaping method. The benefit of an unappalled level of geometric complexity often greatly exceeds the significance of the flaws inherent to this process.

2.8 Conclusion

A great many factors will affect one's choice of ceramic shaping method. While complexity and number of parts required are often the most important concerns, the defects inherent in each method must be taken into account.

Chapter 3
Mechanical Properties

3.1 Introduction to Mechanical Properties of Materials

If one is to better appreciate the advantageous mechanical properties of interpenetrating phase composites, one must have a basic understanding of the mechanical properties of materials. To this end, a brief overview of this vast and complex subject will be presented. This, of course, begins with stress and strain. Perhaps the two most fundamental aspects of mechanics, their relationship to one another presents an effective way to measure and assess the strength of a material. Stress (Equation 3.1) is the ratio of an applied axial force to the sample material's cross sectional area [49]. This force results in a change in specimen length, and the ratio of this change in length to original sample length is the corresponding strain (Equation 3.2). Strain may present as either a positive or negative ratio, depending on whether the sample is under tension or compression. Though these two terms may seem instinctual, one should think of tension and compression here in terms of interatomic spacing [50]. Under the former, force is applied in a pulling method, increasing interatomic spacing. Compression, meanwhile, is applied to a sample's surface and decreases interatomic distances. As interatomic distances decrease, the overall sample length decreases. This results in the negative strain associated with compression, and the positive strain for tension.

Equation 3.1: $$Stress = \sigma = \frac{F}{A} = \frac{Axial\ Force}{Cross\text{-}Sectional\ Area}$$

Equation 3.2: $$Strain = \varepsilon = \frac{\Delta l}{l} = \frac{Change\ in\ Length}{Original\ Length}$$

In gauging a material's mechanical properties, a stress-strain curve is produced. The most popular way of creating one is to pull a sample under tension to failure at a

constant rate [36]. This relates applied axial force (N) to sample elongation, and stress is plotted as a function of the strain [49, 51]. A sample stress-strain curve of a ductile material under tension is presented in Figure 3.1. Here, the shape is pulled downward at a constant rate with the top anchored (Fig. 3.1a). The first thing one will notice is the significant variation in the shape and slope of the graph. Initially, however, this curve begins with a linear elastic portion.

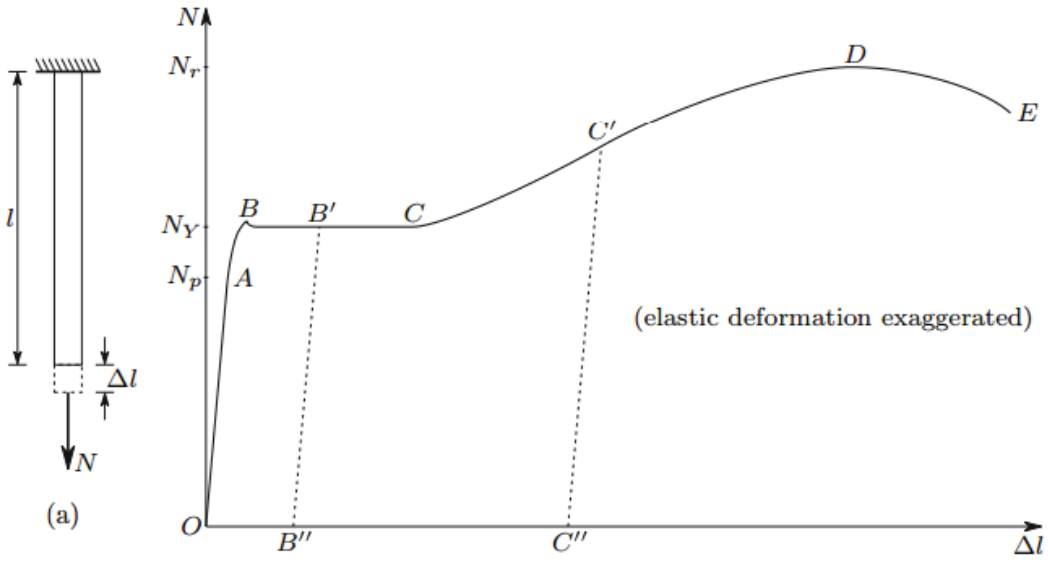

Figure 3.1: Tensile Stress-Strain Curve of a Ductile Material [49].

Ductile materials as a class exhibit elastic behavior, a trait that is not significant with brittle materials. This behavior refers to the ability to deform elastically, which results in atoms being temporarily displaced from their original positions. Such deformation is accompanied by a reduction in cross section. The relationship between these lateral and longitudinal strains is unique to each material and denoted as Poisson's Ratio (Equation 3.3) [8, 49]. Lateral strains occur perpendicular to extension, whereas longitudinal occur in the direction of extension.

Equation 3.3: $Poisson's\ Ratio = \nu = \frac{-\varepsilon(lateral)}{\varepsilon(longitudinal)}$

Once the load has been removed, the part will return to its original shape and dimensions [36]. In terms of the above curve, elastic deformation occurs from O→A. This linear, elastic portion has proportionality between load and extension, which allows one to calculate Young's Modulus [36, 51]. Also known as the Modulus of Elasticity (Equation 3.4), it is the slope of line OA and relates stress and strain to give a measure of material stiffness [36, 49].

Equation 3.4: $Young's\ Modulus = Modulus\ of\ Elasticity = \frac{\sigma}{\varepsilon}$

High modulus denotes significant stiffness in a material, as well as difficult extension under the given load [36]. In the context of line OA, steeper slope will accompany an increase in material stiffness. It is also important to note that while linearity ends at point A, the line from A→B still represents elastic deformation, with A being the Limit of Proportionality (N_p). At this point, there exists no proportionality between load and extension. So, elastic deformation here corresponds to the line from O→B, and the area under that region of the curve represents the elastic potential energy [49]. When unloading occurs, this energy is recovered as the shape returns to its original dimensions. Beyond the region from O→B, however, energy is lost as heat when the material is deformed [49]. This represents the transition from elastic to plastic deformation.

Unlike elastic deformation, plastic deformation is permanent. At Point B, the elastic limit, behavior becomes plastic and the strain is no longer reversible from that point onward [8]. When unloading does occur, the material will be deformed in the plastic region, while deformation that occurred in the elastic region will be reversed [8]. Overall, there will be a change in shape and dimensions as atoms are permanently

displaced from their original positions to occupy new ones [36]. The ability of a material to resist such plastic deformation—as well as penetration of its surface—is its hardness [8, 36]. What's more, for any plastic deformation to start, an amount of energy per unit volume specific to each material must be overcome [49]. This represents that material's resilience.

Beyond hardness, the plastic region also allows one to determine a material's yield strength. The yield point (N_y) represents the point at which significant plastic deformation has occurred [36]. To most effectively measure yield point, one will use the 0.2% offset yield strength as designated by the ASTM [36]. In this method, a line is drawn parallel to the linear portion of the curve with its origin at $\varepsilon = 0.002$ [36]. Where this line (B′′→B′) intersects the original curve is designated the yield point, and the corresponding stress is the yield strength.

A second useful property assessed by the stress-strain curve is ultimate tensile strength. This is the maximum stress achieved by the material, as seen in Point D above [36]. It is important to note that this property is determined by taking into account the original cross section. As elongation occurs, there is typically the start of necking after point D [36]. This necking represents a disproportionately large reduction of cross section at a specific point in the shape as visualized in Figure 3.2. This is also the cause of the downward shift in the curve after point D. Such a property is proportional to a material's ductility, with more ductile materials forming more substantial necks [36]. Ductility, in general, is a measure of a material's ability to deform when subjected to tensile stresses. Very ductile materials—such as metals—will undergo substantial deformation and necking before fracture occurs. At high temperatures, ductility will increase [49].

Conversely, brittle materials, which have low tolerance for tensile forces, will not form necks prior to fracture.

Figure 3.2: Formation of a neck in a tensile sample [52].

After much variation, the stress-strain curve terminates at Point E. This represents the separation of a single material into multiple parts, simply known as fracture [36]. Toughness denotes the amount of energy a material can withstand before fracture occurs and, once more, it is unique to each material [36]. Failure type is also unique to each material and can occur in one of two manners: ductile or brittle [36]. Having briefly touched upon ductility and brittleness above, they will be discussed in detail now.

As the curve above represents a ductile fracture, that will be presented first. As evident by Figure 1, such fracture occurs after a large degree of plastic deformation, and it is characterized by slow crack propagation [36]. In general, it also occurs in the following three steps:

1. A neck forms in the specimen, with cavities forming within that region.
2. Cavities begin to form a crack, which spreads outward perpendicular to the applied forces.
3. A “cup-and-cone” fracture occurs, the result of the crack changing direction near the surface to form a 45 angle to the tensile axis [36].

Such a “cup-and-cone” is presented in Figure 3.3. Note how the cross section above the fracture is larger, consistent with the fracture occurring in the neck where variations in cross section are expected.

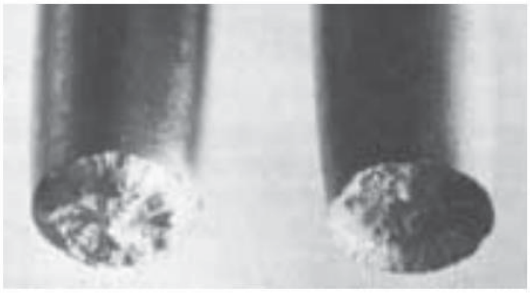

Figure 3.3: Cup-and-cone fracture in ductile sample [52].

In contrast to ductile materials, brittle fracture occurs with much less deformation. The linear elastic zone, for example, is much less defined [49]. The material will fracture abruptly after little plastic deformation [8, 53]. In viewing Figure 3.4, one will notice the stark differences between the stress-strain curve of a ductile (3.4a) and a brittle (3.4b) material. It is also important to note here that such a graph may have negative associated strains. This is the difference between tensile and compression testing. Compression testing, with its associated decrease in interatomic spacing, produces negative strain. One will also notice that the brittle material may undergo more substantial compressive stress than tensile.

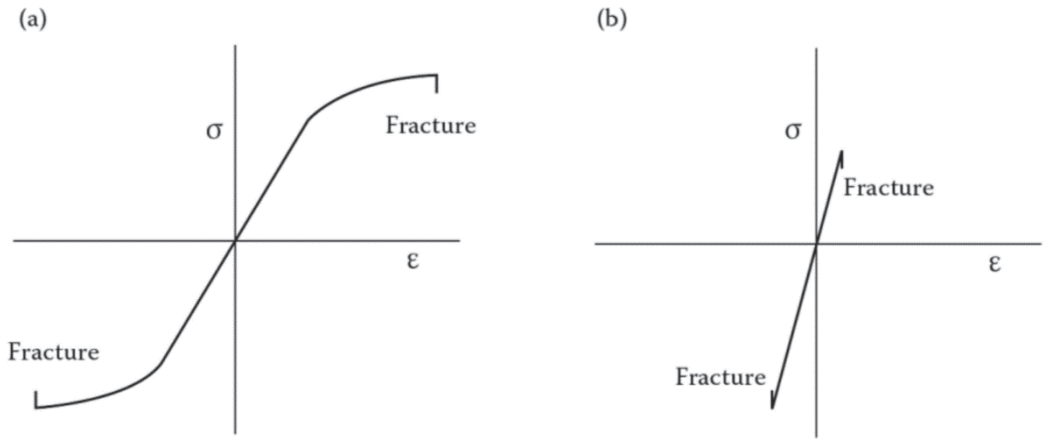

Figure 3.4: Stress-strain curves of a ductile (a) and brittle (b) material [8].

Ceramics, perhaps, represent the most expansive class of brittle materials. Whereas ductile materials fracture at the neck, ceramics will fracture at the largest effective flaw [54]. Essentially, the weakest link is where the chain breaks or, in this case, the ceramic. Such weakness arises as a result of surface cracks, porosity, inclusions, and large grains [36]. Pores, in particular, are also accompanied by a decrease in Young's Modulus [55]. Stress concentrates in these pores, and a crack can propagate outward once that stress reaches a sufficient value [36]. Ceramics cannot form necks to absorb the energy, and their brittle natures allows for easy crack nucleation and propagation [56, 36]. This crack will continue to move and grow until the ceramic eventually fractures.

While ductile and brittle are the two primary modes of failure, fatigue and creep can play important roles. When a material is subjected to repeated cyclic loading, it is worn down over time and the eventual failure is considered to be fatigue failure [36]. Once a crack has formed in a material, the repeated stresses from each cycle further propagate the crack [36]. This continues until the material fails, which occurs at lower stresses than for singular loading [36, 49]. Like brittle fracture, it occurs after minimal

plastic deformation [49]. Furthermore, it is similarly sensitive to surface imperfections. Rough surfaces—simply put—are flaws that create points of increased stress, which allows the crack to form and propagate inward more easily [36, 49]. The second failure, creep, also takes place over a significant period of time. Unlike fatigue, however, creep does not involve any cyclical loading. It is the slow plastic deformation that takes place when a material is under a continuous load for an extended period of time [36]. Here, one should think of a shelf, loaded with books. Over time, that shelf begins to sag. Eventually, it will fracture. This is creep and, like fatigue, it is an important consideration in the design and use of materials.

3.2 Grain Size & Strengthening

Having given a basic understanding of material properties and testing, methods of strengthening materials may be presented. Such methods involve the size and orientations of grains. Each individual crystallographic orientation inside a material represents a grain. The exterior of these grains, where they meet their neighbors, is known as a grain boundary. Materials comprised of multiple grains are referred to as polycrystalline, and they may be strengthened by minimizing the size of the individual grains [57, 58]. This will display a corresponding increase in both hardness and yield stress, and the Hall-Petch Relation (Equation 3.5) relates grain size to yield stress [57, 59]. The variables k and σ_o are constants dependent upon the material, and D is the diameter of the grains. Here, grain size is inversely proportional to yield stress.

Equation 3.5: $\sigma_y = \sigma_o + k_1 D_{GB}^{-1/2}$

In ductile metals and brittle ceramics, decreasing grain size produces effects beyond simply increasing yield stress. Metals, for example, can be made harder and more

brittle by greatly decreasing grain size [60]. Ductility and elasticity, therefore, is reduced. In ceramics, nanocrystalline grains can increase plasticity because of creep diffusion and grain boundary sliding [60]. To understand these effects better, one may look to the grain boundaries.

The shape of each grain is determined by its neighbors. When grains nucleate and grow outward, they bump up against other grains and boundaries from between them. Such boundaries involve the packing of irregular polyhedrons so as to minimize open space [61]. However, this may include a mismatch of atoms and crystallographic orientations, which produces holes [61]. Between the holes and the decreased density at the grain boundaries, diffusion occurs more easily there than in the grains [61]. However, dislocations, which are defects on the atomic scale, are blocked by grain boundaries and have their movement restricted [36, 51, 59]. As such, decreasing grain size increases the amount of grain boundaries while increasing material strength.

The strengthening effects of grain boundaries are hindered at high temperatures. In this case, the boundaries represent areas of weakness in a material, while the grains themselves are stronger [36, 61]. Often, intergranular failure tends to happen at high temperatures, as the failure will follow the grain boundaries [61]. For this reason, the temperature at which a material will be used needs to be taken into account before grain refinement.

3.3 Mechanics of Composite Materials

Compared to the tensile test presented above, composite materials are not so simply assessed. Metals, for example, are isotropic, having identical properties in all directions [1]. Composites lack this quality, resulting in difficult characterization of their

mechanical properties. However, there are two parameters specifically for measuring the mechanical advantages of composite materials: specific strength (Equation 3.6) and specific modulus (Equation 3.7) [1].

Equation 3.6: $Specific\ Strength = \frac{Ultimate\ Stress}{Density} = \frac{\sigma_{ULT}}{\rho}$

Equation 3.7: $Specific\ Modulus = \frac{Young's\ Modulus}{Density} = \frac{E}{\rho}$

The first parameter relates the ultimate strength of the material to its density, whereas the second relates Young's Modulus to density. In Figure 3.5, the specific strengths of various materials are presented. Composites, which achieve high strength with lower densities, tower above steel and other metals. Here, the advantages of composite materials are readily visualized.

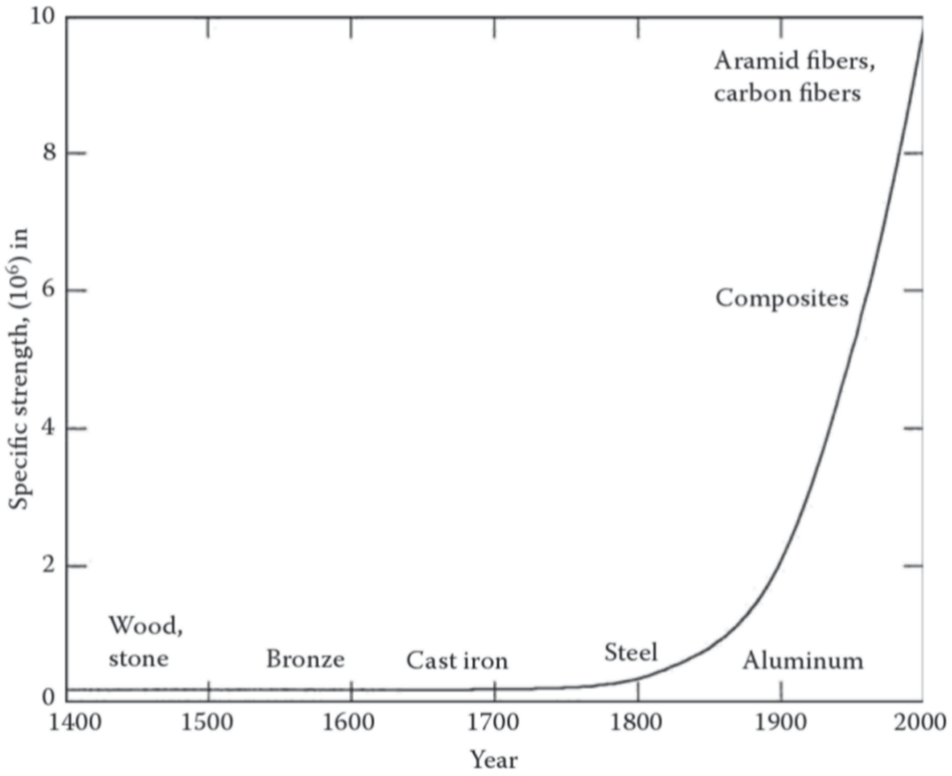

Figure 3.5: Specific strengths of various materials [1].

In the context of ceramic metal composites, their properties are highly dependent upon the relative concentrations and orientations of each constituent. Fracture toughness, in some CMCs, can possess proportionality to the diameter of the metal ligaments [14]. Maximum toughness is attained when those metal ligaments are also well bonded the ceramic matrix [16]. When these ligaments be unidirectional, however, advantageous properties are achieved only in that direction [10]. This is a weakness is remedied by the interpenetrating phase composite.

3.4 Mechanics of Interpenetrating Phase Composites

Compared to other variations of the ceramic matrix composite, IPCs have more impressive mechanical properties. C^4 materials have lower coefficients of thermal expansion (CTE), as well as higher stiffness, wear resistance, thermal conductivity, and fracture toughness [4]. Fatigue strength is also improved, with better resistance to damage from thermal cycling [10]. One may wonder how these effects come to be, and it is all the result of the interpenetrating nature. As contiguity of the phases increase, Young's Modulus increases and is further increased with composite density [12, 14, 21]. In Figure 3.6, the strength of an IPC is compared to the strength of a fiber-reinforced ceramic, both in the direction of the fibers and normal to them.

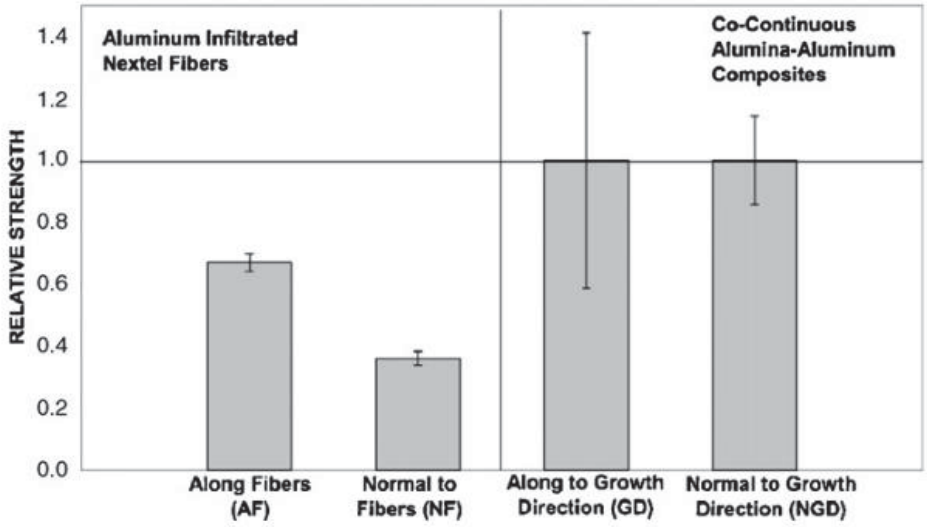

Figure 3.6: Comparison of the strength of an IPC and a fiber-reinforced CMC [10].

Compared to their fiber-reinforced counterparts, IPCs have significantly higher strengths than in either fiber direction. The direction of C^4 growth also shows no significant effect on strength.

It was said above that ceramic failure begins at a flaw site, and IPCs share this trait. Typically, failure begins at the ceramic's largest flaw, while metal determines overall fracture toughness [62]. Also, the metal has the most significant role in determining deformation behavior [16, 62]. Despite this, IPCs show no significant ductility even with the metal phase because the material is predominantly ceramic [12]. Furthermore, transfer of load from matrix to reinforcement is improved by increasing interface strength and surface area [62]. This is accompanied by an increase in material toughness, and is achieved by decreasing the diameter of both the ceramic and metal ligaments [1]. The more the matrix is in contact with reinforcement, the more substantial the increase in composite properties [21]. Strength of the interface depends on the matrix

and reinforcement's ability to bond to one another, necessitating few defects and sufficiently high wettability of one to the other.

A very interesting aspect of the IPC is its behavior at high temperatures. The compressive strength of an alumina-aluminum IPC produced from slip casted silica was assessed at temperatures up to 800℃ [9]. The results of this test are presented in Figure 3.7, and one will notice that at all temperatures compressive strength remains above 200 MPa. Even at 800℃, at which point aluminum—with a melting point of 660℃—is molten, such strength is retained. This is, of course, attributed to the ceramic matrix. It provides enough strength to maintain the structural integrity of the composite even when the metal has melted.

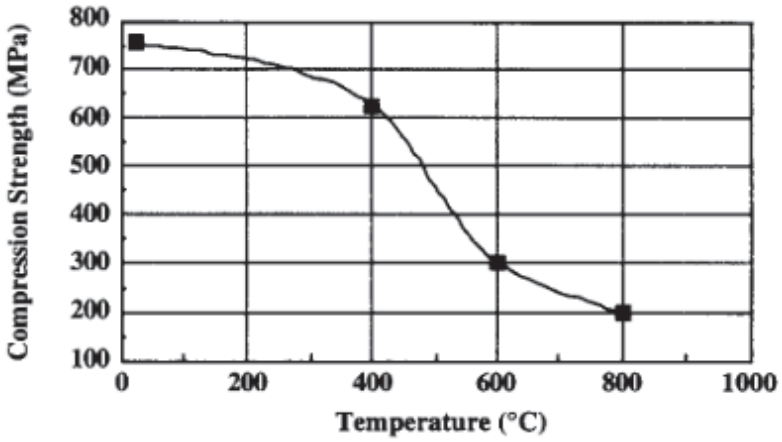

Figure 3.7: Compressive Strengths of a C^4 composite at varying temperatures [9].

This composite was further subjected to analysis, and a table of material properties is presented in Figure 3.8. One will pay special attention to the graph of specific stiffness for various materials. Having mentioned the importance of this property for analyzing composite advantages, one will see how significantly improved the C^4 is compared to other materials.

Property	Value
Density	3.5–3.7 g cm^{-3}
Thermal conductivity	80 W K^{-1} m^{-1}
Coefficient of thermal expansion	10×10^{-6} K^{-1}
Young's modulus	215 GPa
Average MOR[a] in three-point bend	470 MPa
Fracture toughness	10.5 MPa $m^{0.5}$
Scuff testing	No wear

[a]MOR, modulus of rupture.

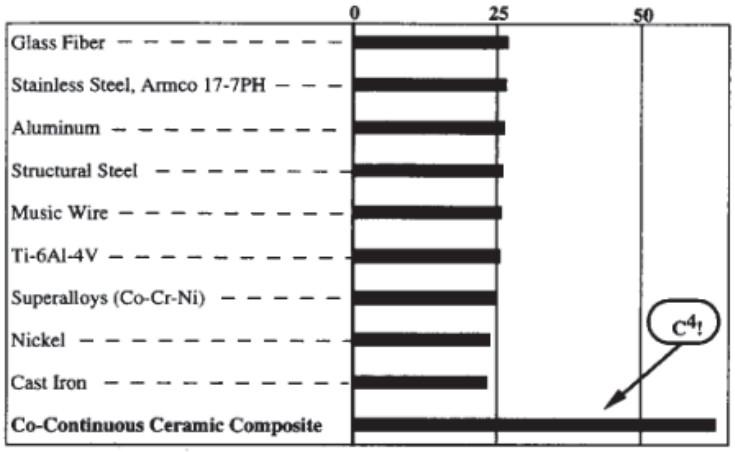

Figure 3.8: Comparison of specific stiffness for various materials [9].

A second property of note is the coefficient of thermal expansion. In Chapter 1, it was mentioned that the significant difference in thermal expansion for ceramics and metals can serve to weaken their composite. However, this is not the case in an interpenetrating phase composite. During reactive metal penetration, the differing coefficients of thermal expansion produce residual stresses [63]. The ceramic, with a lower CTE, enters a state of residual compression. The metal enters a state of tension. Then, before crack opening may occur, these residual forces must be overcome [63]. The end result is an increasing material toughness. Truly, interpenetrating phase composites have many significant advantages.

3.5 Crack Bridging

The metal constituent determines the fracture behavior of an IPC, and does this though crack bridging and crack blunting. As a crack moves through the ceramic matrix, it can move past an obstacle and leave that obstacle intact [50]. In an IPC, the obstacle is the ductile metal reinforcement. Bridging refers to the metal's ability to stretch across a crack and bridge the top and bottom, while blunting refers to the plastic deformation that takes places [9, 63]. These events will increase the material toughness and decrease the extent of the damage [50]. Such is the case in Figure 3.9, and one will clearly see the metal ligament that spans the crack. Notice the necking and deformation that occurs in these ligaments as they are stretched.

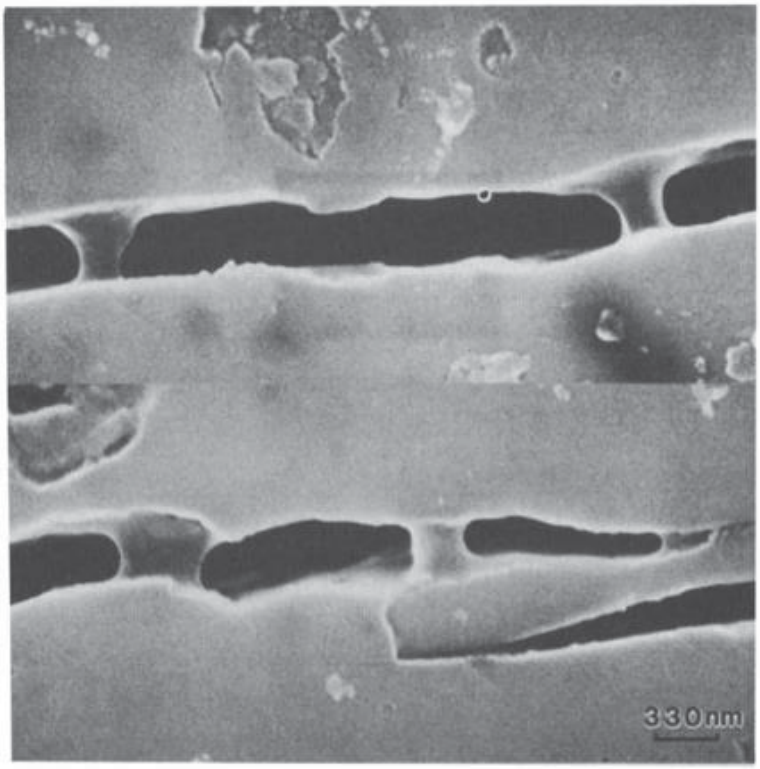

Figure 3.9: Crack bridging in a composite material [63].

With sufficient loading, the metal's bridging ability will be overcome. However, the continuous and microscopic nature of an IPC allows for a significant degree of crack bridging due to the high concentration of metal ligaments. Yet, with increasing load, more and more cracks will form, and the ligaments will be stretched until rupture. At this point, the material will fail.

3.6 Conclusion

The interpenetrating phase composite is a strong and versatile material with advantageous mechanical properties. Having lower coefficients of thermal expansion, crack bridging abilities, and exceptional specific stiffness they greatly eclipse other variations of the ceramic-metal composite.

Chapter 4
Statement of the Problem

This project, like many in the Wagner research group, was done in collaboration with the TCON division of Fireline, Inc. Based in Youngstown, Ohio, they supply silica and alumina parts for refractory applications. A major branch of their research and development, however, involves the production of interpenetrating phase composites. There, they utilize the reactive metal penetration of slip cast silica parts in aluminum to produce Al_2O_3/Al composites. Potentially, these IPCs may be used for a number of ballistic, automotive, and refractory applications. The desire to produce new and varied composites for such applications drives their collaboration with the Wagner lab.

Previously, it was discovered that magnesium aluminate spinel ($MgAl_2O_4$) may be incorporated into IPCs using a non-silica precursor. This work was done by Kyle Myers, and he reacted magnesium titanate ($MgTiO_3$) preforms with a melt of 95% aluminum and 5% silicon [64]. Spinel was produced alongside alumina, however, and the question then became whether a composite could be produced with only $MgAl_2O_4$ as the ceramic phase.

This interest in magnesium aluminate arose because of its chemical, and crystallographic properties. A second spinel, aluminum oxynitride, was also of interest for the same reasons. Having significant strength and chemical resistance, they are both cubic in structure. Alumina, in contrast, is hexagonal. In an interpenetrating phase composite containing cubic aluminum, it is expected that the boundary between a cubic metal and a cubic ceramic will be stronger. This, in turn, will increase the strength of the whole composite. Alumina and aluminum, in theory, will have a crystallographic

mismatch at their boundaries due to the differing crystal structures. A very simplistic depiction of these grain boundaries is presented in Figure 4.1. The goal, in this respect, is to produce an IPC containing either of the spinels as the sole ceramic phase. Then, scanning electron microscopy and mechanical properties testing may be used to analyze the composite's properties and determine whether a stronger and more cohesive interface was achieved relative to the Al_2O_3/Al composite.

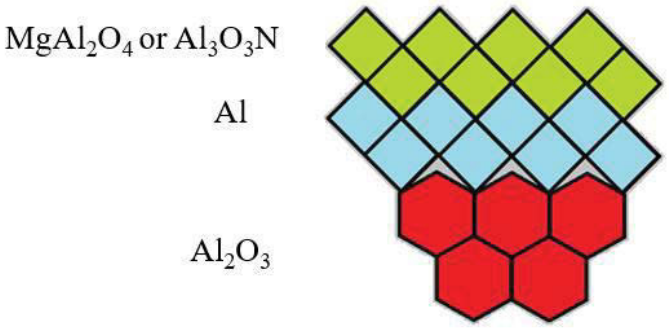

Figure 4.1: Simplistic diagram of cubic-on-cubic crystal packing and hexagonal-on-cubic crystal packing.

A second goal of this research involved the shaping of sacrificial precursors by 3-D printing. Slip casting is the primary method by which Fireline produces sacrificial ceramic shapes. The microstructure of IPCs formed using these parts is well known, and there exists great interest in seeing how the 3-D printing method affects final microstructure as well as composite strength. The methods by which ceramic precursors were printed will be presented in the ensuing chapter. Then, the impact of 3-D printing on the transformed composites will be discussed in depth.

Chapter 5
Experimental

5.1 Introduction

The production and shaping methods of sacrificial preforms are discussed in this chapter. All preforms were produced in an attempt to synthesize magnesium aluminate or aluminum oxynitride via reactive metal penetration and the TCON process. The specifics of these transformation methods will be presented in depth. Finally, techniques for analysis and characterization of the final composites will be discussed.

5.2 Precursor Shaping Methods

The target preform shape, regardless of the ceramic used, was a pellet with a one-half inch diameter and one-quarter inch height. Such parts were shaped either by uniaxial pressing (Fig. 5.1A) or 3-D printing (Fig. 5.1B). The former utilized a steel die held to a pressure of ~2000 psi for one minute.

Figure 5.1: Methods for shaping ceramic preforms consisted of the (A) uniaxial hydraulic pellet press or (B) the ExOne X1-Lab 3-D printer.

All 3-D printing was done on an ExOne X1-Lab printer. It works in the same alternating jetting of binder and rolling of powder method that was described in Section 2.7. The specific parameters used for the 3-D printing of sacrificial preforms are presented in Table 5.1.

Spread Speed	0.5 mm/second
Layer Height	100 µm
Binder Saturation	70%
Curing Temperature	190℃
Curing Time	4 hours

Table 5.1: Parameters for 3-D printing on the X1-Lab printer.

Following initial printing of the pellets, the entire build bed is removed from the machine. It is then inserted into the curing oven and heated. This allows the binder to set and harden, producing a solid shape. Upon cooling of the cured pellets, the excess powder may be brushed away. This exposes the final printed shapes that are strong enough for handling and sintering. Figure 5.2 shows the build bed and the printed pellets within immediately prior to the curing step.

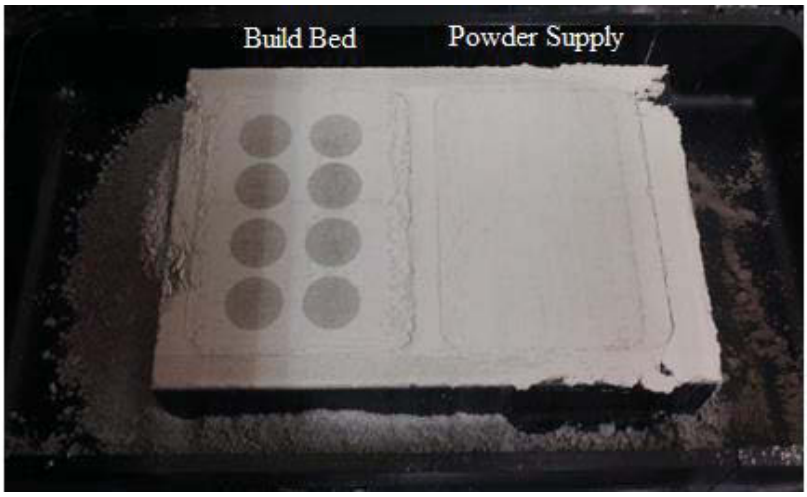

Figure 5.2: Build and feed beds of X1-Lab printer containing printed pellets prior to curing.

5.3 Precursor Materials

5.3.1 AlON Precursors

Here, the target preform was a silicon aluminum oxynitride. They are often referred to simply as SiAlONs, and many possible compositions are contained within this class of ceramics. The composition of interest in this thesis, however, is $SiAl_2O_2N_2$. Upon reaction with aluminum, this compoud would—in theory—react to give aluminum nitride and alumina in a 3:1 molar ratio (Reaction Scheme 5.1).

Reaction Scheme 5.1: $SiAl_2O_2N_2 + 4Al \rightarrow 2Al_2O_3 + 6AlN + 2Si$

While AlON is comprised of equal parts alumina and aluminum nitride (Reaction Scheme 5.2), the phase diagram (Fig. 5.3) explains the desire for the aforementioned 3:1 ratio.

Reaction Scheme 5.2: $Al_2O_3 + AlN \rightarrow Al_3O_3N$

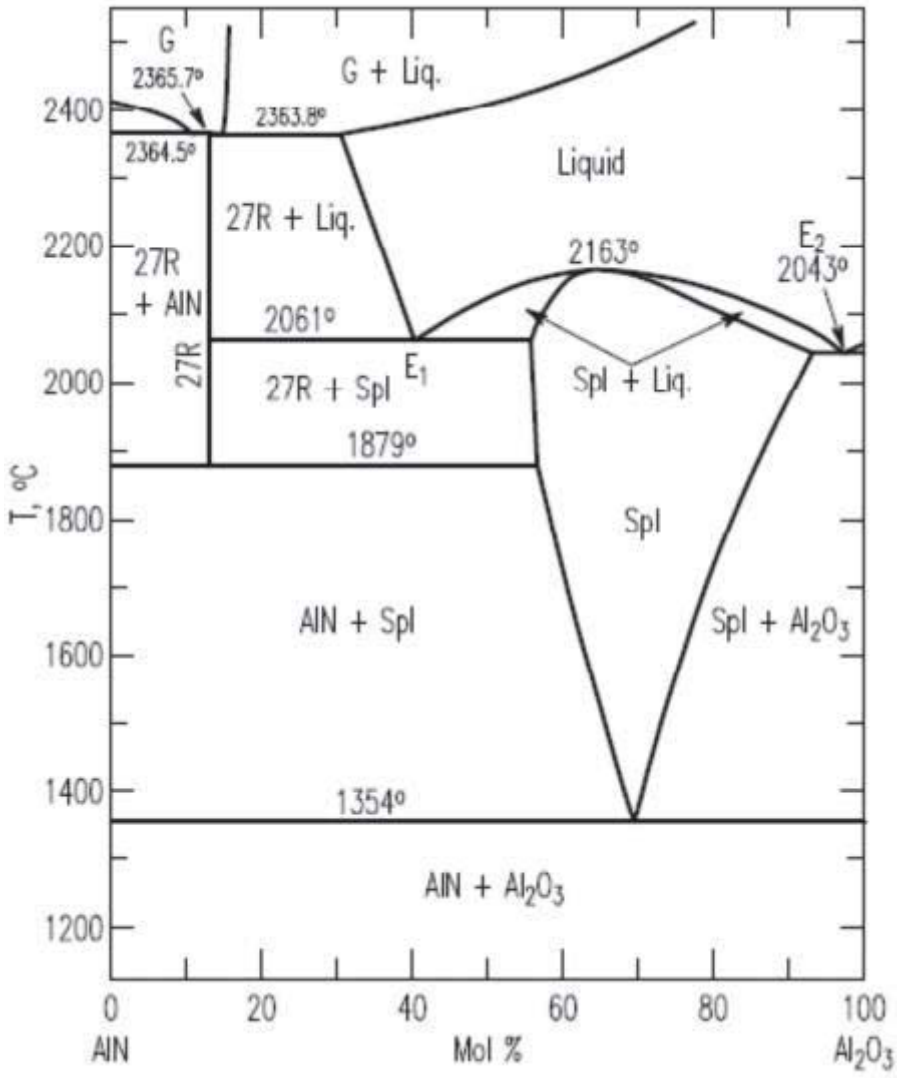

Figure 5.3: Phase diagram of the AlN/Al_2O_3 system [65].

An ideal synthesis will occur at the lowest possible temperature. The phase diagram of the aluminum nitride/alumina system posits that the lowest possible temperature at which AlON spinel may form is ~1350℃. The stiochiometry at this point corresponds to 70% AlN and 30% Al_2O_3. This can be approximated as a 3:1 ratio, hence $SiAl_2O_2N_2$ being the desired precursor phase. Production of this SiAlON occured by two

methods: a combination of high-energy ball milling and reactive sintering, or reactive sintering alone.

5.3.1.1 High-Energy Ball Milling & Reactive Sintering

The first method of SiAlON production utilized ball milling as a way to produce nano-particles of ceramic for greater reactivity during sintering. Tessier et al. outlined the specifics of this procedure and presented the general formula $Si_{3-x}Al_xO_xN_{4-x}$ for producing β-phase SiAlONs having a crystal structure correlating to that of the silicon nitride ceramic [66]. The preform of choice, $SiAl_2O_2N_2$, also possesses the β structure, and Tessier et al. similarly sought to produce this material. They desired to synthesize it using only two reagents: aluminum nitride and silica. This utilized a 2:1 molar ratio of AlN and SiO_2 with a value of X = 2 (Reaction Schemes 5.3 & 5.4 respectively).

Reaction Scheme 5.3: $SiO_2 + 2AlN \rightarrow SiAl_2O_2N_2$

Reaction Scheme 5.4: $Si_{3-x}Al_xO_xN_{4-x} \xrightarrow{x=2} SiAl_2O_2N_2$

Utilizing Tessier's procedure, 0.847 g SiO_2 and 1.155 g AlN were combined in a zirconia milling vial with two 0.5-inch zirconia mixing balls. The specific masses used play an important role on success of the reaction, and this will be described in detail during Chapter 6. The vial was then inserted into a SPEX 8000M Mixer/Mill for 18 hours. This milling drastically decreased the particle size of each powder allowing for greater reactivity with one another. The actual phase change, however, occurs during sintering.

Upon completion of milling, the powder was uniaxially pressed into pellets. The pellets were then placed into an alumina combustion boat and sintered under a nitrogen atmosphere. This begins with heating to 1300℃ at 600℃/h. There is no dwell time at this

temperature, and rate then changes to 90℃/h until 1450℃ is reached. At this point, the reaction is allowed to cool and the pellets were crushed for powder X-ray diffraction (Fig. 5.4). Despite rigid control of composition and sintering, the $SiAl_2O_2N_2$ phase was not formed. Two other SiAlONs were, however, as well as some alumina. As a result, this preform was not chosen for transformation.

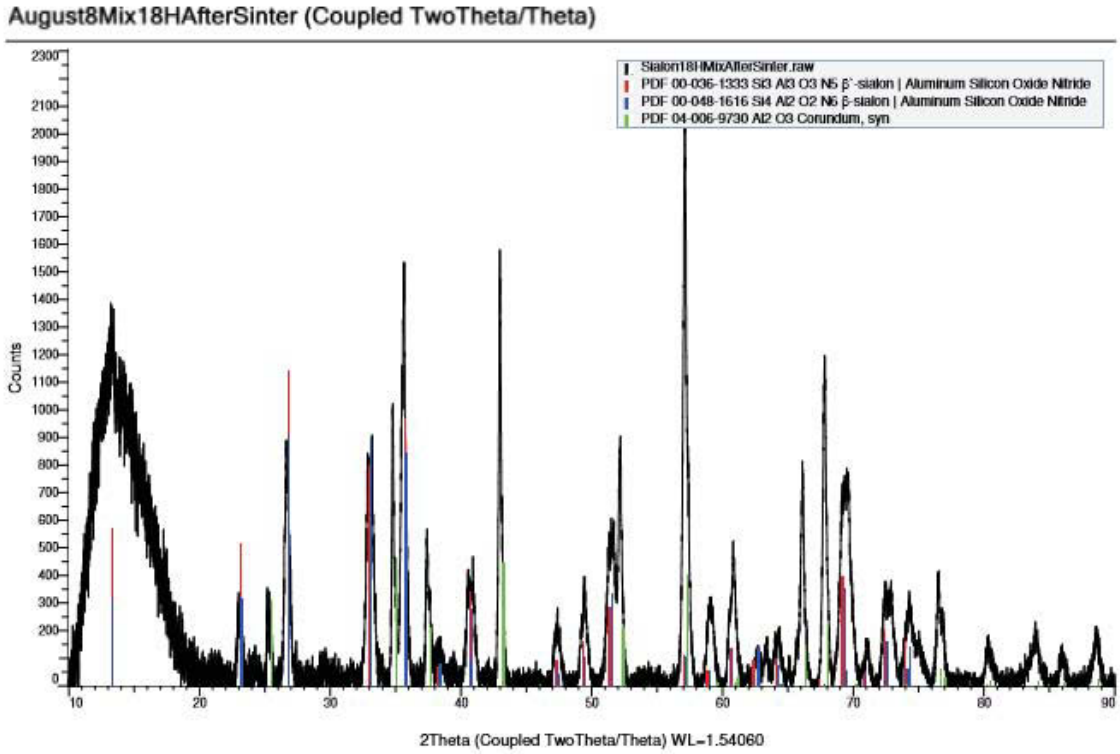

Figure 5.4: XRD pattern of the SiAlONs produced by high-energy ball milling and reactive sintering.

- $Si_3Al_3O_3N_5$, 00-03-1333, Hexagonal, P63/m (176), a = 7.67810 Å, c = 2.97690 Å
- $Si_4Al_2O_2N_6$, 00-048-1616, Hexagonal, P63/m (176), a= 7.66640 Å, c = 2.95950 Å
- Al_2O_3, 04-006-9730, Rhombo.H.axes, R-3c (167), a = 4.7690 Å, c = 13.02090 Å

5.3.1.2 Reactive Sintering

The second attempt at $SiAl_2O_2N_2$ occurred via the reactive sintering of raw powders. Pichlbauer et al. proposed a general chemical formula for the production of all SiAlONs as $Si_{6-z}Al_zO_zN_{8-z}$ [67]. Their target phase, $Si_4Al_2O_2N_6$, utilized a value of z = 2 (Reaction Scheme 5.5).

Reaction Scheme 5.5: $Si_{6-z}Al_zO_zN_{8-z} \xrightarrow{z=2} Si_4Al_2O_2N_6$

Synthesis of this material utilized a mixture of alumina, aluminum nitride, silicon nitride, and elemental silicon. Sintering under a nitrogen atmosphere both nitrogenizes the silicon and minimizes the loss of nitrogen from the ceramics at high temperatures. This produces the target phase (Reaction Scheme 5.6)

Reaction Scheme 5.6: $2Al_2O_3 + 3Si_3N_4 + 2AlN + 3Si + 2N_2 \xrightarrow{z=2} 3Si_4Al_2O_2N_6$

Whereas the Pichlbauer synthesis used z = 2, production of $SiAl_2O_2N_2$ requires a value of z = 4 (Reaction Scheme 5.7). Though this technically produces the $Si_2Al_4O_4N_4$ material, it is still a valid precursor in terms of this thesis because it is merely a doubling of the desired phase.

Reaction Scheme 5.7: $Si_{6-z}Al_zO_zN_{8-z} \xrightarrow{z=4} Si_2Al_4O_4N_4 \rightarrow 2SiAl_2O_2N_2$

Furthermore, the silicon concentration was varied across three reactions in an attempt to optimize the synthesis. The first reaction (Scheme 5.8), removed the silicon entirely, using only raw ceramic materials (Precursor S1).

Reaction Scheme 5.8: $Si_3N_4 + 2AlN + 2Al_2O_3 \rightarrow 3SiAl_2O_2N_2$

The second used stoichiometric amounts of silicon (Precursor S2), and the third used a 50% excess (Precursor S3). These two reactions both followed Scheme 5.9, despite the differing amounts of silicon during synthesis.

Reaction Scheme 5.9: $Si_3N_4 + 4AlN + 4Al_2O_3 + 3Si + 2N_2 \rightarrow 3SiAl_2O_2N_2$

Following preparation of the powders, all three were uniaxially pressed into pellets of differing shades of gray. They were then placed into alumina crucibles for sintering (Fig. 5.5A). Under a nitrogen atmosphere, they were heated to 1400℃ and held there for 6 hours. Then, they were heated to 1650℃ and held for an additional 2 hours. Once cool, they were removed from the furnace and all three bore a similar whitish-blue color (Fig. 5.5B).

Figure 5.5: SiAlON ceramics (A) before and (B) after sintering.

XRD analysis showed that all methods of preparation produced the desired $Si_2Al_4O_4N_4$ phase. However, all contained impurities. For example, the synthesis done without any elemental silicon lead to residual Si_3N_4 and Al_2O_3 in the pellet (Figure 5.6).

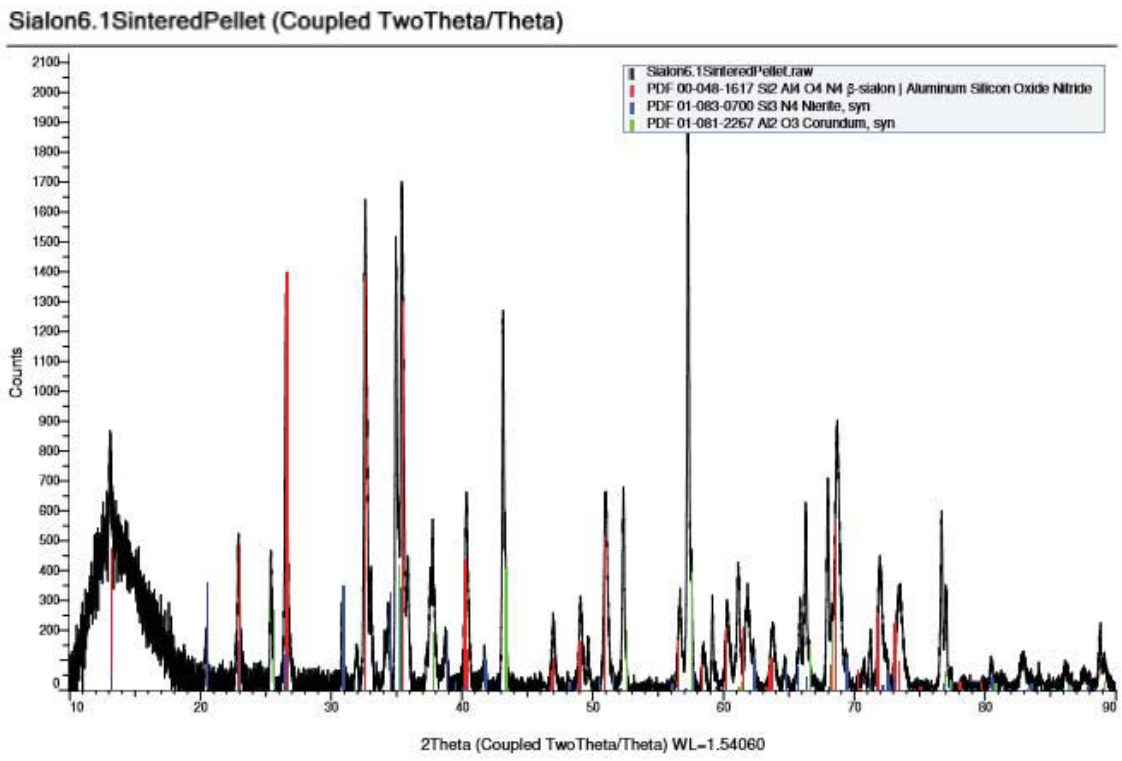

Figure 5.6: XRD pattern of SiAlON produced without elemental silicon (Precursor S1).

- $Si_2Al_4O_4N_4$, 00-048-1617, Hexagonal, P63/m (176), a = 7.72840 Å, c = 3.01150 Å
- Si_3N_4, 01-083-0700, Hexagonal, P31c (159), a = 7.76500 Å, c = 5.62750 Å
- Al_2O_3, 01-081-2267, Rhomo.H.axes, R-3c (167), a = 4.75400 Å, c = 12.98200 Å

Stoichiometric amounts of silicon, however, resulted in residual Al_2O_3 and AlN (Figure 5.7).

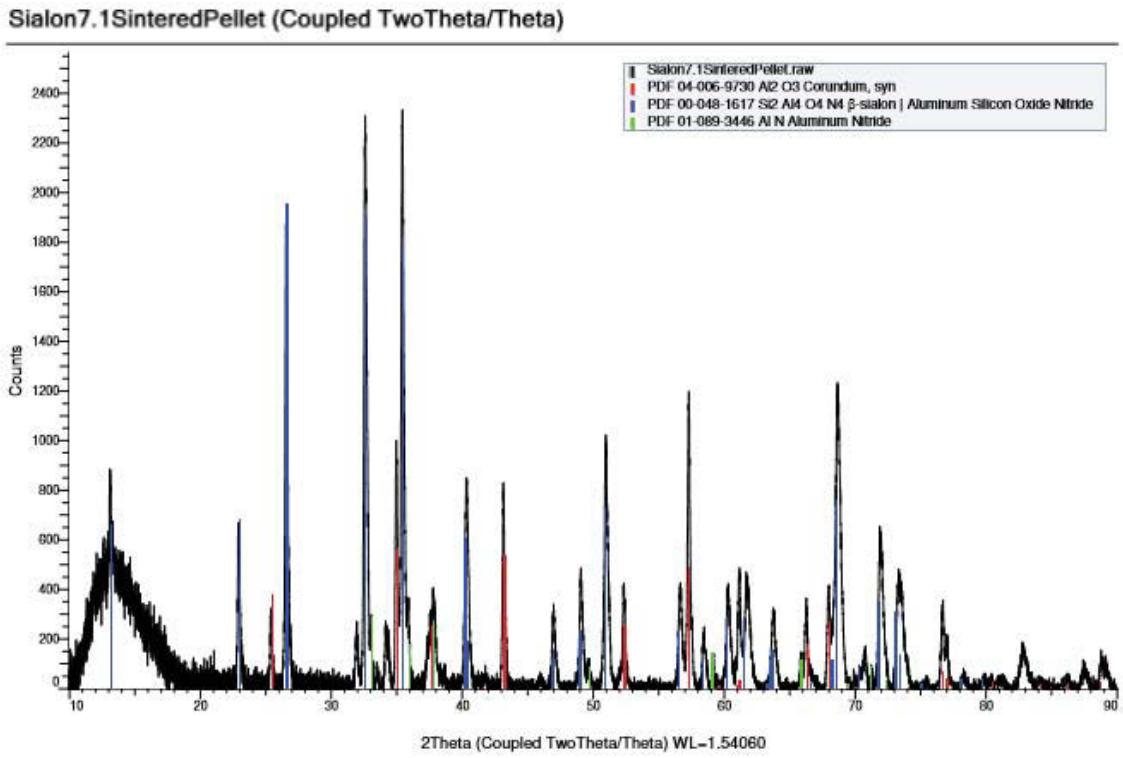

Figure 5.7: SiAlON produced with stoichiometric amounts of elemental silicon (Precursor S2).

- Al_2O_3, 04-006-9730, Rhombo.H.axes, R-3c (167), a = 4.76900 Å, c = 13.02090 Å
- $Si_2Al_4N_4O_4$, 00-048-1617, Hexagonal, P63/m (176), a = 7.72840 Å, c = 3.01150 Å
- AlN, 01-089-3446, Hexagonal, P63mc (186), a = 3.12300 Å, c = 4.98800 Å

The 50% excess of silicon yielded the best results. The only side product produced was alumina, and it was in smaller concentrations compared to the SiAlON (Figure 5.8).

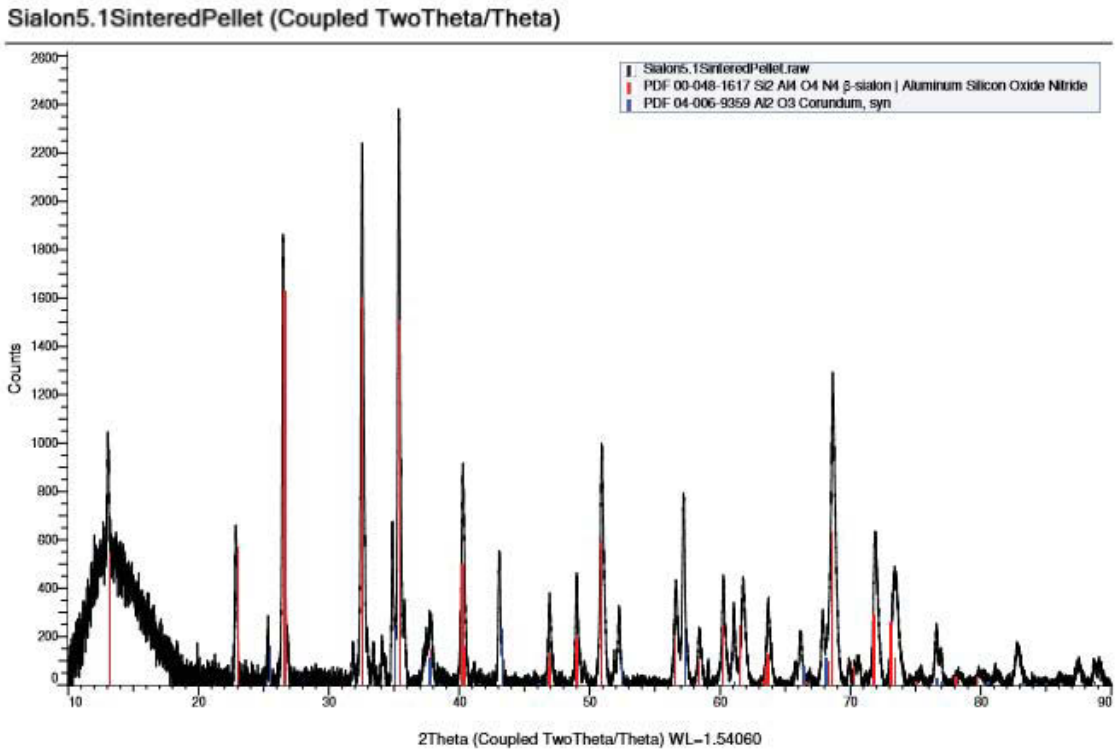

Figure 5.8: SiAlON produced with a 50% excess of elemental silicon (Precursor S3).

- $Si_2Al_4O_4N_4$, 00-048-1617, Hexagonal, P63/m (176), a = 7.72840 Å, c = 3.01150 Å
- Al_2O_3, 04-006-9359, Rhombo.H.axes, R-3c (167), a = 4.76500 Å, c = 13.03000 Å

Due to the success of all three methods, regardless of side products formed, all three were selected for transformation.

5.3.2 $MgAl_2O_4$ Precursors

All preforms covered in this section were created using magnesium titanate ($MgTiO_3$) as the base material. Synthesis of this ceramic followed the procedure outlined in Reaction Scheme 5.10 [64].

Reaction Scheme 5.10: $MgO + TiO_2 \rightarrow MgTiO_3$

Magnesium oxide (MgO) was combined and thoroughly mixed with anatase (TiO_2). To ensure complete sintering, the entire mixture was wet with acetone and compacted into pellets. Sintering then occurred in an alumina crucible under air. A temperature of 1500℃ held for 18 hours proved sufficient for complete reaction. Powder XRD analysis of a ground pellet showed large quantities of $MgTiO_3$ with $MgTi_2O_5$ as a very minor side product (Fig. 5.9).

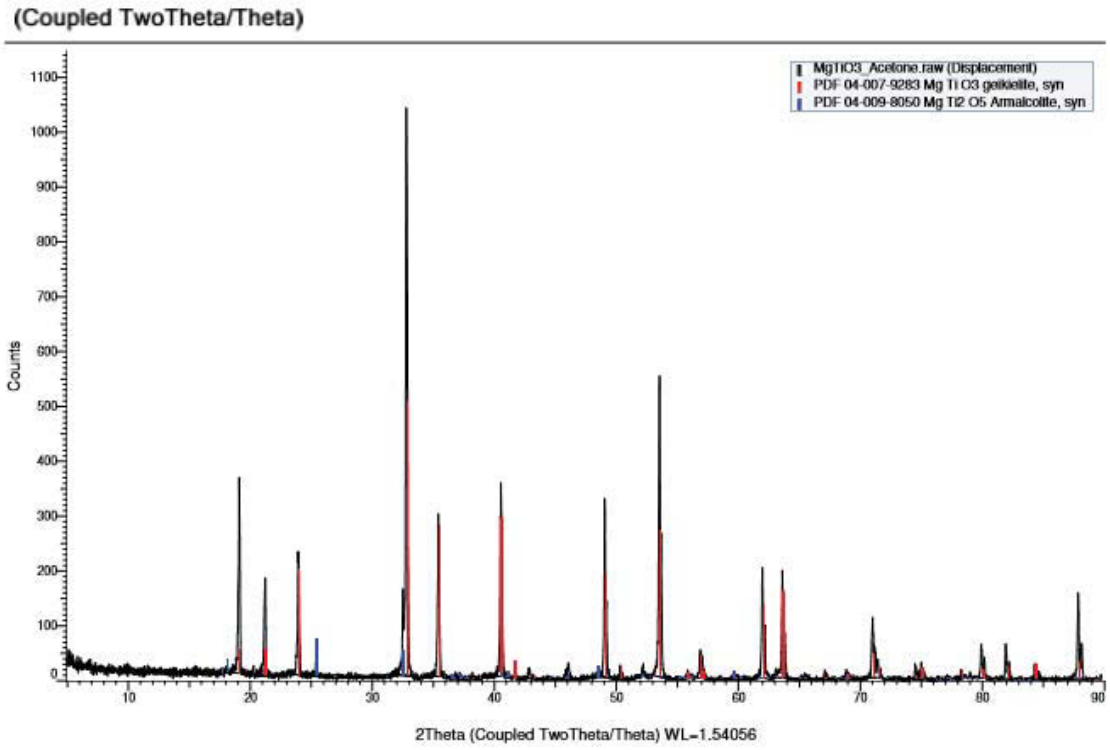

Figure 5.9: XRD pattern of $MgTiO_3$.

- $MgTiO_3$, 04-007-9283, Rhombo.H.axes, R-3 (148), a = 5.05600 Å, c = 13.89700 Å
- $MgTi_2O_5$, 04-009-8050, Orthorhombic, Bbmm (63), a = 9.75970 Å, b = 9.97890 Å, c = 3.74780 Å

The interest in $MgTiO_3$ results from its ability to form magnesium aluminate spinel during reactive metal penetration in 95% Al and 5% Si. However, spinel is produced alongside alumina and not as the sole ceramic phase. Now, the interest lies in whether a stoichiometric mixture of silica and $MgTiO_3$ can produce a precursor capable of yielding only the spinel. In theory, this precursor's reaction with aluminum will follow Reaction Scheme 5.11.

Reaction Scheme 5.11: $2MgTiO_3 + SiO_2 + 4Al \rightarrow 2MgAl_2O_4 + Si + 2Ti$

While the magnesium titanate was synthesized, the silica component of this precursor was bought from chemical suppliers. It was utilized both as amorphous silica gel and a crystalline silica powder.

5.3.2.1 Amorphous Silica Gel

5.3.2.1.1 Preforms for Furnace Transformation

Magnesium titanate and amorphous silica gel were combined in a 2:1 molar ratio and thoroughly mixed. They were then uniaxially pressed into pellets and allowed to remain unsintered.

5.3.2.1.2 Preforms for Kiln Transformation

A 2:1 molar mixture of $MgTiO_3$ and amorphous SiO_2 gel were combined to create a bulk powder for the 3-D printer. Following printing and curing, the pellets were sintered at 1300℃ for 6 hours under air. This preform will be henceforth referred to as the G-precursor.

5.3.2.2 Crystalline Silica

A 2:1 molar mixture of $MgTiO_3$ and crystalline SiO_2 were combined to create a bulk powder for the 3-D printer. Following printing and curing, the pellets were sintered at 1300℃ for 6 hours under air. This preform will be referred to as the C-precursor.

5.4 Transformation Processes

The methods for transformation of precursors involved either a tube furnace or a laboratory kiln. A Thermolyne 59300 High Temperature Tube Furnace with an alumina combustion tube served as the first method. The sacrificial pellets and the chosen metal(s) were placed in 10 mL alumina crucibles and inserted down the tube. Each side of the tube was then capped with aluminum end pieces. This prevented oxygen from reacting with the metal melt, and also provided a specially made argon inlet. The reactive metal penetration could then occur under inert atmosphere. The second method of transformation occurred at Fireline. There, pellets were transformed at 1200℃ in an industrial kiln for 24 hours.

5.4.1 Transformation of SiAlONs

All three SiAlONs produced in Section 5.3.1.2 were transformed in the tube furnace simultaneously. The crucibles were prepped first with the melting of aluminum blocks at 750℃ for 1 hour (Fig. 5.10A → 5.10B). This was done under an argon atmosphere to prevent oxidation of the metal. Having melted and cooled, the aluminum was solidified at the bottom of each crucible. This increases the open space in the crucible for each of the precursor pellets. Each pellet was then placed atop the solidified metal (Fig. 5.10C), and additional aluminum was added (Fig. 5.10D). All three vessels

were inserted into the tube furnace and reacted for 60 hours at 1500℃ under argon and in a pure aluminum melt. They were then cooled to room temperature.

Upon removal from the furnace, all three pellets appeared to have transformed (Fig. 5.10E). The crucibles were broken off with a hammer to expose the metal and pellet. Then, the metal was melted away from the IPC using an oxygen/natural gas torch (Fig. 5.10F).

Figure 5.10: Transformation of SiAlON precursors in the tube furnace.

5.4.2 Transformation of $2MgTiO_3 + SiO_2$

5.4.2.1 Transformation of Uniaxially Pressed Pellets

This was done in varying metal melts. Pure aluminum was used for one reaction, while 95% aluminum with 5% of either silicon, magnesium, or titanium were used for an

additional three. Each melt was pre-melted before transformation by holding at 900℃ for 2 hours under argon (Fig. 5.11A → B → C). A pellet was then placed atop the solidified metal (Fig. 5.11D). All four reaction vessels were then transformed under argon, and held at 1200℃ for 22 hours.

Upon removal from the furnace, they sat atop the solid metal (Fig. 5.11E). They had floated to the top of the bath during cooling, and very little was holding them to the metal. Rather than torch them out, the pellets and metal were simply pulled apart using vice grips (Fig. 5.11F).

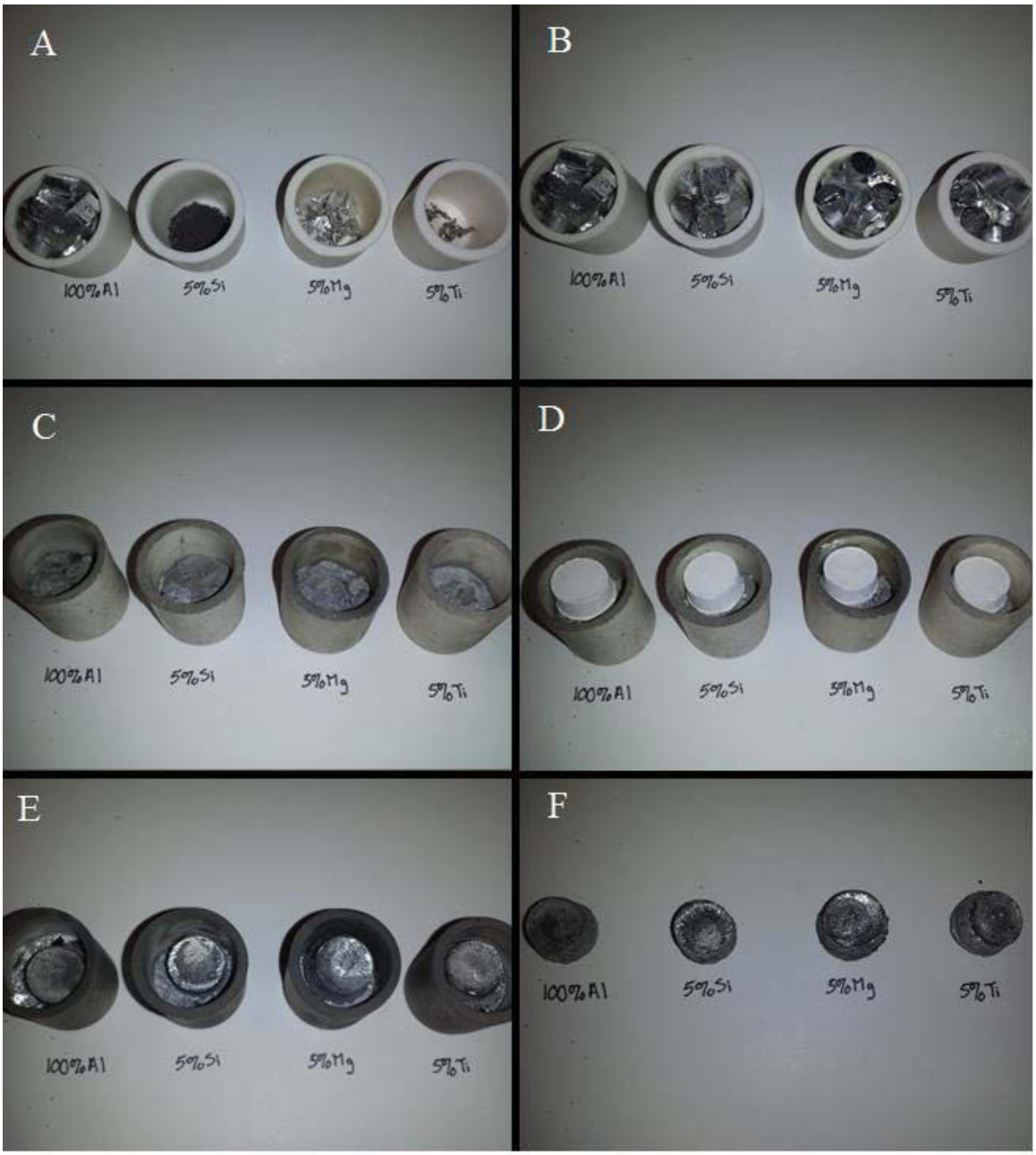

Figure 5.11: Transformation of unsintered and uniaxially pressed $MgTiO_3$ and SiO_2 gel preforms in the tube furnace.

5.4.2.2 3-D Printed 2MgTiO3 + SiO2

The preforms described by sections 5.3.2.1.2 and 5.3.2.2 were transformed in Fireline's kilns at 1200℃. A bath of 95% aluminum and 5% silicon was used, and the pellets were immersed for 24 hours.

5.5 Characterization of Transformed Materials

5.5.1 Cutting, Grinding, and Polishing

Characterization and analysis of transformed materials was preceded by cutting, grinding, and polishing. The first method produced a ~5 mm thick cross sectional slice of the composite. This was done on a Buehler Isomet 1000 Precision Cutter with an Isomet 15HC Wafering Blade. It is important to note that all composites were cut such that their geometric center is part of the cross sectional slice. This allows for better analysis of both the edges and center of the material.

Once cut, the composite was ground and polished. The high magnification of a scanning electron microscope requires that the sample be as smooth as possible. This is achieved first by grinding the sample flat, then polishing it to remove the smallest of surface defects. A Struers PlanoPol-3 was used for these purposes. It acts as a magnetic, rotating mount for the grinding and polishing disks described in Table 5.2. This table also presents the steps, lubricants, and suspensions used.

Step	Disk	Suspension	Lubricant
1	MD-Piano 120	-	Water
2	MD-Piano 600	-	Water
3	MD-Piano 1200	-	Water
4	MD-Plan	DP-Paste M 6 µm	DP-Lubricant Blue & Water
5	MD-Dac	DP-Paste M 3 µm	DP-Lubricant Blue & Water
6	MD-Nap	DP-Paste M 1 µm	DP-Lubricant Blue & Water
7	MD-Nap	DP-Paste M 0.25 µm	DP-Lubricant Blue & Water

Table 5.2: Steps for grinding and polishing of transformed samples.

After successful polishing, the samples are washed with water to remove any grime resulting from the polishing wheel. Then, they are sonicated in acetone for 5 minutes. This ensures complete removal of all residue on the composite. Finally, they are dried at 100℃ for 12 hours to completely remove any entrapped moisture.

5.5.2 X-Ray Diffraction (XRD)

X-ray diffraction is a valuable technique for identification of crystalline materials. This method works because all crystalline materials, regardless of their compositions, obey the same two rules. First, all crystals will present with one of the fourteen Bravais Lattices. Second, each compound will possess its own unique set of unit cell dimensions (a, b, and c) and interfacial angles (α, β, and γ). Figure 5.12 presents the fourteen crystal lattices, and one will notice that relationships between dimensions and angles are unique to each of the seven basic crystal structures: triclinic, monoclinic, orthorhombic, tetragonal, hexagonal, cubic, and rhombohedral (Trigonal R). Differing numbers of atoms in these seven, as well as the orientations of these atoms, give rise to the 14 Bravais Lattices. P, I, C, and F are used to denote the differences in each of the seven [68]. Primitive cells (P) have only one atom total, with an eighth of an atom at each of the vertices. Body-centered (I) and base-centered (C) both contain two atoms. Aside from having one split between each vertex, the former has a whole atom at its center while the latter has one-half an atom at its top and bottom. Face-centered (F) contains the most atoms with four. One-half atom sits at each of the six faces, and there is another one split between the eight vertices.

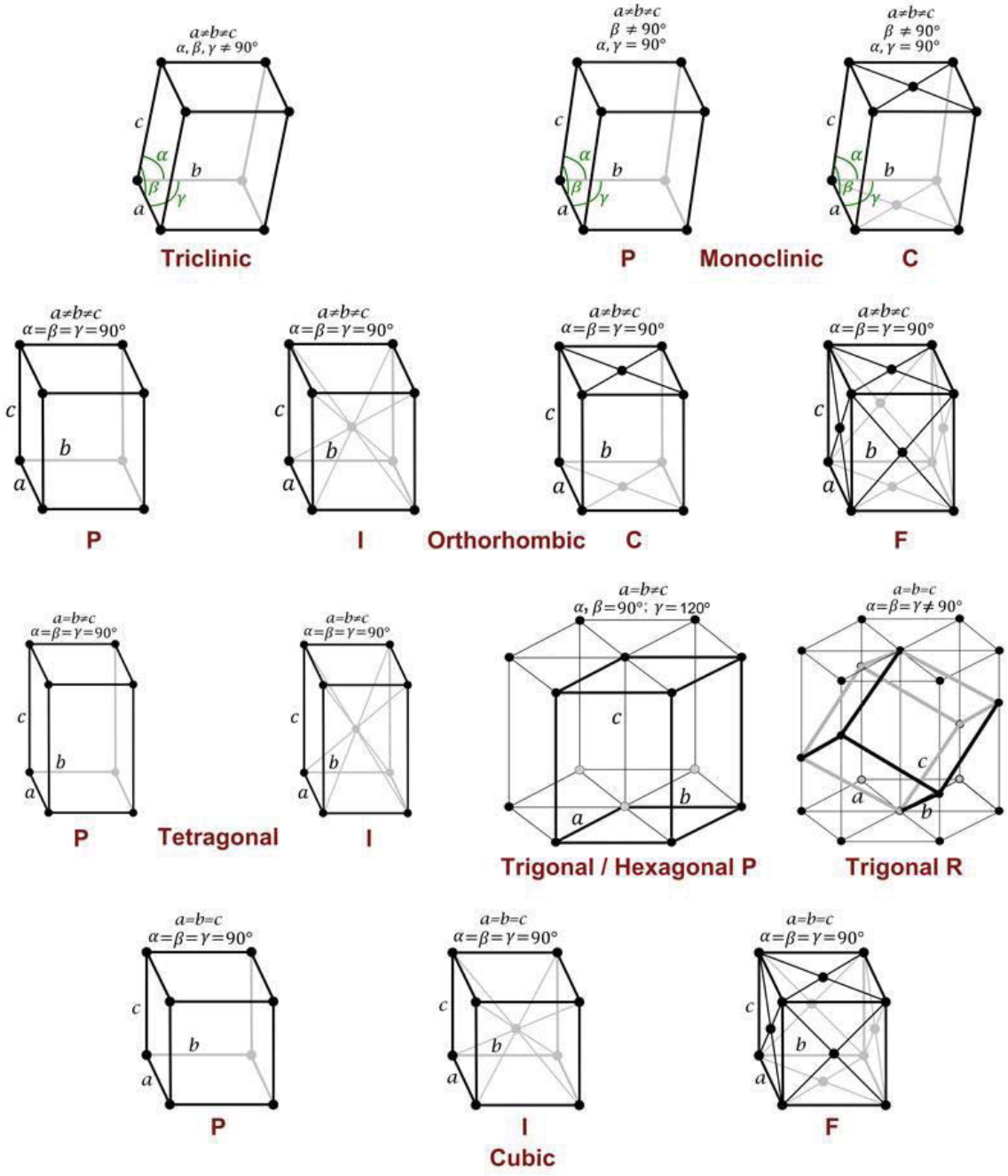

Figure 5.12: Fourteen Bravais lattices [68].

The unit cell dimensions, a, b, and c, correspond to the edge lengths for each lattice. The interfacial angles, α, β, and γ, are the angles between b and c, c and a, and a and b respectively. Each individual compound has its own select set of these six

variables, and that gives rise to unique X-ray diffraction patterns. A table (5.3) of unit cell dimensions and interfacial angles for each of the seven is presented below.

Crystal Lattice	Cell Dimensions	Interfacial Angles
Triclinic	$a \neq b \neq c$	$\alpha \neq \beta \neq \gamma \neq 90^{\circ}$
Monoclinic	$a \neq b \neq c$	$\alpha = \gamma = 90^{\circ}$ $\beta \neq 90^{\circ}$
Orthorhombic	$a \neq b \neq c$	$\alpha = \beta = \gamma = 90^{\circ}$
Tetragonal	$a = b \neq c$	$\alpha = \beta = \gamma = 90^{\circ}$
Hexagonal	$a = b \neq c$	$\alpha = \beta = 90^{\circ}$ $\gamma = 120^{\circ}$
Rhombohedral	$a = b = c$	$\alpha = \beta = \gamma \neq 90^{\circ}$
Cubic	$a = b = c$	$\alpha = \beta = \gamma = 90^{\circ}$

Table 5.3: Unit cell dimensions and interfacial angles for each of the seven basic crystal lattices [68].

There exist two branches of x-ray diffraction: single crystal and powder. The first involves a small crystal exhibiting a single crystallographic orientation. The second method works with the understanding that a powder is simply an accumulation of crystallites. Such crystallites display all possible orientations and this method is utilized for characteriztion of bulk materials. Though the TCON composites are neither single crystals or powder, the large number of grains at various orientations allows for characterization of the entire material by powder XRD.

In general, a powder x-ray diffractometer possesses three primary components: an X-ray source, the sample stage, and the X-ray detector (Fig. 5.13). The first contains a cathode ray tube, which produces the X-rays needed for diffraction. A monochromator then filters these X-rays to a specific wavelength, and a collimator focuses them into a beam [69]. As this beam moves toward a specimen, the sample stage and detector will rotate and move. This serves to vary the angles θ and 2θ. The first represents the angle

between incident beam and sample, while the second refers to the angle between the incident beam and detector. Figure 5.13 shows this relationship clearly.

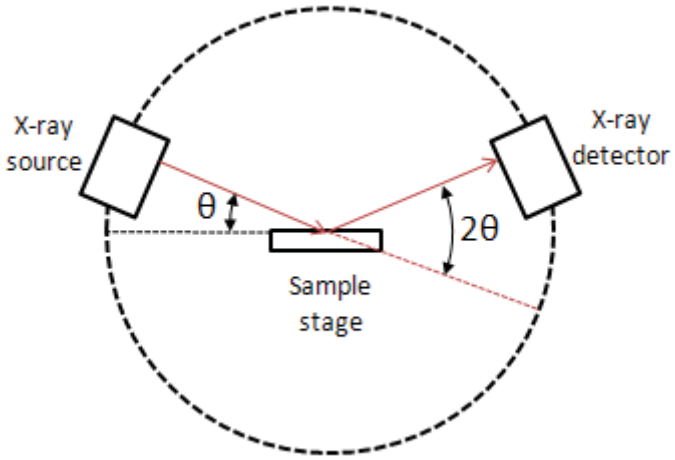

Figure 5.13: Three primary components of an X-ray diffractometer [70].

Typically, the X-ray beam will interact with the sample and scatter randomly. However, depending on the compound being analyzed, certain values of θ (and 2θ, by extension) will result in the original beam being diffracted. This is a result of constructive interference as the beam interacts with the sample's crystal planes. Figure 5.14 shows a single crystal sample with planes visualized as two sets of parallel lines. In the first image, the crystal is not oriented to produce constructive interference and the original beam is scattered in various directions. In the second and third images, the samples are rotated to specifics angles that allow for constructive interference of the diffracted beam.

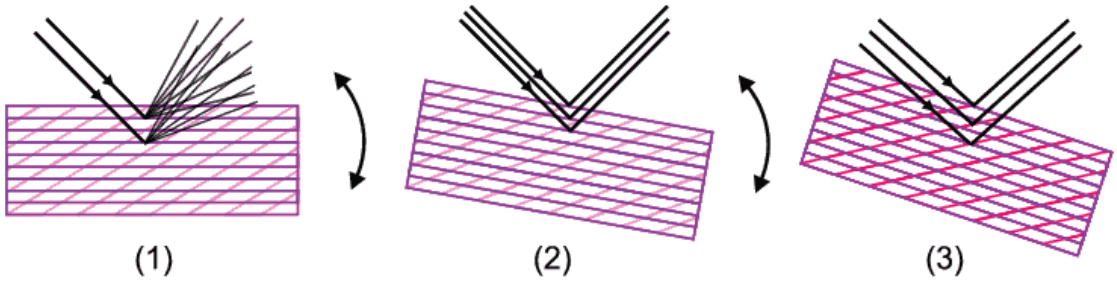

Figure 5.14: X-ray diffraction of planes in a single crystal [71].

In comparison to single crystals, powder samples are composed of many millions of individual crystallites. The large number of them means that every possible crystallographic orientation is present in the sample. While not every crystallite is positioned for diffraction, the sheer number of them means that—statistically—all appropriate values of 2-theta for the specific compound will produce an intense diffracted beam as the sample rotates. This is evident in Figure 5.15, where different crystallographic orientations are depicted in white, green, and pink. These d1 and d2 beams produce strong signals at the detector, and a peak is plotted on the diffraction pattern for each value of 2-theta at which this diffraction occurs.

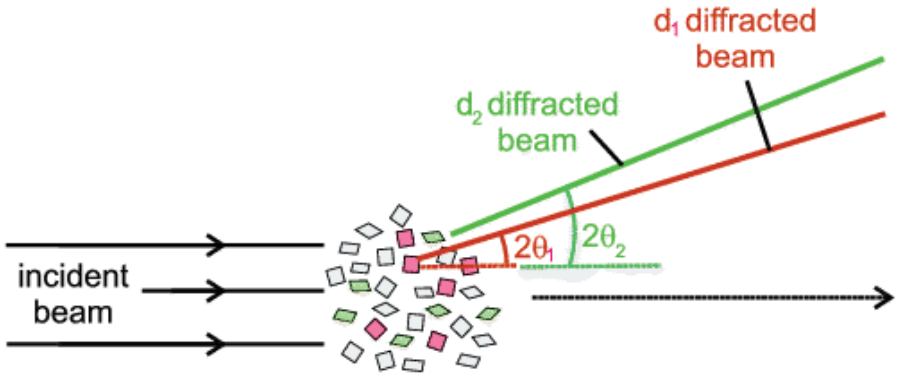

Figure 5.15: X-ray diffraction of different crystallites in a bulk powder [71].

To understand how diffraction allows for sample identification, one must understand crystal planes. Simply put, they are a series of geometric planes that link atoms throughout the crystal. Each crystal plane represents a set of parallel slices that are separated by the interplanar distance, d (Fig. 5.16). There exist infinite numbers and orientations of these crystal planes, and they are identified by Miller Indices.

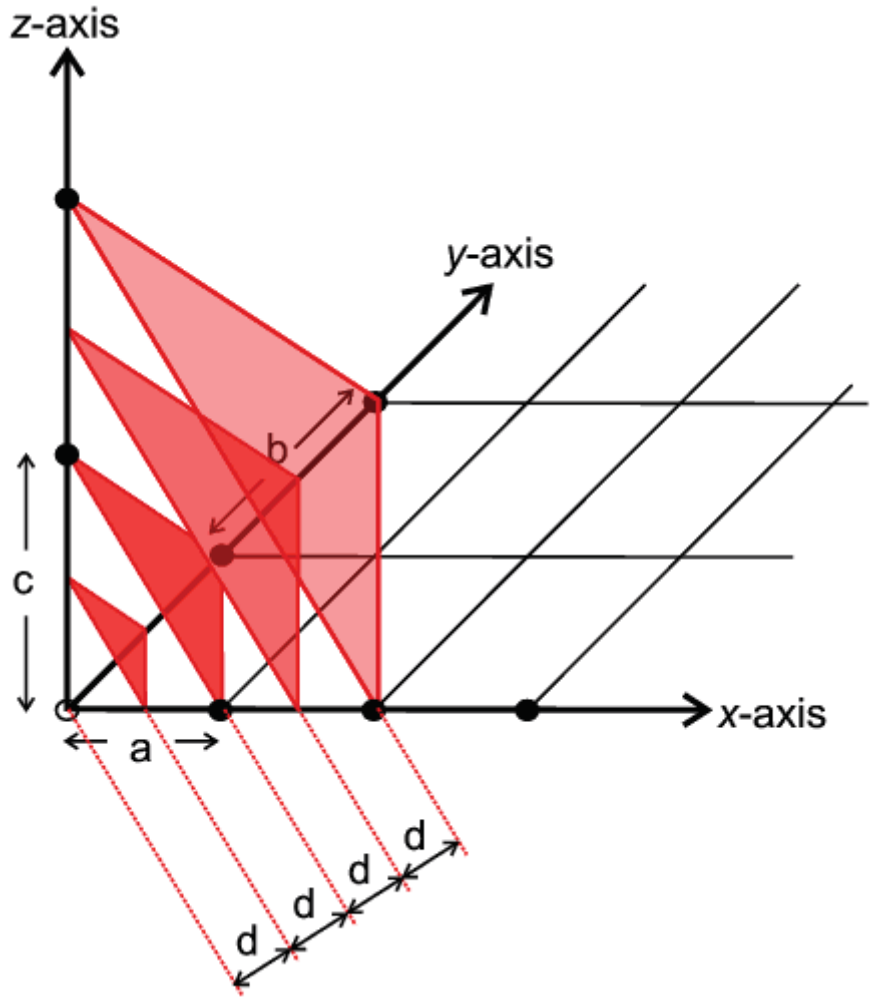

Figure 5.16: Crystal planes (red) and their accompanying interplanar spacings (d) [71].

Miller indices describe crystal planes in terms of h, k, and l. Identification of these values takes place in three steps:

1. In terms dimensions a, b, and c, determine where the crystal plane intersects the unit cell.
2. Take the reciprocal of the intercepts then reduce to the smallest possible integer.
3. Enclose in parentheses as (hkl) [72].

In a crystal, every plane must satisfy Equation 5.1, where $\frac{h}{a}, \frac{k}{b}, \text{and} \frac{l}{c}$ are the intercepts of the plane on the x, y, and z axes respectively [72].

Equation 5.1: $\frac{h}{a}x + \frac{k}{b}y + \frac{l}{c}z = 1$

It is important to note that when the intercept occurs on a negative axis, the resulting h, k, and/or l value will be capped with a bar (i.e. $\bar{h}$). Furthermore, families of planes related by symmetry are written as {hkl}. Families may be thought of as having the same three integers (regardless of whether they are negative or positive) comprising h, k, and l in any combination. For example, the family {321} is comprised of planes [132], [213], $[\bar{3}\bar{2}\bar{1}]$, $[1\bar{3}2]$, etc.

From the Miller Indices, one may determine interplanar spacings for a family of planes. It is important to note that every material will have its own specific set of these crystal planes. Furthermore, each of the seven basic crystal lattices has a unique equation for determining d-values, and they are presented in Table 5.4.

Crystal Lattice	D-Spacing
Cubic	$\frac{1}{d^2} = \frac{h^2 + k^2 + l^2}{a^2}$
Tetragonal	$\frac{1}{d^2} = \frac{h^2 + k^2}{a^2} + \frac{l^2}{c^2}$
Hexagonal	$\frac{1}{d^2} = \frac{4}{3}\left(\frac{h^2 + hk + k^2}{a^2}\right) + \frac{l^2}{c^2}$
Rhombohedral	$\frac{1}{d^2} = \frac{(h^2 + k^2 + l^2)\sin^2\alpha + 2(hk + kl + hl)(\cos^2\alpha - \cos\alpha)}{a^2(1 - 3\cos^2\alpha + 2\cos^3\alpha)}$
Orthorhombic	$\frac{1}{d^2} = \frac{h^2}{a^2} + \frac{k^2}{b^2} + \frac{l^2}{c^2}$
Monoclinic	$\frac{1}{d^2} = \frac{1}{\sin^2\beta}\left(\frac{h^2}{a^2} + \frac{k^2\sin^2\beta}{b^2} + \frac{l^2}{c^2} - \frac{2hl\cos\beta}{ac}\right)$
Triclinic	$\frac{1}{d^2} = \frac{1}{V^2}(S_{11}h^2 + S_{22}k^2 + S_{33}l^2 + 2S_{12}hk + 2S_{23}kl + 2S_{13}hl)$ $S_{11} = b^2c^2\sin^2\alpha$ $S_{22} = a^2c^2\sin^2\beta$ $S_{33} = a^2b^2\sin^2\gamma$ $S_{12} = abc^2(\cos\alpha\cos\beta - \cos\gamma)$ $S_{23} = a^2bc(\cos\beta\cos\gamma - \cos\alpha)$ $S_{13} = ab^2c(\cos\gamma\cos\alpha - \cos\beta)$ $V = abc\sqrt{1 - \cos^2\alpha - \cos^2\beta - \cos^2\gamma + 2\cos\alpha\cos\beta\cos\gamma}$

Table 5.4: Interplanar spacing equations for the seven basic crystal lattices [73].

As the unit cell dimensions and interfacial angles are unique to each compound, the equations above will yield characteristic values of d for all materials. This allows for characterization of virtually any crystalline phase.

To determine the identity of a material by X-ray diffraction, one must be able to relate interplanar spacing to the angle of diffraction. This is done by Bragg's Law (Equation 5.2) [71].

Equation 5.2: $n\lambda = 2d \sin\theta$

n = unity

λ = wavelength of X-rays used

d = interplanar spacing

θ = angle

As only monochromatic radiation is used, the wavelength is held constant while the angle is varied by rotating the sample and detector. When the X-ray beam is diffracted (i.e. when constructive interference occurs) and a peak forms on the diffraction pattern, Bragg's Law is said to be satisfied and one may calculate interplanar spacing for this angle. These d-values, in turn, are compared to known values and the sample's identity may be determined. How wavelength, angle, and interplanar spacing relate to satisfy Bragg's Law is clearly shown if Figure 5.17.

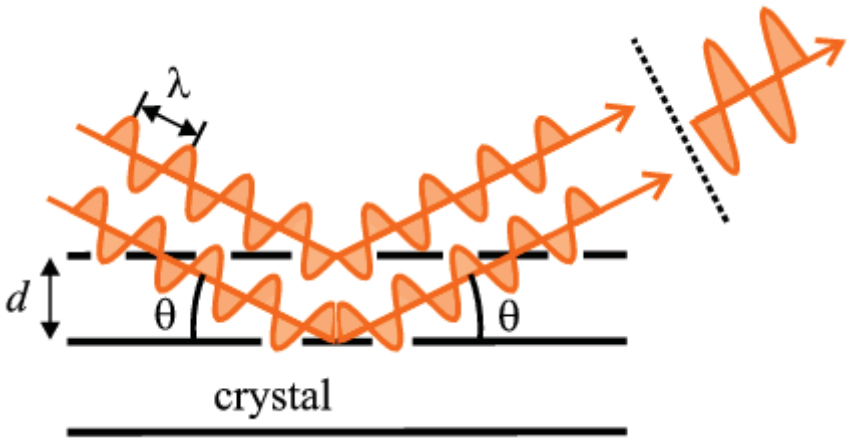

Figure 5.17: Relationship between wavelength, interplanar spacing, and angle in XRD [71].

All X-ray diffraction data in this thesis was attained on a Bruker D8 or Rigaku Miniflex diffractometer. Both utilize Cu-K_α radiation and all diffraction patterns were assessed using Bruker DIFFRAC.EVA software. This allowed for thorough characterization and phase identification of the TCON composites and precursors.

5.5.3 Scanning Electron Microscopy (SEM)

Scanning electron microscopy is an exceptional tool for viewing materials on the micro- and nanoscale. Unlike light microscopy, which uses visible light for imaging, this method utilizes an electron beam. Having significantly smaller wavelengths than visible light, electrons can provide exceptionally high magnifications exceeding 100,000x. The interpenetrating phase composites described in this thesis were imaged exclusively with an SEM. In particular, a JEOL JIB-4500 Multi Beam System with LaB_6 filament (Fig. 5.18).

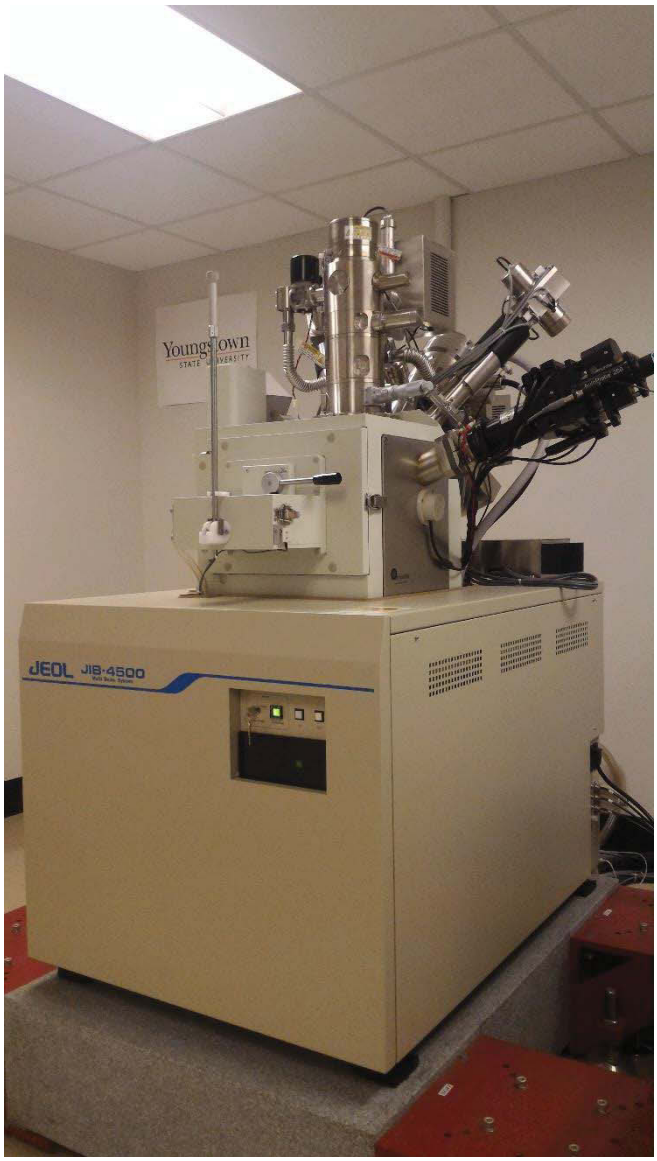

Figure 5.18: JEOL JIB-4500 Multi Beam System Scanning Electron Microscope with LaB_6 filament.

The high magnification of an SEM allowed for visualization of the micro-scale ceramic and metal phases in TCON composites. While the specific designs of each microscope vary, there are many features standard to all. All scanning electron microscopy, for example, begins with an electron gun (Fig. 5.19). This produces the

stable beam of electrons needed for imaging. As these electrons move down the optical column, they encounter a series of electromagnetic lenses. First and second are condenser lenses, which reduce the diameter of the beam and determine spot size [74, 75]. When one refers to "spot size" in scanning electron microscopy, this corresponds to the diameter of the electron beam where it hits the surface of a sample. By decreasing spot size, we decrease the size of the area being analyzed during each scan.

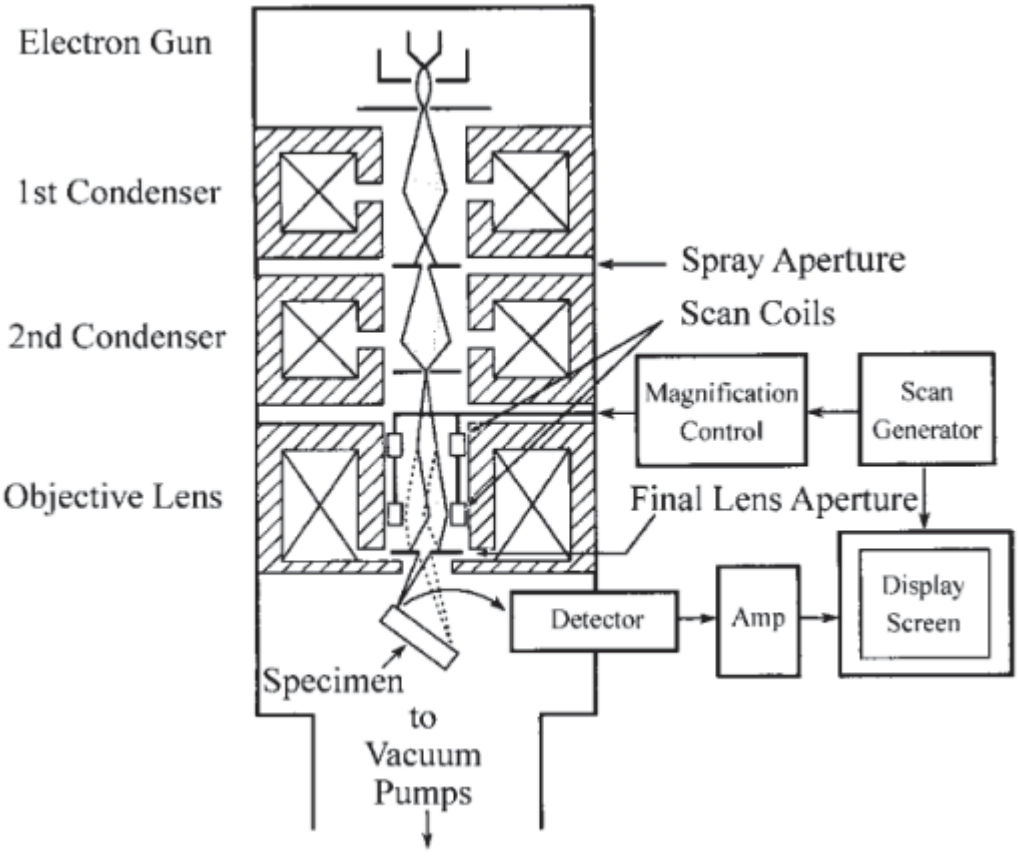

Figure 5.19: Cross-sectional view of a scanning electron microscope [75].

The last electromagnetic lens the electron beam encounters is the objective lens. This produces demagnification the beam and serves to focus it [74, 75]. The beam—now focused—must pass through a final aperture before it reaches the sample. The diameter of

this aperture dictates the angle at which the beam encounters the specimen being analyzed. This is referred to as the convergence angle, α. These parameters are varied depending on the type of analysis being done. Topographical analysis, for example, utilizes small aperture and convergence angle because it provides an increased depth of field.

It is important now to note that electron microscopy occurs under vacuum. Electrons will interact with anything they come in contact with, causing a rapid loss in energy. The high vacuum produces an unobstructed path from electron gun to sample, allowing for interaction of beam electrons with sample atoms alone. This interaction serves as the basis for all imaging in a scanning electron microscope.

As the electron beam strikes a sample, it will penetrate into its bulk. This typically occurs to a depth of ~1 μm and the three dimensional region effected is referred to as the interaction volume [76]. Different regions of the interaction volume are responsible for five types of signals: secondary electrons, backscattered electrons, characteristic X-rays, auger electrons, and cathodoluminescence [77]. A depiction of interaction volume and the regions corresponding to the first three signals is presented in Figure 5.20.

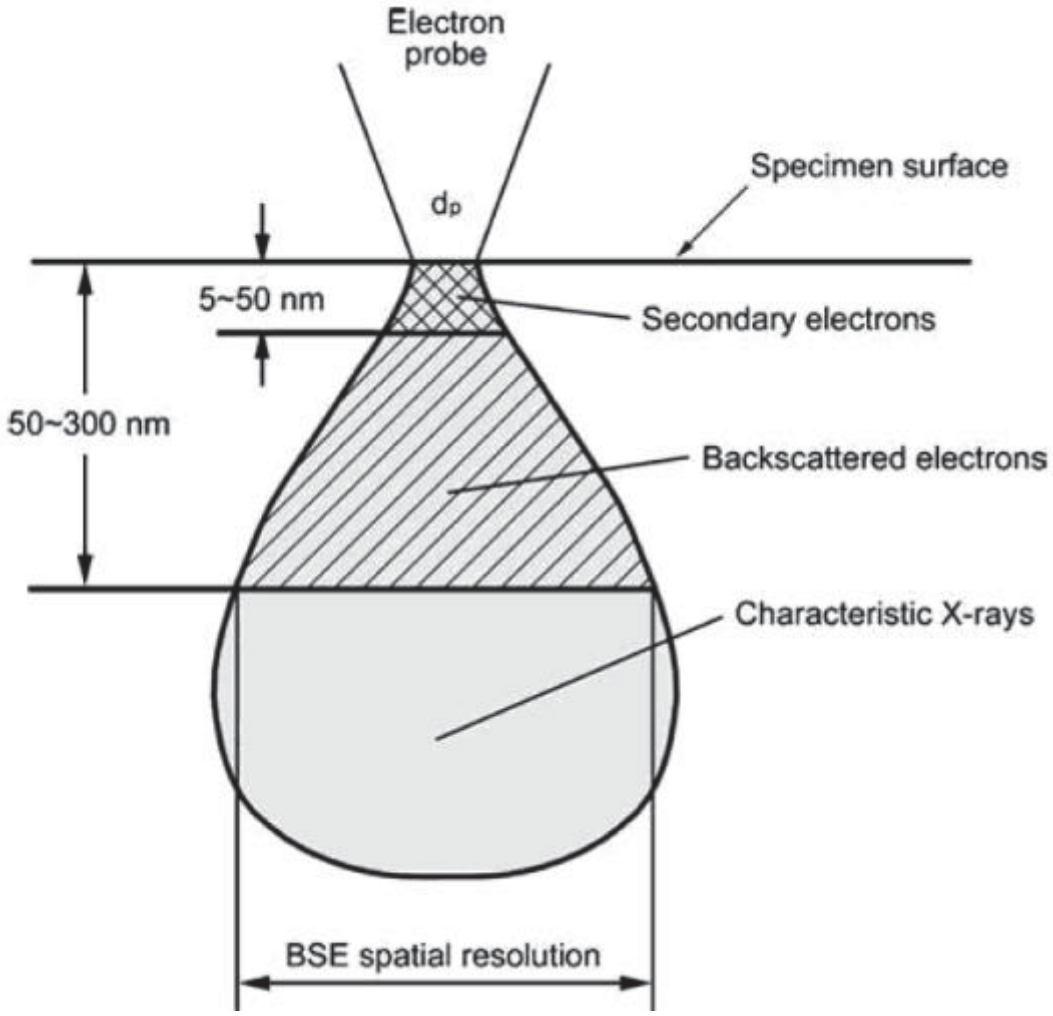

Figure 5.20: Interaction volume in scanning electron microscopy [75].

Scanning electron microscopes produce images using secondary and backscattered electrons. The former arise when beam electrons interact inelastically with the sample. This knocks sample electrons from their original positions [75]. Backscattered imaging, in contrast, is the result of elastic interactions that cause incident electrons to be scattered by sample atoms. Individual detectors are required for each type of signal, and Figure 5.21 shows the interactions between beam electrons and sample atoms for both.

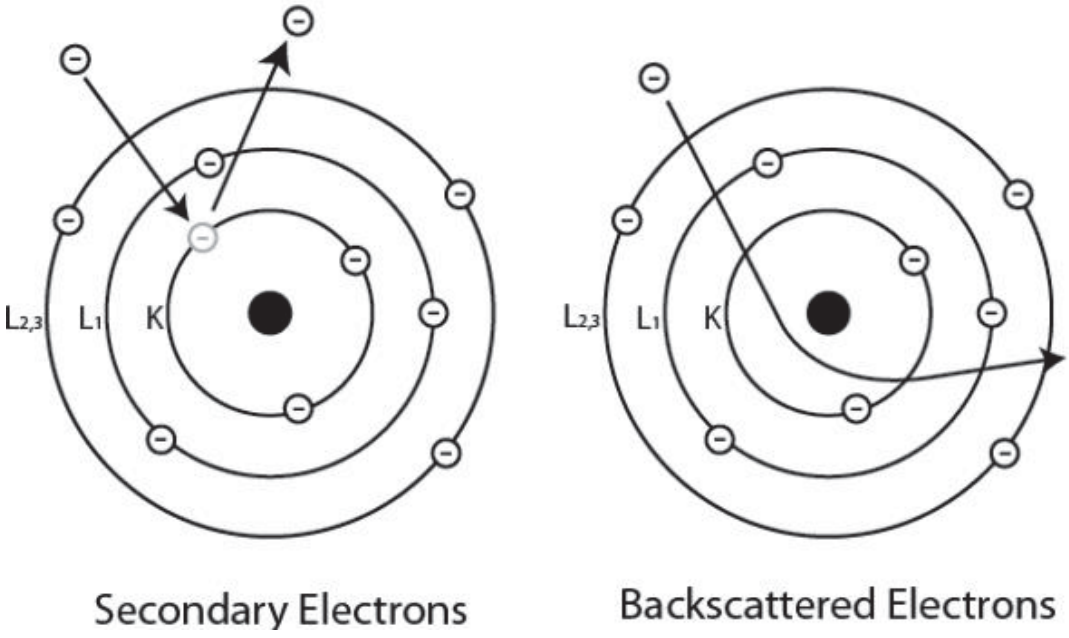

Figure 5.21: Interactions between the electron beam and sample atom in SEM [78].

Primarily, secondary electrons are used for topographical studies due to their short escape depths. The composites mentioned in this thesis were polished to a flat surface before imaging, so there was little use for topographical analysis. As a result, backscattered electrons were used for characterization of all interpenetrating phase composites. This provided compositional information as brightness is dependent on the average atomic number of each constituent phase. The phase with the higher average atomic number produces greater numbers of BSE, which leads to that phase appearing brighter than its lower average atomic number counterpart. The greater depths from which backscattered electrons arise also produces better information about a sample's bulk. This was particularly valuable in assessing the compositions and microstructures of TCON composites.

5.5.4 EDAX

The JIB-4500 SEM comes equipped with a system to perform energy-dispersive X-ray spectroscopy. The specific instrument used for analysis here was an EDAX Apollo XV system. It collects X-rays produced during interactions between a sample and the electron beam. If an electron of sufficient energy hits a sample atom, an inner shell electron may be knocked from its position in that atom. When the electron leaves the atom becomes ionized, and to return to the normal state an outer shell electron must fill the inner shell vacancy [75]. As a result, an X-ray photon is generated from the energy difference between the outer and inner shell electrons [75]. The energy of such X-rays is characteristic to the element being studied. As no two elements have the same atomic number, the identities of elements in a sample may be determined by measuring the energy of the X-ray produced. Mosely's Law (Equation 5.3) relates the atomic number to characteristic X-ray wavelength [75]. Furthermore, the atomic interactions that cause X-ray emissions are presented in Figure 5.22. This technique was used extensively when analyzing the microstructure of the IPCs formed.

Equation 5.3: $\lambda = \frac{B}{(Z-\sigma)^2}$

B & σ = Constants Depending on Specific Shells

λ = Wavelength

Z = Atomic Number

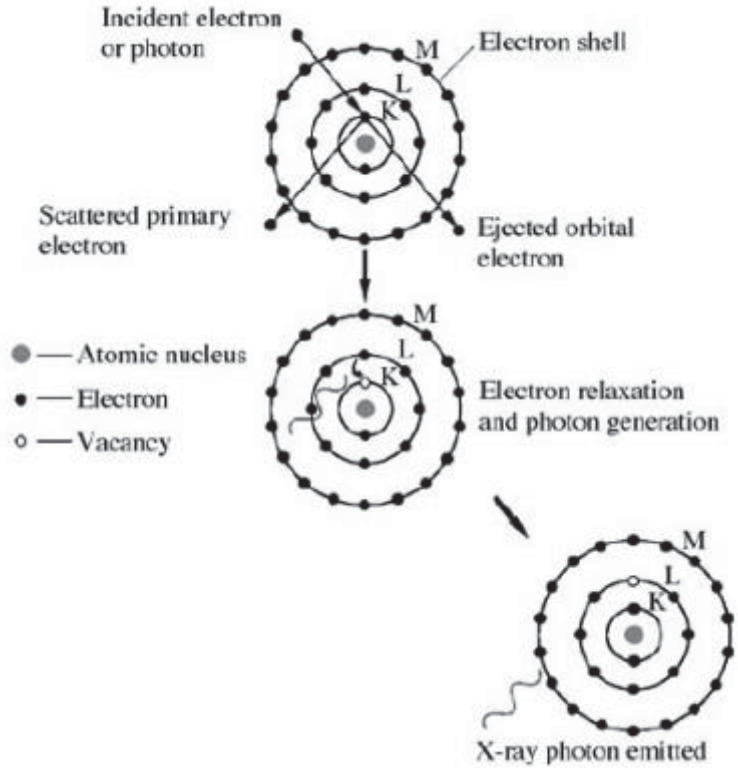

Figure 5.22: X-ray photon emission resulting from interactions between an electron and a sample atom. [75].

5.5.5 Compression Testing

The C-precursors were transformed in Fireline's kilns according to the procedure described in Section 5.4.2.2. Three of these transformed materials were subjected to compression testing. Such was done on an Instron 5500R (Fig. 5.23), and the load (N) was plotted as a function of extension (mm).

Figure 5.23: Compression testing of $MgAl_2O_4$/Al composites with the pellet itself marked with a red arrow in (B).

The load at which the sample failed is known as the maximum load, and from that one can calculate compressive strength using Equation 5.4.

Equation 5.4: $Compressive\ Strength\ (MPa) = \frac{Maxium\ Load\ (N)}{Surface\ Area\ (mm^2)}$

Chapter 6
Results & Discussion

6.1 SiAlON Preforms

6.1.1 Ball Milled Precursors

In the previous chapter, Section 5.3.1.1 described the production of β-SiAlON by high-energy ball milling and reactive sintering. That procedure, unlike all others presented, was very specific as to the masses of reagents used. This is due to the method's success being limited to an exceedingly small scale. Attempts were made to mill a powder mixture totaling 5 grams and all attempts failed. The ability to produce only ~2 grams of SiAlONs at one time makes this a very unfavorable synthesis for industrial applications. Furthermore, the significant time required for milling (18 hours) was incredibly damaging to the zirconia sample vial and milling balls. For these reasons, this preform was neither transformed or investigated further.

6.1.2 SiAlONs Produced via Reactive Sintering

Despite an inability to synthesize a precursor composed solely of $SiAl_2O_2N_2$, the pellets synthesized in Section 5.3.1.2 were selected for transformation in a tube furnace. However, such transformation proved to be an overwhelming failure. Even after 60 hours of transformation, there were still large areas of unreacted ceramic in the composites formed from Precursors S2 and S3. These areas were in plain view when the materials were cut to expose their cross sections. No unreacted regions were seen in the cross section of the composite produced from Precursor S1, however it cannot be ruled out that they are present in other parts of the pellet. In any case, because these precursors require

an exceptionally long transformation time they are not considered suitable for industrial applications.

More importantly, none of the three preforms yielded AlON upon transformation. The results—regardless of elemental silicon concentrations—were identical: alumina, aluminum nitride, and aluminum. No variation was found, regardless of whether the composite was produced from Precursor S1 (Fig. 6.1), S2 (Fig. 6.2), or S3 (Fig. 6.3).

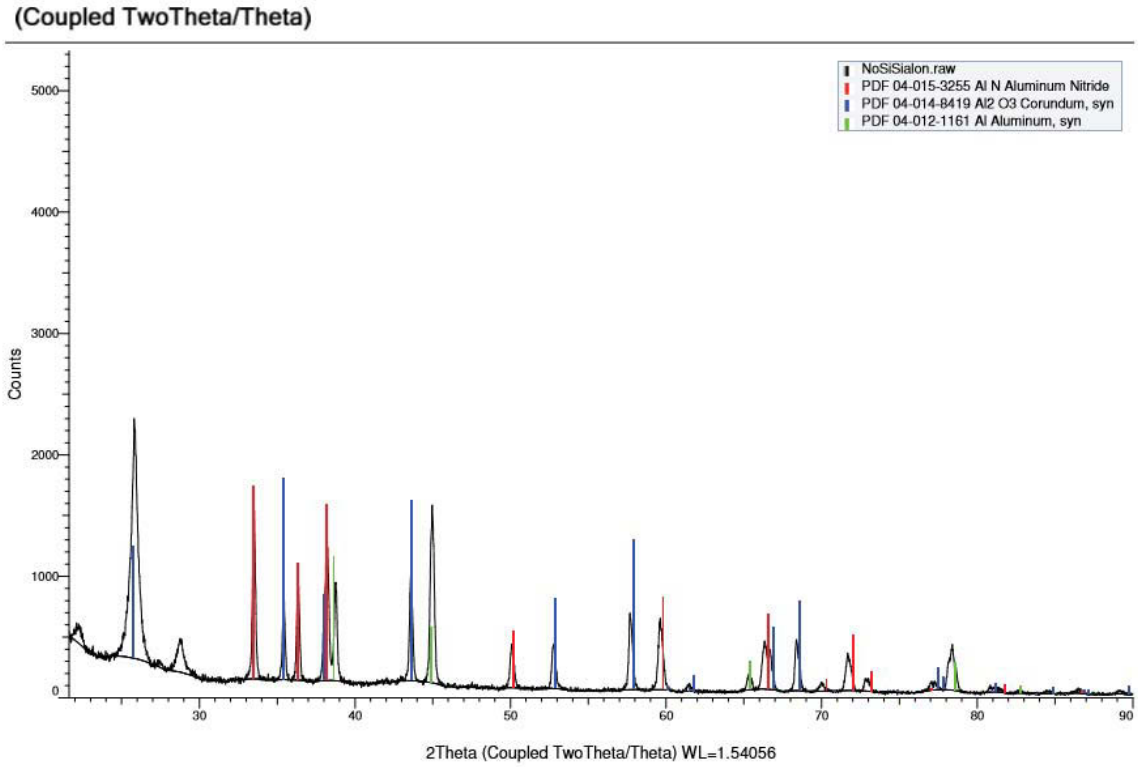

Figure 6.1: XRD pattern taken from the completely transformed pellet surface of the composite produced by transformation of the SiAlON containing no elemental silicon (Precursor S1).

- AlN, 04-015-3255, Hexagonal, P63mc (186), a = 3.09000 Å, c = 4.94400 Å
- Al_2O_3, 04-014-8419, Rhombo.H.axes, R-3c (167), a = 4.73500 Å, c = 12.89900 Å
- Al, 04-012-1161, Cubic, Fm-3m (225), a = 4.03400 Å

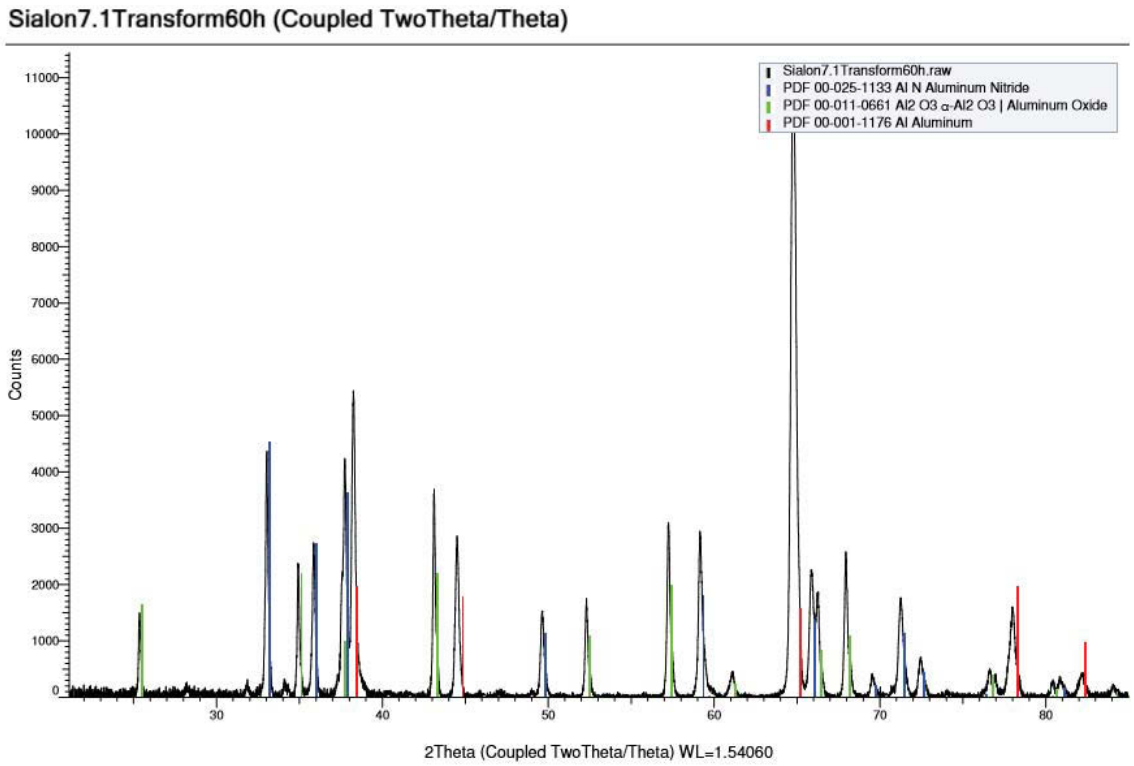

Figure 6.2: XRD pattern taken from the completely transformed pellet surface of the composite produced by transformation of the SiAlON containing stoichiometric amounts of elemental silicon (Precursor S2).

- AlN, 00-025-1133, Hexagonal, P63mc (186), a = 3.11140 Å, c = 4.97920 Å
- Al, 00-001-1176, Cubic, Fm-3m (225), a = 4.04060 Å
- Al_2O_3, 00-011-0661, Rhombo.H.axes, R-3c (167), a = 4.75900 Å, c = 12.99100 Å

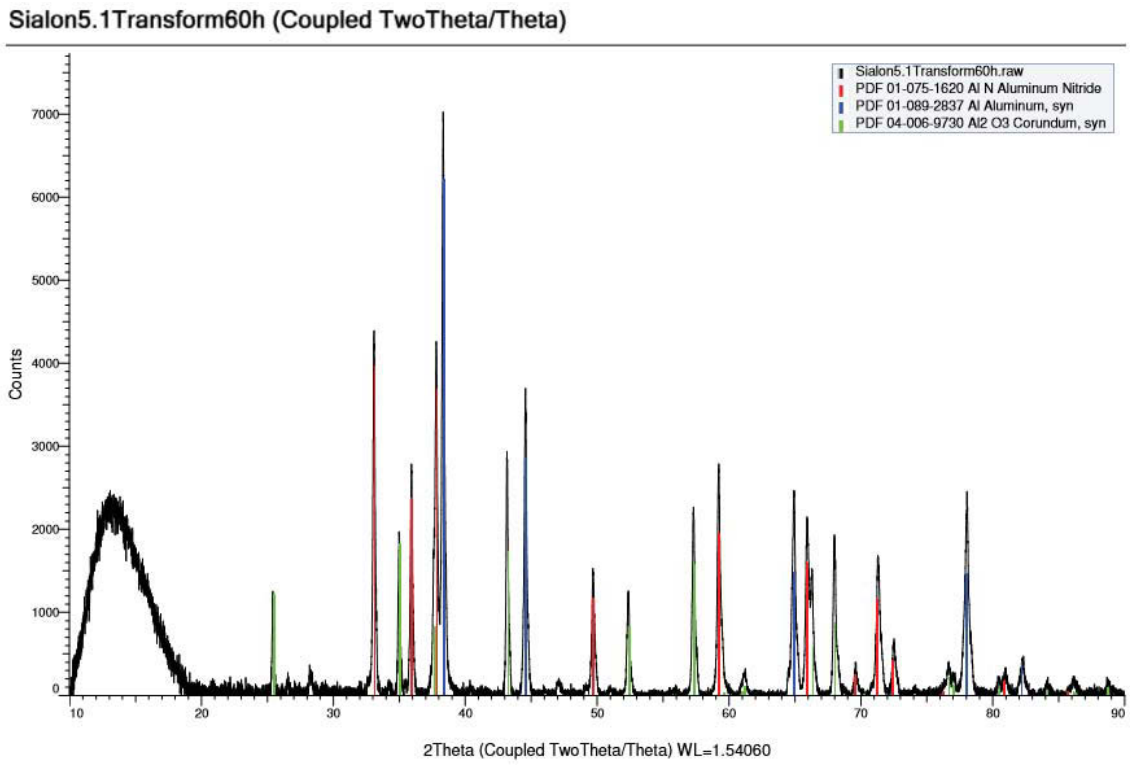

Figure 6.3: XRD pattern taken from the completely transformed pellet surface of the composite produced by transformation of the SiAlON containing a 50% excess of elemental silicon (Precursor S3).

- AlN, 01-075-1620, Hexagonal, P63mc (186), a = 3.11900 Å, c = 4.99100 Å
- Al, 01-089-2837, Cubic, Fm-3m (225), a = 4.05925 Å
- Al_2O_3, 04-006-9730, Rhombo.H.axes, R-3c (167), a = 4.76900 Å, c = 13.02090 Å

The reasons for AlON's failure to form may be understood by viewing the AlN/Al_2O_3 phase diagram in Figure 6.4. There, one will notice that below 1700℃ the only AlON that may form is the γ-phase. The composition of this is $Al_{23}O_{27}N_5$. Obviously, this is far from the desired Al_3O_3N spinel. It is now believed that the phase diagram presented in Figure 5.3 was incorrect.

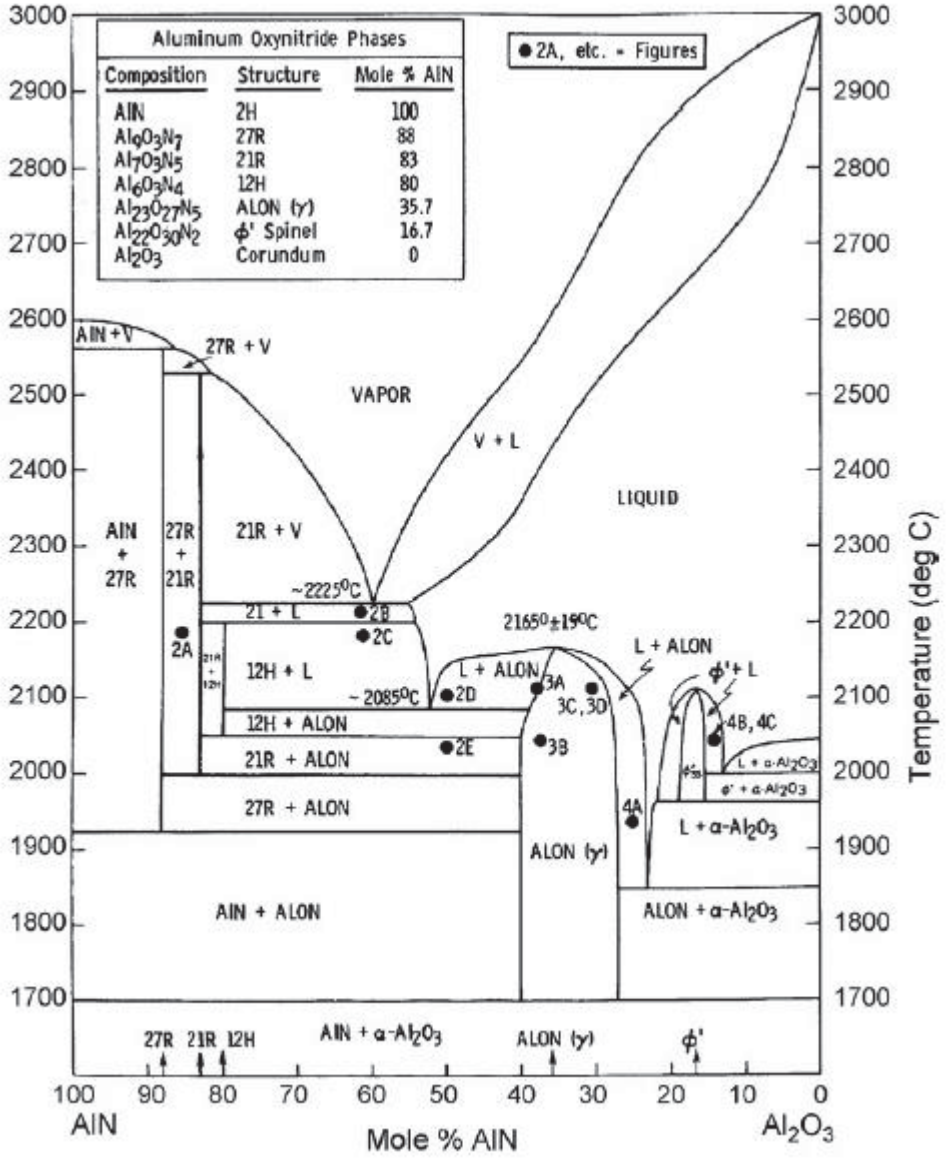

Figure 6.4: Phase diagram of aluminum nitride and alumina [79].

The correct phase diagram (Fig. 6.4) does not support the use of $SiAl_2O_2N_2$ for the TCON process. AlON may form at all temperatures above 1700℃, but this is not achievable in Fireline's kilns. There, the maximum transformation temperature is 1200℃. Even if these high temperatures were achievable, the significantly long transformation

times would still prevent SiAlON's use. For these reasons, SiAlONs were abandoned as a TCON precursor material.

6.2 MgAl2O4 Precursors

6.2.1 Furnace Transformation

The preforms described in Section 5.3.2.1.1 were transformed in four different melts simultaneously. By varying only metal compositions and keeping all other parameters constant, one may gain significant insight as to how the metal bath affects the microstructure and compositions of the final composites. In general, the transformations described in Section 5.2.4.1 were an overwhelming success. Table 6.1 presents the results of each of the four reactions. From this data, as well as the SEM images presented, the best set of reaction conditions for further trials could be chosen.

Reaction Conditions of $2MgTiO_3/SiO_2$ Transformation	Resulting Composite
100% Al, 1200℃, 22 Hours	$MgAl_2O_4$, Al_2O_3, Al, $TiAl_3$
95% Al, 5% Si, 1200℃, 22 Hours	$MgAl_2O_4$, Al, $MgAl_2Si_2$
95% Al, 5% Mg, 1200℃, 22 Hours	$MgAl_2O_4$, Al, $TiAl_3$, Si
95% Al, 5% Ti, 1200℃, 22 Hours	$MgAl_2O_4$, Al, $TiAl_3$

Table 6.1: Results of the furnace transformation of $MgTiO_3$ and amorphous SiO_2 gel.

As one can see, the 100% aluminum melt was the only transformation that did not produce spinel as the sole ceramic phase. Alumina, of course, is undesired, and it was present in the final composite's XRD pattern (Fig. 6.5).

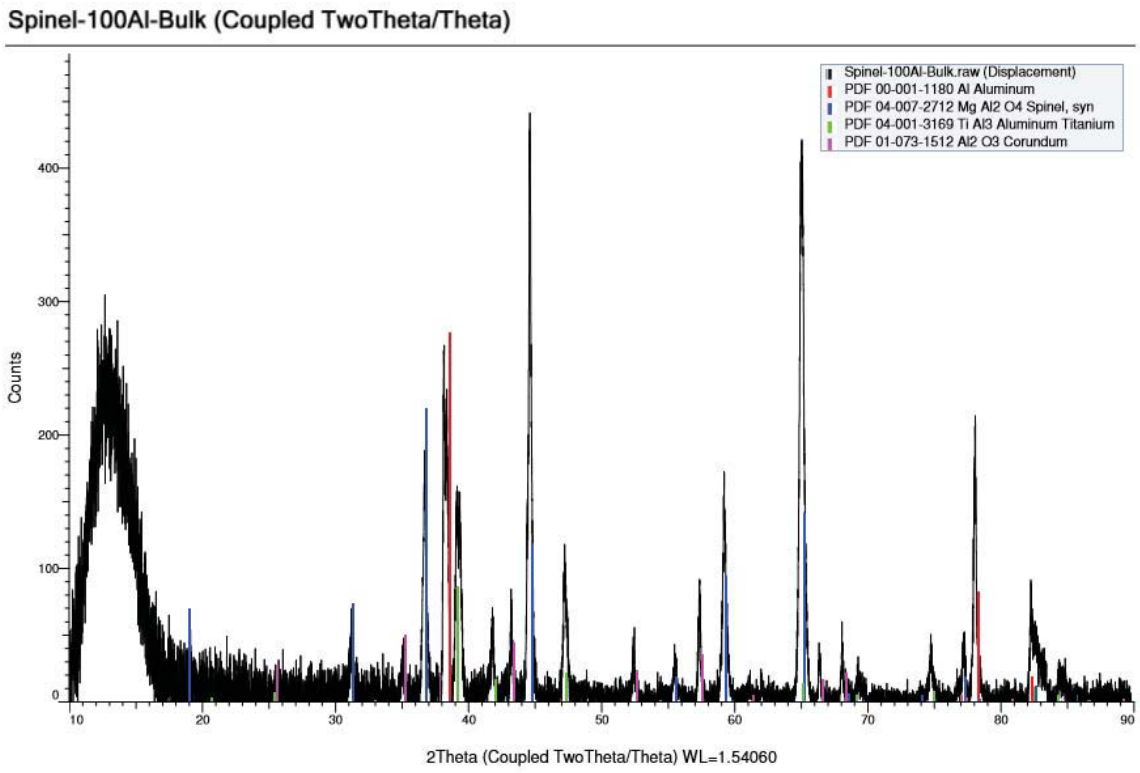

Figure 6.5: XRD pattern of composite formed by transformation of $MgTiO_3$ and SiO_2 gel in a 100% Al melt.

- Al, 00-001-1180, Cubic, Fm-3m (225), a = 4.04060 Å
- $MgAl_2O_4$, 04-007-2712, Cubic, Fd-3m (227), a = 8.08580 Å
- $TiAl_3$, 04-001-3169, Tetragonal, I4/mmm (139), a = 3.84000 Å, c = 8.59000 Å
- Al_2O_3, 01-073-1512, Rhombo.H.axes, R-3c (167), a = 4.75050 Å, c = 12.97030 Å

The three other IPCs showed variation primarily in the secondary metal phases. Powder X-ray diffraction proved that magnesium aluminate spinel was the only ceramic formed during RMP in the 5% Si (Fig. 6.6), 5% Mg (Fig. 6.7), and 5% Ti melts (Fig. 6.8).

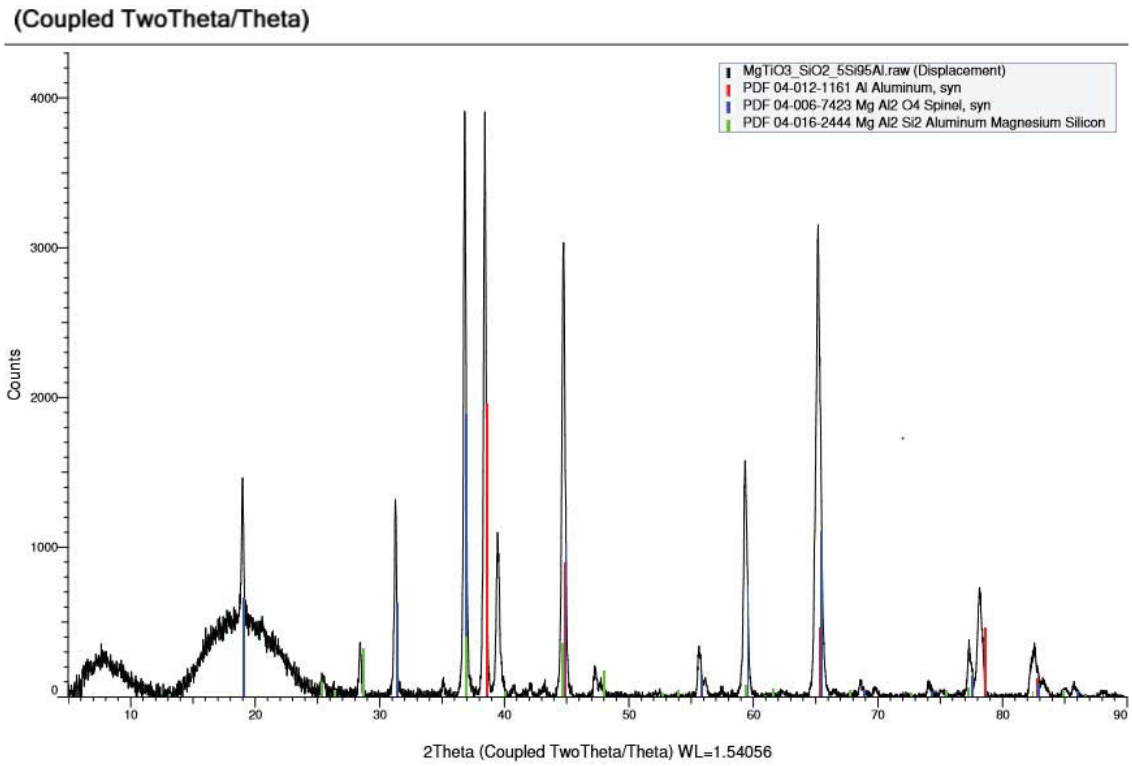

Figure 6.6: XRD pattern of composite formed by transformation of $MgTiO_3$ and SiO_2 gel in a 95% Al, 5% Si melt.

- Al, 04-012-1161, Cubic, Fm-3m (225), a = 4.03400 Å
- $MgAl_2O_4$, 04-006-7423, Cubic, Fd-3m (227), a =8.06000 Å
- $MgAl_2Si_2$, 04-016-2444, Hexagonal, P-3m1 (164), a = 4.05000 Å, c = 6.74000 Å

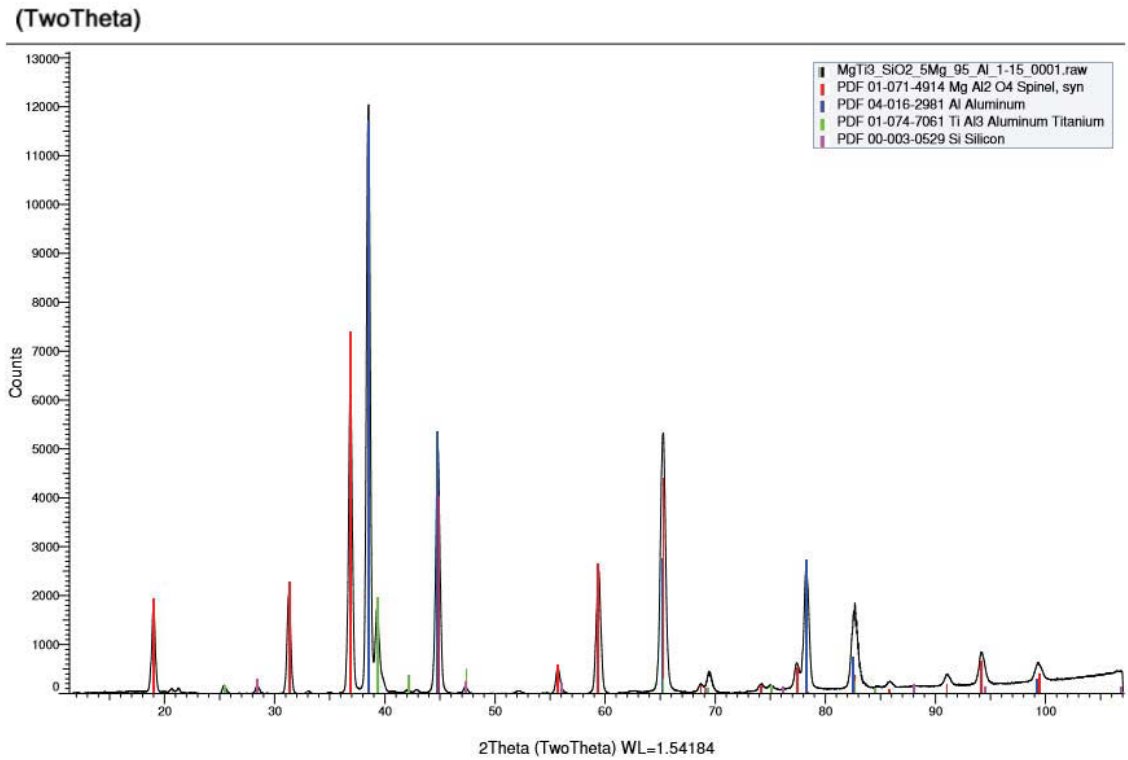

Figure 6.7: XRD pattern of composite formed by transformation of $MgTiO_3$ and SiO_2 gel in a 95% Al, 5% Mg melt.

- $MgAl_2O_4$, 01-071-4914, Cubic, Fd-3m (227), a = 8.08600 Å
- Al, 04-016-2981, Cubic, Fm-3m (225), a = 4.04980 Å
- $TiAl_3$, 01-074-7061, Tetragonal, F4/mmm (139), a = 5.42500 Å, c = 8.87900 Å
- Si, 00-003-0529, Cubic, Fd-3m, a = 5.43040 Å

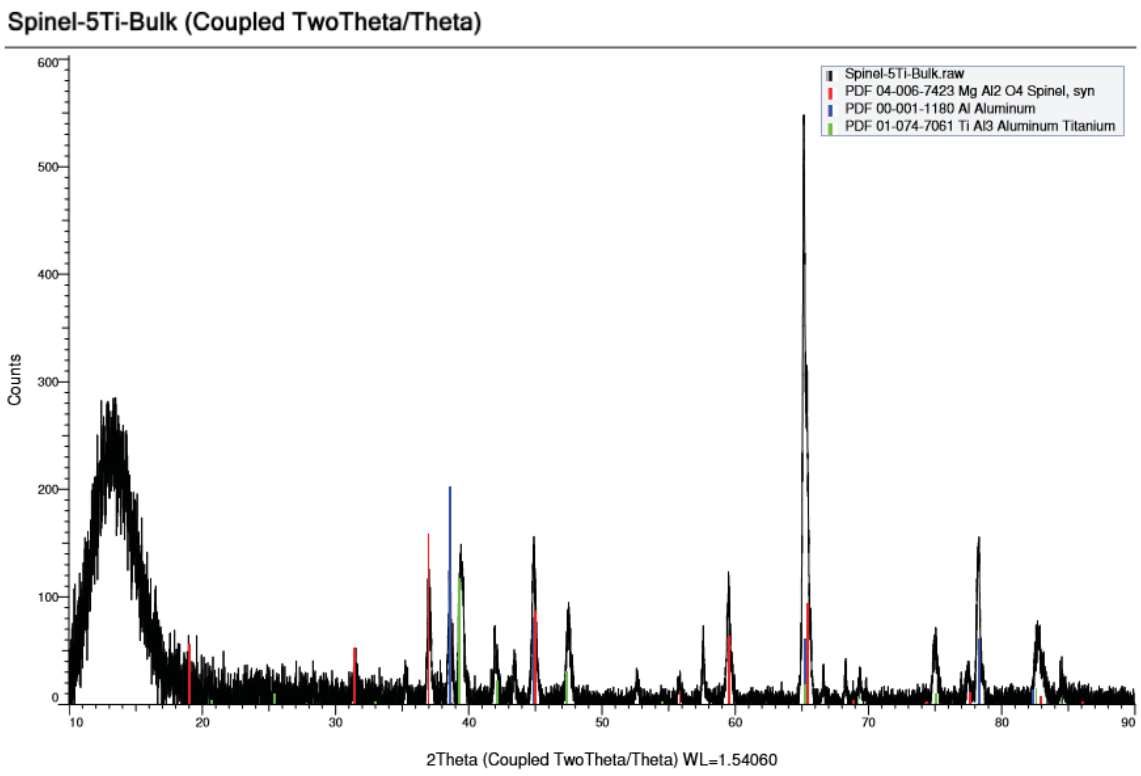

Figure 6.8: XRD pattern of composite formed by transformation of $MgTiO_3$ and SiO_2 gel in a 95% Al, 5% Ti melt.

- $MgAl_2O_4$, 04-006-7423, Cubic, Fd-3m (227), a = 8.06000 Å
- Al, 00-001-1180, Cubic, Fm-3m (225), a = 4.04060 Å
- $TiAl_3$, 01-074-7061, Tetragonal, F4/mmm (139), a = 5.42500 Å, c = 8.57900 Å

The concentrations and compositions of these secondary metal phases are not considered significant. As aluminum is the primary metal and in much greater concentrations, the metal phases are not a deciding factor in determining which melt to continue on with. Kilns will have significantly larger melts, and the side metals—in theory—would be minimized. Furthermore, X-ray analysis for these side metals is considered unreliable. Many variations of silicon-titanium-aluminum alloys possess similar unit cells and

diffraction patterns. Often, there are multiple overlapping signals on said patterns, and the EVA software may not always accurately differentiate between the different alloys. For these reasons, the SEM and EDAX software were used to determine which melt yielded the best composite.

The polished cross sections of each composite are presented in Figure 6.9. One will immediately notice the cracks and deformation in all four. This is a result of the preforms' unsintered nature. However, despite their flaws, each precursor offered valuable information. This in not only in regards to whether a spinel IPC can form, but how the different melts effect diffusivity and composite microstructure. In the image below, one will notice arrows marking the diffusion lines. This line separates the two microstructures in each composite. Each microstructure, in turn, has unique compositions of metals. Notice the diffusion line of the 5% Si composite is significantly higher than for the other three.

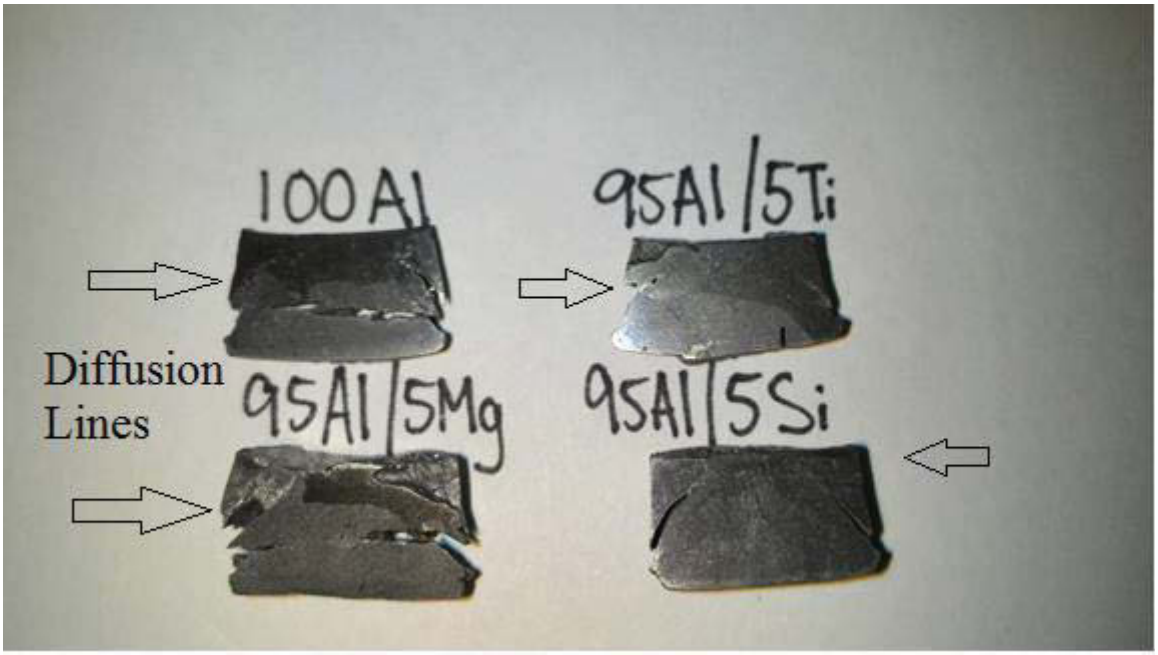

Figure 6.9: Cross sections of the 4 furnace-transformed MgAl2O4 composites and their diffusion lines.

Figure 6.10 presents the microstructures of each composite above and below their diffusion lines. These SEM images were taken at 400x magnification, and the constituent phases were identified by EDAX and labelled with colored dots. It is obvious to see that—regardless of melt composition—microstructures are uniform across all $MgAl_2O_4$/Al composites. Below the diffusion line, there exists primarily $MgAl_2O_4$ (green), Al (yellow), and Al-Si-Ti (pink). The latter typically fills large cracks in the ceramic that occurred during transformation. Such cracks are significantly larger than the interpenetrating networks of spinel and aluminum. Above the diffusion line, there is greater homogeneity in terms of the size of the constituent phases. No large cracks in the ceramic appear to have formed, and the phases are more interpenetrating. However, there is significant variation among the phases. Pure aluminum networks are not seen here, but rather alloys of aluminum with silicon, titanium, and/or magnesium. These by-produced metals did not have the chance to diffuse into the bath and became entrapped in the final composite. This then caused the distinct diffusion line and accompanying differences in microstructure.

One may notice that there exist unreacted areas of $MgTiO_3$ (purple) both above and below the diffusion line. This is due to newly-formed spinel (green) encapsulating particular grains of precursor. In the images below, all unreacted grains of $MgTiO_3$ are encased by solid shells of $MgAl_2O_4$, which act as a barrier to further transformation. These unreacted areas were few and far between, however, and were not taken into account when determining the conditions for future trials.

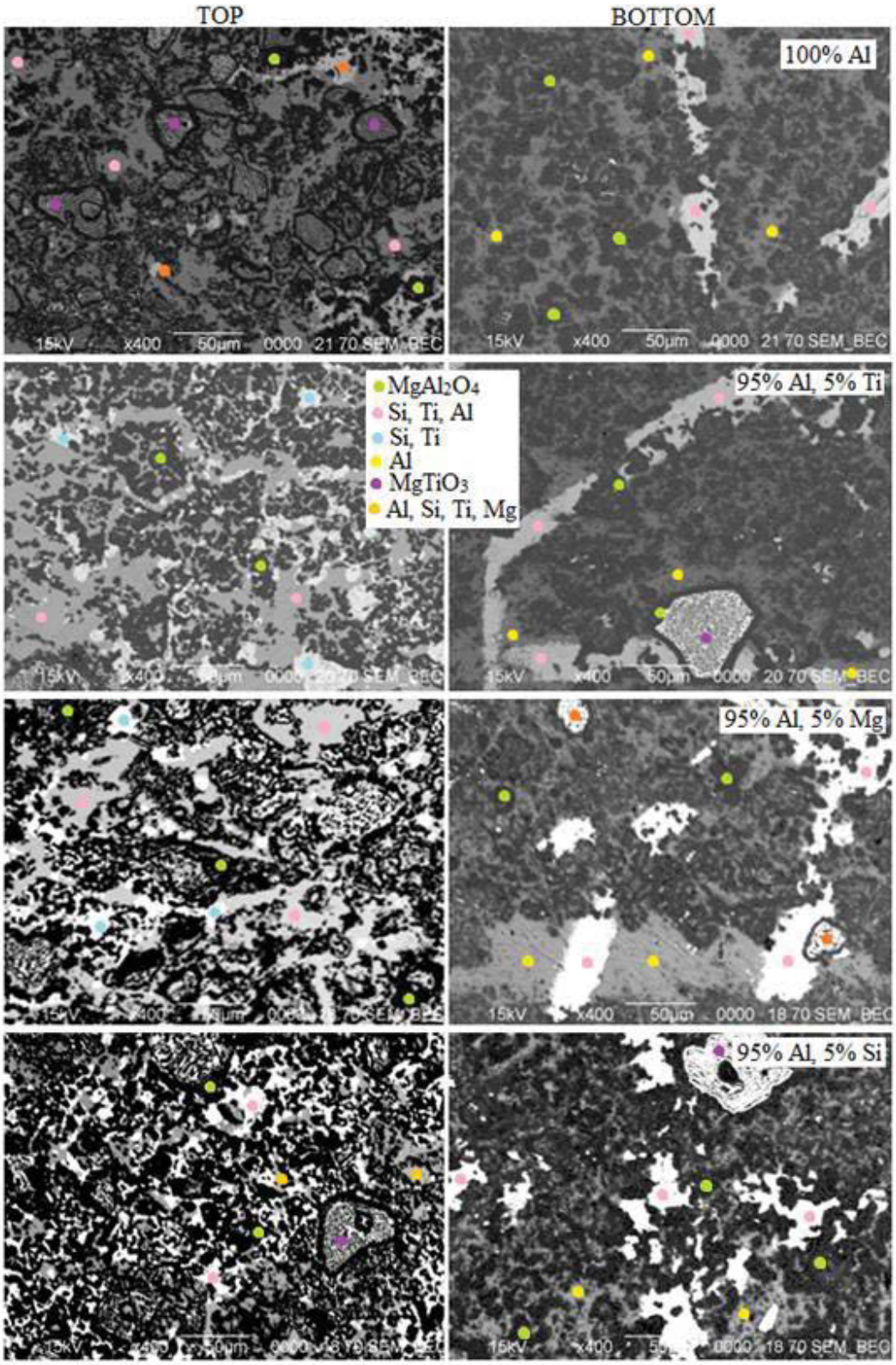

Figure 6.10: SEM images of the four furnace-transformed composites both above and below their respective diffusion lines.

In the ideal composite, there will exist a homogenous microstructure and minimal amounts of by-produced metals. For these reasons, the 5% silicon melt was chosen for further studies. It's diffusion line sat only a few millimeters from the pellet's top, meaning diffusivity occurred more quickly in this system. This resulted in a more consistent microstructure and smaller relative concentrations of the Si, Ti, and/or Mg alloys. Furthermore, the 5% Si melt is consistent with the work done by Kyle Myers [64].

6.2.2 Kiln Transformations

6.2.2.1 Effects of 3-D Printing

Sacrificial pellets were 3-D printed for transformation in Fireline's kilns. The printed powder mixtures were comprised of a 2:1 molar ratio of $MgTiO_3$ and either amorphous silica gel (G-precursors) or crystalline silica (C-precursors). Though the basic compositions, printing, and sintering processes were identical, the final preforms differed greatly. The effect these differences had on the transformed composites will be discussed in detail.

After sintering, each of the G- and C-precursors were weighed and measured. The average values for each material are presented in Table 6.2. The dimensions designated by the CAD file are present for comparison.

Parameter	CAD File	G-Precursors	C-Precursors
Radius (cm)	0.635	0.595	0.623
Height (cm)	0.635	0.623	0.653
Volume (cm3)	0.804	0.694	0.797
Mass (g)	-	0.887	1.275
Density (g/cm3)	-	1.278	1.602
%Volume Change	-	-13.656	-0.847

Table 6.2: Comparison of properties for sintered G- and C-precursors.

The most significant changes between CAD model and final shape occurred with the G-precursor. This can be primarily attributed to the amorphous nature of the silica. At high sintering temperatures, the amorphous silica undergoes a phase change to crystalline. This change is accompanied by an increase in density. Then, as one component of the precursor decreased in volume, so did the entire shape. This produces a 13% change in volume across the part. The crystalline silica undergoes no such phase change. As a result, volume and dimensions remain much more consistent between CAD model and final shape of the C-precursor.

Though sintering is often accompanied by a reduction in size and dimensions, one will notice that pellet height for the C-precursor actually increased. This is attributed to the "stickiness" of the binder. When pellets are removed from the print bed, excess powder clings to their exterior. Often, it is difficult to remove all residual powder. This is especially true at the pellets base, as the first printed layer of binder may drift downward into the bed. If excess powder sticks to the base and is not removed, it is incorporated into the preform's final shape during sintering. Hence; the increase in height for the C-precursor. This may also explain why radius changed to a greater extent in the G-precursor than height. However, because the change in dimensions in G-precursors is much more significant that the C-precursor there is still an overall decrease in height.

Perhaps the most significant property in Table 6.2 is preform density. Reactive metal penetration and the TCON process are both optimized by denser precursor material. Typically, this results in a higher ceramic content and finer microstructure. It is natural then to assume that the C-precursor, with its greater density, would provide a

composite with finer microstructure and grain sizes. However, in the next section, one will see that this may not be the case.

6.2.2.2 Final Composites

Having transformed the G- and C-precursors in Fireline's kilns, they were cut and polished for XRD and SEM analysis. It was found that these precursors produced magnesium aluminate as the sole ceramic phase regardless of the silica used. The difference between composites lay solely in the metal constituents. The IPC produced from the G-precursor—henceforth referred to as the G-spinel—contained Al_9Si in addition to the aluminum (Figure 6.11).

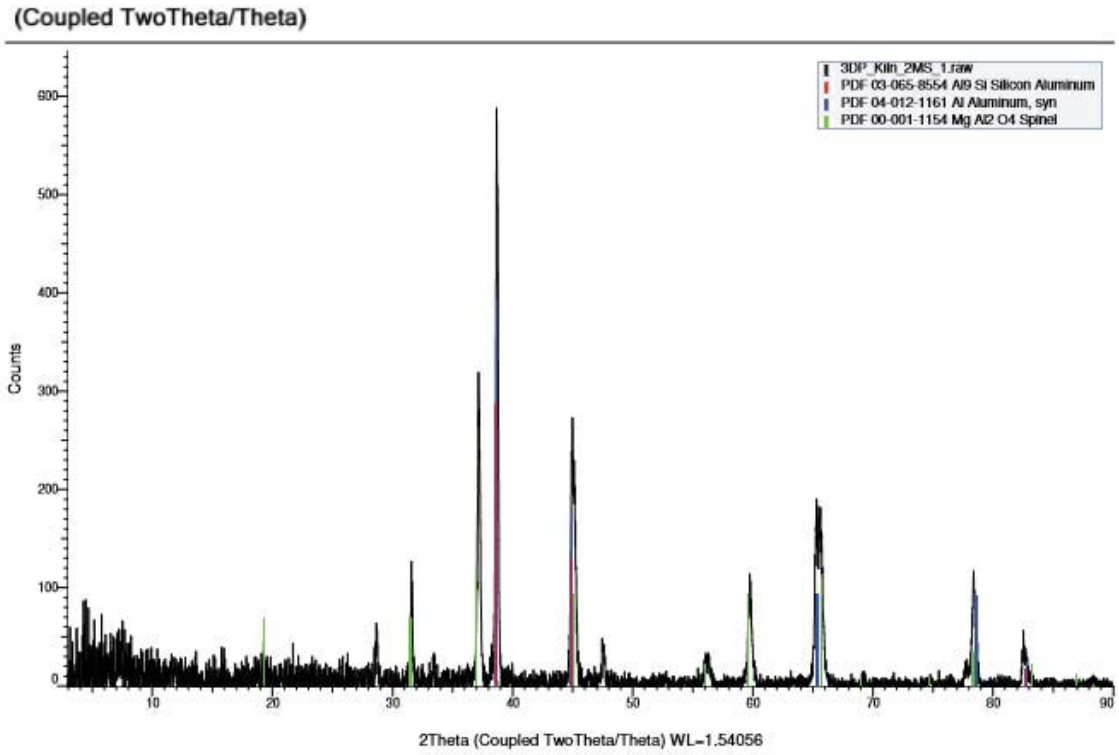

Figure 6.11: XRD pattern of composite formed from transformation of the G-precursor.

- Al_9Si, 03-065-8554, Cubic, Fm-3m (225), a = 4.03750 Å
- Al, 04-012-1161, Cubic, Fm-3m (225), a = 4.03400 Å
- $MgAl_2O_4$, 00-001-1154, Cubic, Fd-3m (227), a = 8.03000 Å

The composite produced from the C-precursor—henceforth referred to as the C-spinel—contained both silicon and $TiAl_{2.4}Si_{0.6}$ in small amounts (Figure 6.12).

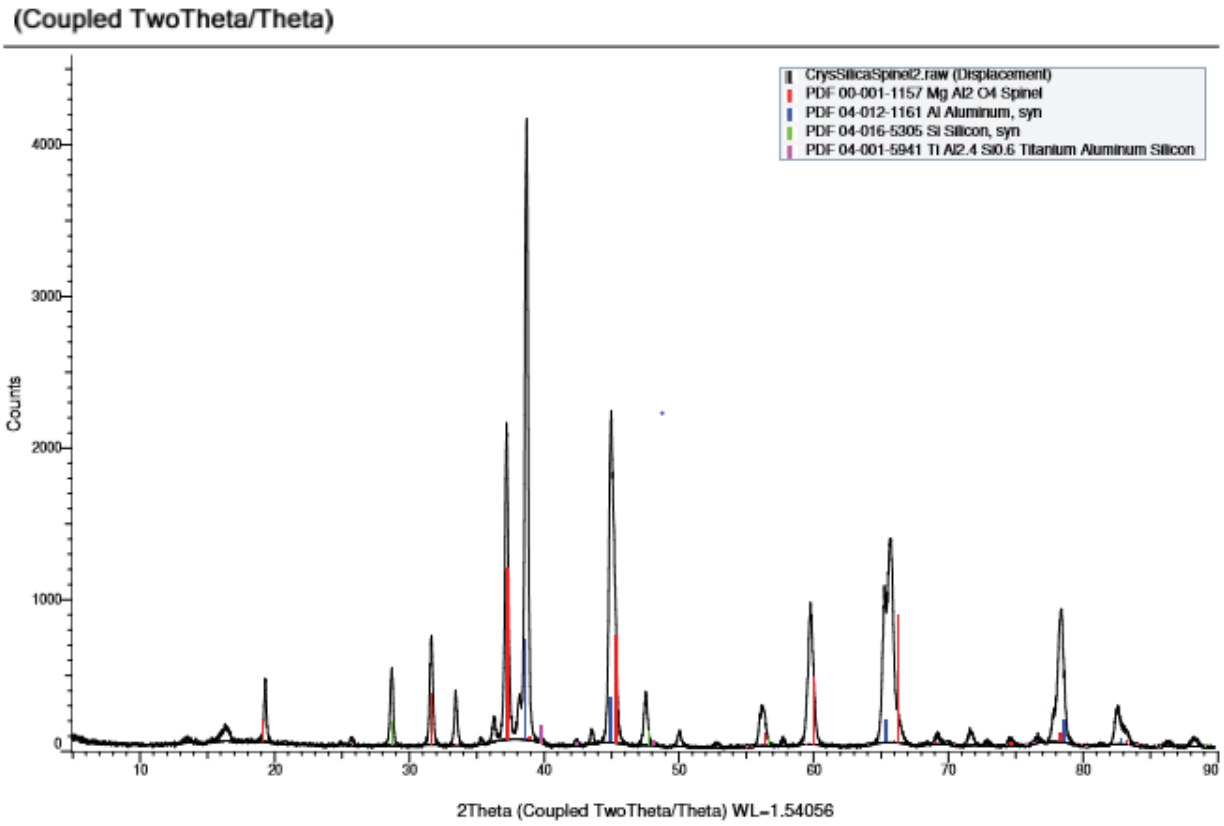

Figure 6.12: XRD pattern of composite produced via transformation of the C-precursor.

- $MgAl_2O_4$, 00-001-1157, Cubic, Fd-3m (227), a = 8.08600 Å
- Al, 04-012-1161, Cubic, Fm-3m (225), a = 4.03400 Å
- Si, 04-016-5305, Cubic, Fd-3m (227), a = 5.38100 Å
- $TiAl_{2.4}Si_{0.6}$, 04-001-5941, Tetragonal, I4/mmm (139), a = 3.78000 Å, c = 8.52000 Å

The reason for these differing metal contents is uncertain. As the preforms were transformed in identical melts under identical conditions, there was no external factor that would have effected metal composition. The differences in XRD patterns were likely the result of the EVA software failing to differentiate between similar compounds. This is, of course, in accordance with the furnace-transformed composites. Furthermore, the additional metal phases are in small enough concentrations relative to aluminum that they are not believed to cause significant differences between the composites

Comparison of these G- and C-spinels is best done with a scanning electron microscope. Figure 6.13 compares images taken of both composites at 270x magnification. Though XRD showed different metal constituents, the EDAX results were very consistent. Both materials contained the interpenetrating networks of spinel and aluminum, in addition to pools of Al-Si-Ti.

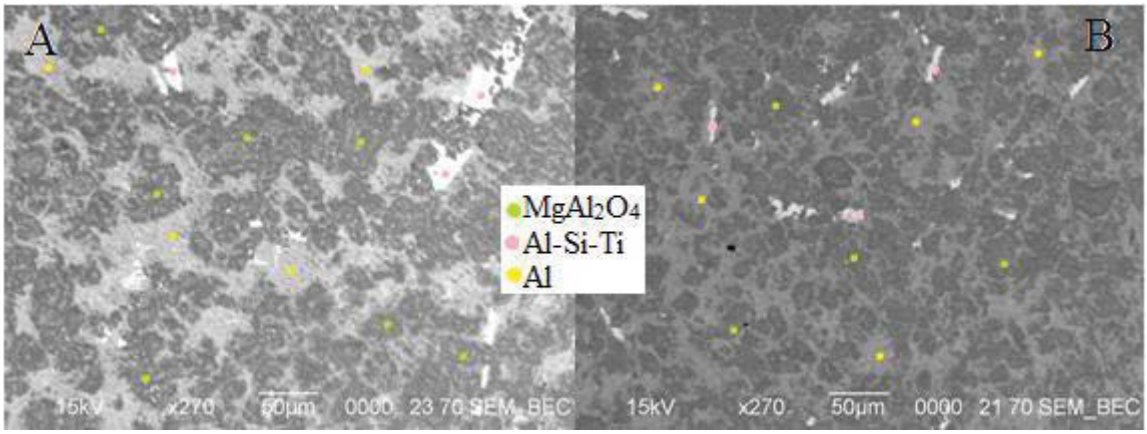

Figure 6.13: SEM images taken at 270x magnification for the (A) C-spinel, and (B) G-spinel composites.

The elemental mapping capabilities of EDAX also showed the compositional similarities (Figure 6.14). However, these maps also show the differences in relative amounts of

ceramic and metal. The C-spinel—which is formed from the higher density C-precursor—displays more of the ceramic phase (green and red). The less dense G-precursor produced more significant amounts of aluminum (blue) in the final composite.

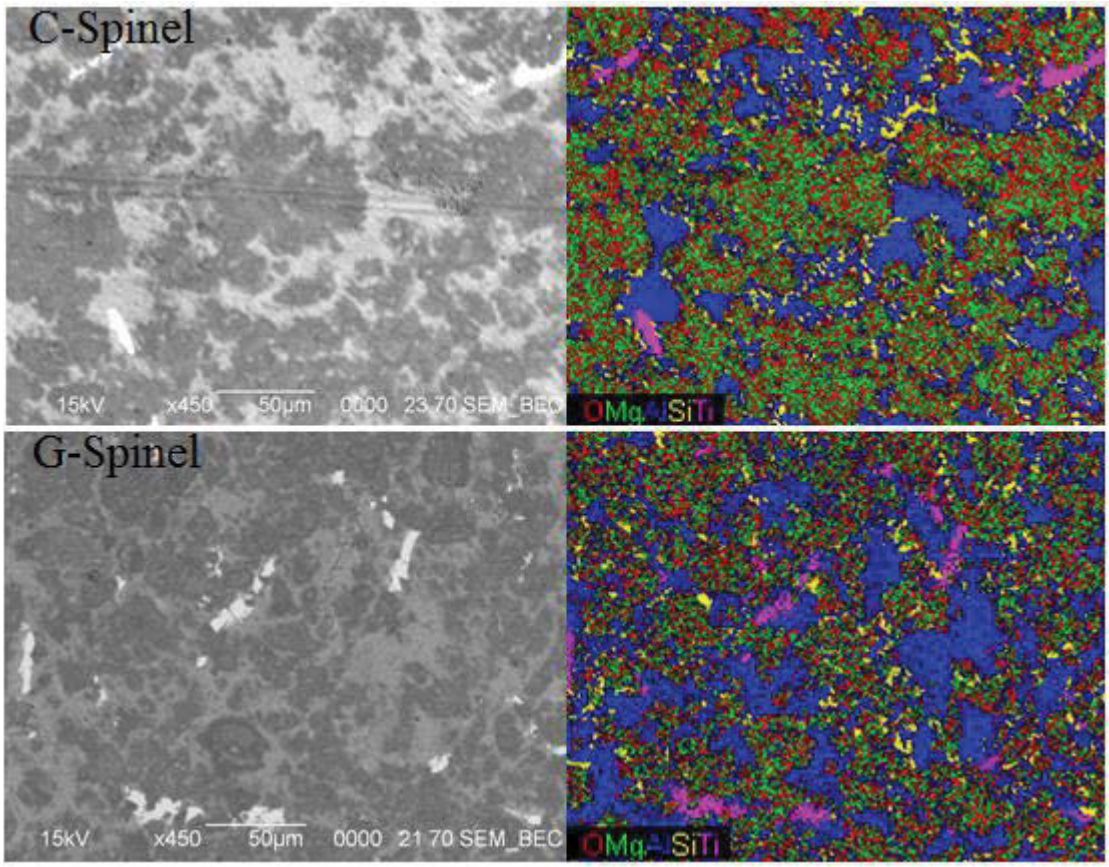

Figure 6.14: SEM images (left) and element maps (right) for the C- and G-spinels taken at 450x magnification.

In viewing these SEM images, one may also notice the difference in average ligament diameter for the ceramic and metal phases. The G-spinel depicts much finer grain sizes, as well as smaller pools of Al-Si-Ti. Having mentioned in Chapter 3 that decreasing grain size increases yield stress, it is easy to see why this is desirable. However, one must weigh the pros and cons before choosing whether to use crystalline or

amorphous silica in their spinel precursor. Decreasing metal content may lead one to choose the former. If small grain size is desired, the latter may prove better.

The most interesting images acquired on the SEM show the effect of 3-D printing on final composite microstructure. In Figure 6.15, one will notice a series of parallel metal channels crossing the composite. The distance between such lines was found to be, on average, 90-100 µm. This, of course, corresponds to the layer height chosen for 3-D printing: 100 µm. The areas once occupied by binder now correspond to linear metal channels throughout the IPC. While this was very obvious in the C-spinel, it is a trait absent in the G-composite. This is believed to result from the differing effects of binder in the crystalline silica opposed to its amorphous counterpart.

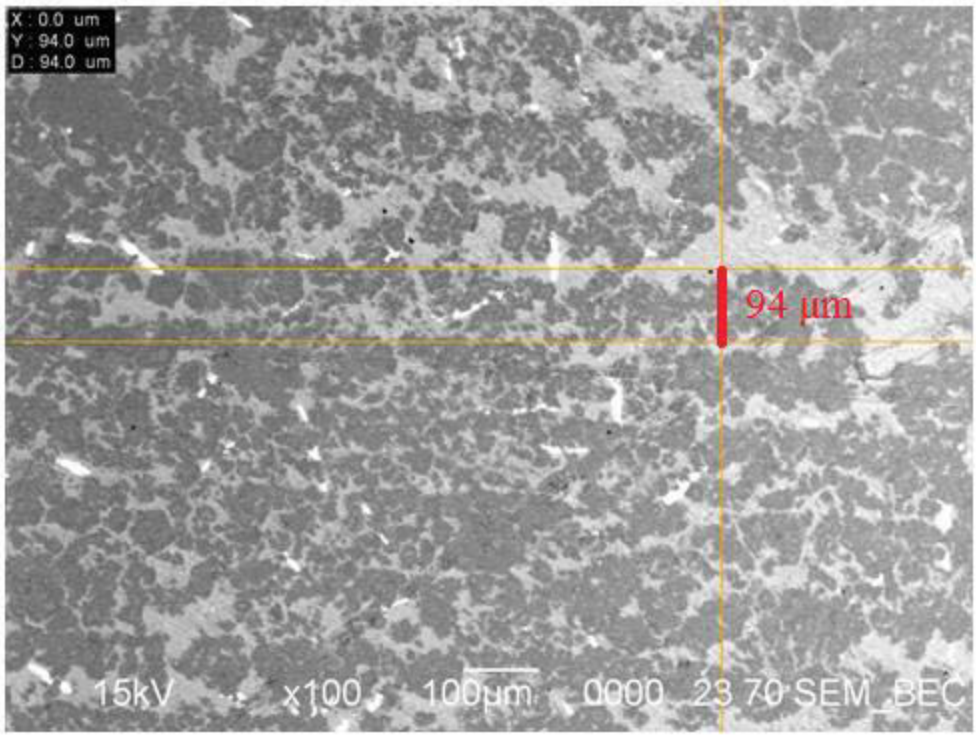

Figure 6.15: SEM image of C-spinel taken at 100x magnification showing a series of horizontal metal channels approximately 100 µm apart.

It is important to note that amorphous silica gel has adsorbent properties. Crystalline silica, in contrast, does not. So, when aqueous binder is dispersed during printing, each will behave differently. It is believed that the adsorbent nature of silica gel allows for more even and thorough distribution of binder throughout the pellet's entirety. It is also believed that crystalline silica does not allow that movement of binder. For that reason, the binder would exist as distinct, isolated layers in each pellet. A simplistic depiction of this is presented in Figure 6.16, as well as the effects of sintering and binder burnout.

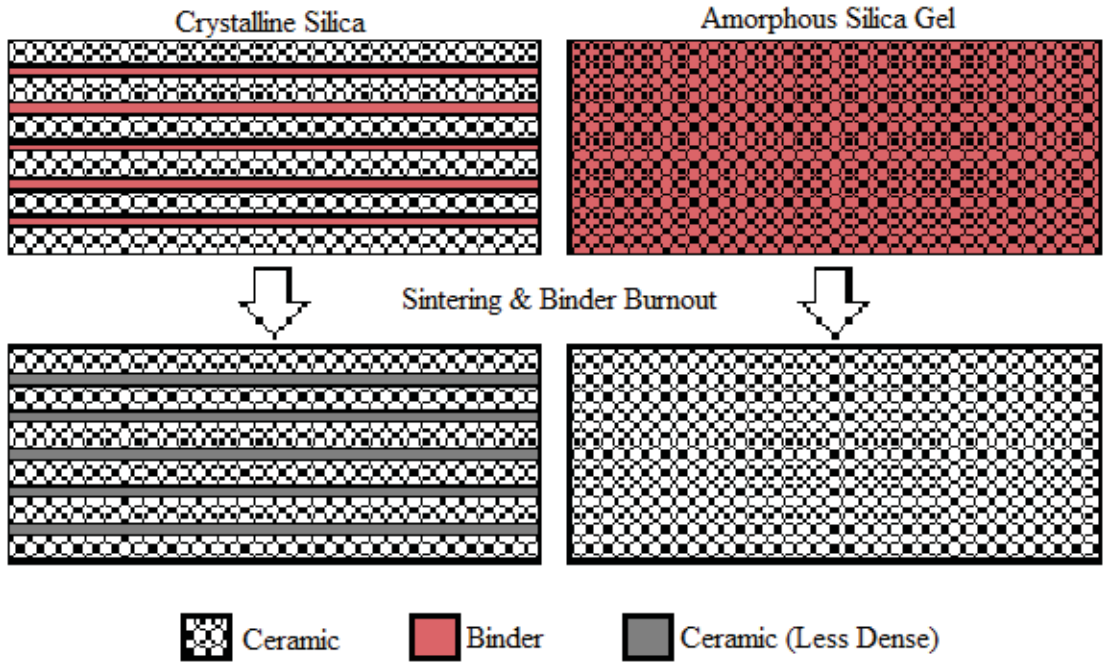

Figure 6.16: Effects of binder position before and after sintering in the 3-D printed C- and G-precursors.

Before a shaped powder is sintered, it is comprised of individual particulates. Then, at high temperatures, the edges of these particulates diffuse into their neighbors. The end result is a single cohesive shape. For this to happen, however, those particulates

must be in contact with one another. It is believed that the distinct layers of binder in a C-precursor limit contact between the particulates above and below them. Then, when sintering takes place, this limited contact creates regions of decreased density where binder used to be. The end result is a layered structure of alternating densities (Fig. 6.16). The regions of lower density produce the distinct metal channels seen in the C-spinels. The G-precursor, which allows for greater dispersion of binder with its adsorbent properties, does not have the same diminished contact between particulates as its C-counterpart. For that reason, sintering produces a more homogeneous preform. Then, during transformation, no parallel metal channels are formed.

In the end, crystalline silica was chosen for future work. For the ballistic and automotive applications of IPCs, larger ratios of ceramic to metal are required. The significantly higher density achieved by the C-precursors is considered more favorable, even if this yields linear channels of metal and ceramic in the final composite. It was these C-spinel composites that were subjected to mechanical properties testing.

The last topic to mention is the survivability of $MgAl_2O_4$/Al composites in the transformation process. Though fourteen pellets of G-precursor and twelve of the C-precursor were transformed, only two of the former and three of the latter survived the process. The rest either contained substantial cracks or had broken into multiple parts. This is believed to be a result of the transformation environment. The sample holder in all trials was silica, and subjected to the aluminum bath it became alumina. It is well known that magnesium aluminate likes to form on alumina, and the newly formed composites likely attached themselves to the alumina walls of the sample holder. Then, this attachment made removal from the metal bath difficult, resulting in the low survival rate.

In the future, different sample holders must be investigated. Silicon carbide, for example, poses no threat of reaction with the spinel. Using this, in theory, will increase the survival rate of the $MgAl_2O_4$/Al composites, allowing for more substantial investigation of their properties and microstructures.

6.2.3 Compressive Testing of C-Spinel IPCs

Three transformed pellets of the C-spinel were subjected to compressive testing on an Instron 5500R. Material load was plotted as a function of extension, and the compressive strength was determined for these composites. Though all samples were acquired from the same batch of 3-D printed pellets and transformed simultaneously, Table 6.3 displays the vastly different results acquired. Only Pellet 2 displayed the sudden brittle fracture one would expect from a ceramic-based composite (Fig. 6.17).

Pellet	Mass (g)	Height (mm)	Radius (mm)	Density (g/cm^3)	Maximum Load (N)	Compressive Strength (MPa)
1	2.17	7.24	6.57	2.21	25000	184
2	2.50	6.89	6.73	2.55	38000	267
3	2.46	7.70	6.59	2.34	28000	205

Table 6.3: Properties and results of C-spinel pellets subjected to compression testing.

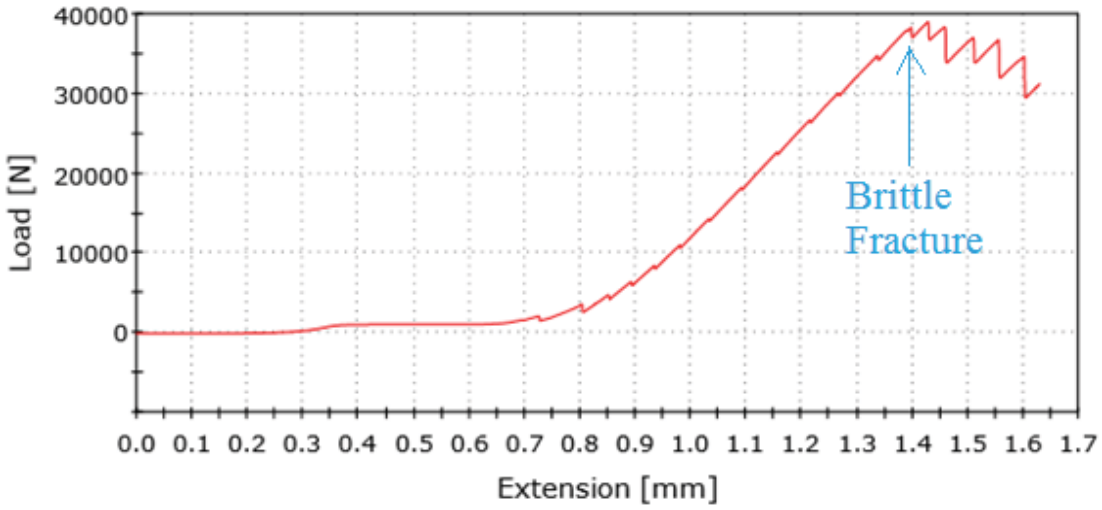

Figure 6.17: Graph of extension vs. load for Pellet 2 when subjected to compression testing.

At a sufficiently high load—38000 N, in this case—Pellet 2 suddenly fractured and the curve dropped off. In contrast, Pellets 1 (Fig. 6.18) and 3 (Fig. 6.19) experienced significant compression and deformation. No clear brittle fracture occurred, and the significant plastic deformation made determination of maximum load difficult. For this reason, the load at which each curve plateaued and switched from concave downward to concave upward was chosen. This is believed to be the point when the metal network starts holding the material together, as opposed to the ceramic matrix.

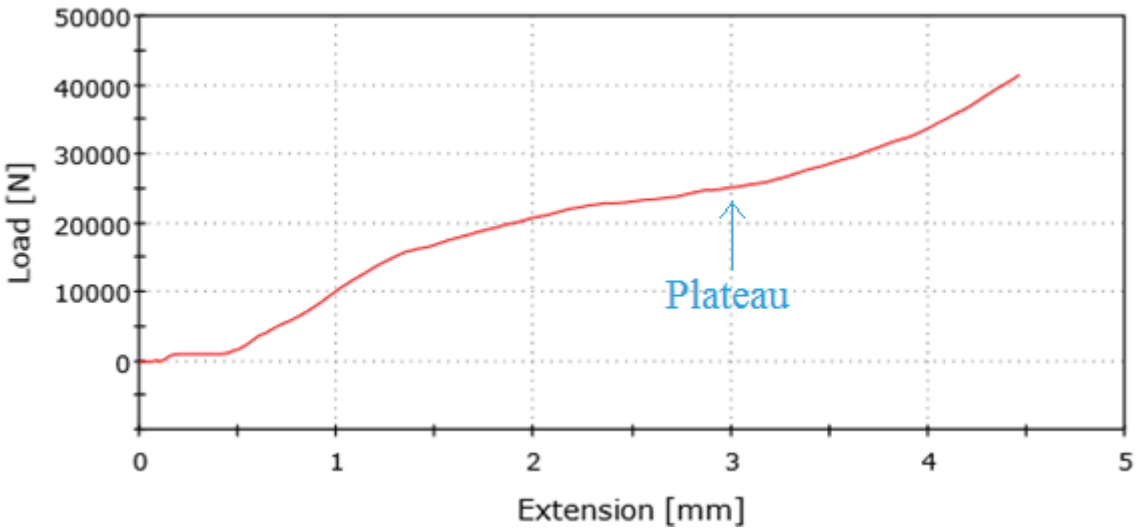

Figure 6.18: Graph of extension vs. load for Pellet 1 when subjected to compression testing.

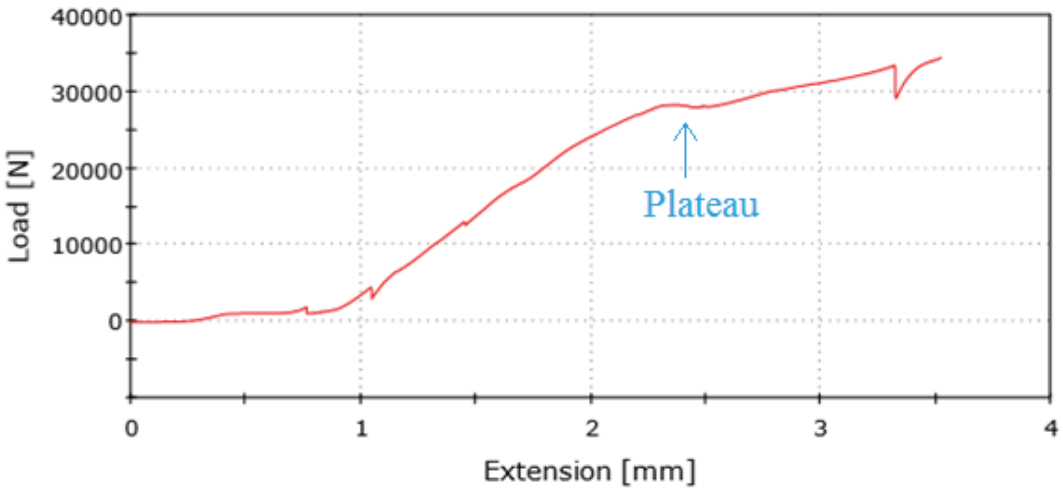

Figure 6.19: Graph of extension vs. load for Pellet 3.

The significant deformation occurring in Pellets 1 and 3 is particularly evident in Figure 6.20. There, one may see Pellet 1 after compression testing. The malleable nature of the metal network allowed large changes in the composites shape without separation into multiple parts. It also allowed for a greater degree of expansion, i.e. a more significant decrease in sample height.

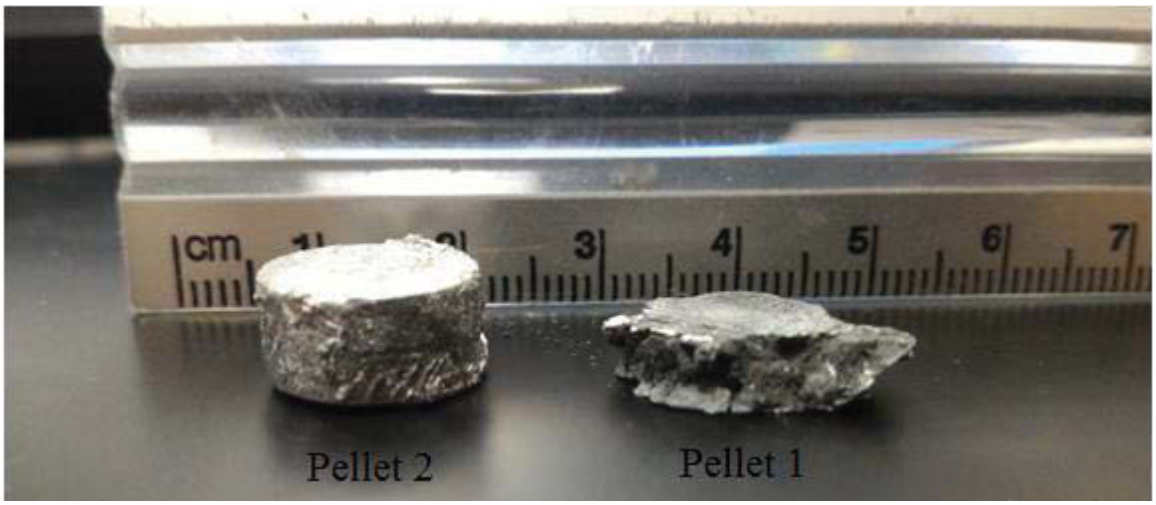

Figure 6.20: Pellet 1 after compressive testing. Compared to the unaltered shape of Pellet 2, it has undergone significant deformation without separation into multiple pieces.

The reasons Pellets 1 and 3 exhibited more metallic behavior than Pellet 1 is because they possessed a greater relative concentration of metal. The densities presented in Table 6.3 show this clearly. Spinel has a density of 3.57 g/cm^3, while that of aluminum is only 2.7 g/cm^3. It then stands to reason that larger concentrations of spinel create a denser composite. Pellet 2 possesses the highest density (2.55 g/cm^3), and was the only sample to display true brittle fracture. Its compressive strength was also the highest, at 196 MPa. Pellets 1 and 3—with densities of 2.21 and 2.34 g/cm^3, respectively—displayed metallic behavior because they contained greater concentrations of the lower density aluminum. The composite with the most metal, Pellet 1, also displayed the weakest compressive strength (184 MPa). These results further support the need to use crystalline silica when producing $MgAl_2O_4$/Al composites. A denser preform will produce a denser composite, and stronger compressive strengths will result.

6.2.4 Grain Boundaries

In Chapter 4, it was proposed that a cubic spinel and aluminum composite would possess better packing at the grain boundaries than one of aluminum and alumina. This is, of course, due to a cubic-on-cubic interface, as opposed to hexagonal-on-cubic. While only the $MgAl_2O_4$/Al composite was successfully created, its properties do support this hypothesis. To understand how, one may look to the SEM image presented in Figure 6.21. Three constituents are present in this image: $MgAl_2O_4$, Al, and Al-Si-Ti. One will notice that the interface between the two metal phases is clean and well-resolved. In contrast, the $MgAl_2O_4$/Al grain boundary is fuzzy and looks out of focus. Such fuzziness

was common amongst all SEM images presented thus far. Work done by Solomon and Moro may offer an explanation for this.

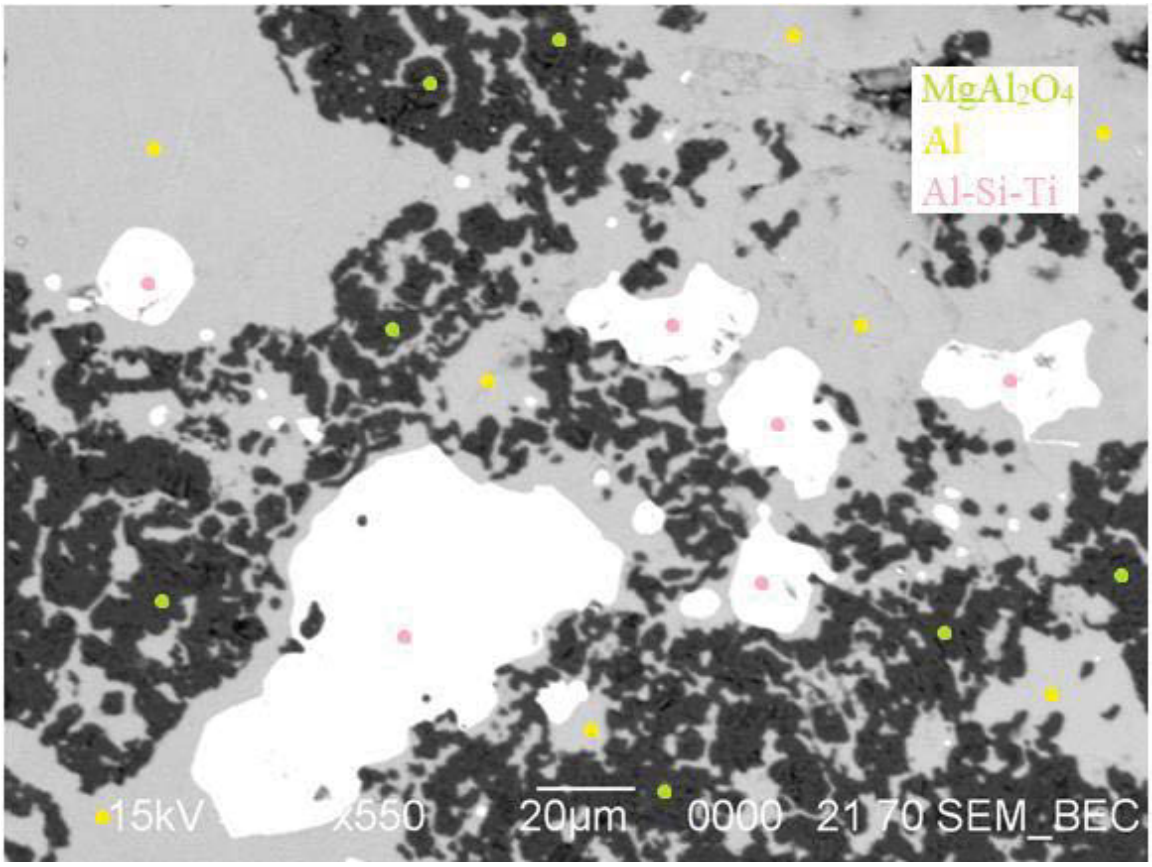

Figure 6.21: SEM image of a MgAl2O4/Al composite transformed in the tube furnace with a pure aluminum melt.

Working in collaboration with Fireline Inc., Solomon and Moro investigated an Al_20_3/Al-7.5 wt% Fe TCON composite [80]. Utilizing high resolution transmission electron microscopy, they assessed the interface between the Al and $Al_{13}F_4$ networks. There, they found an aluminum-silicon-iron boundary region (Fig. 6.22). This narrow interface region serves to accommodate the crystallographic differences between

hexagonal alumina and monoclinic aluminum-iron. It also gives the appearance of clear grain boundaries even at high magnifications.

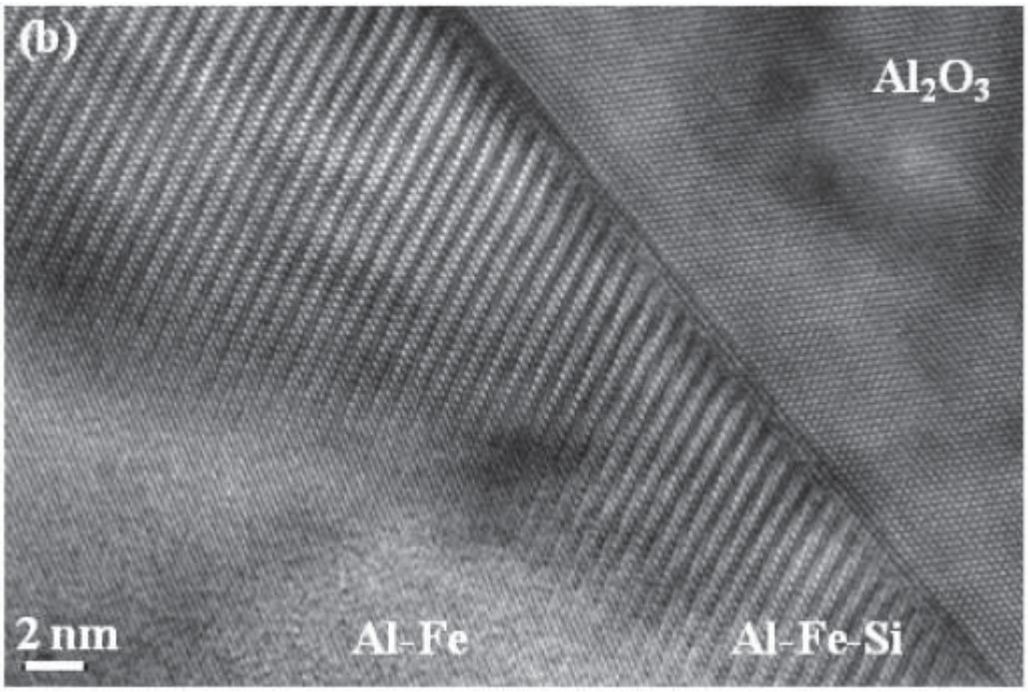

Figure 6.22: High resolution TEM image of the Al-Fe-Si boundary region in an $Al_20_3/Al_{13}Fe_4$ TCON composite [80].

Such a boundary region is believed to be absent in the $MgAl_2O_4$/Al composite. As both the ceramic and metal are cubic, there are no crystallographic differences to accommodate. Rather, the phases may meet and form a complex, faceted boundary. This would explain why the metal-metal interface is clear in Figure 6.21, but the ceramic-metal boundary is fuzzy. Such preliminary results do support the overall hypothesis of this thesis. Initial SEM images are consistent across all six composites investigated, regardless of reaction parameters or type of silica used. Significant transmission electron microscopy must be performed, however. This will best characterize the grain boundaries in composites of magnesium aluminate spinel and aluminum.

Chapter 7
Conclusions & Future Work

New ceramic-metal composites were created via reactive metal penetration and the TCON process. Initial precursor materials were shaped either by uniaxial pressing or 3-D printing, then immersed in a bath of aluminum with or without additional metals. This work was done in hopes of accomplishing three primary objectives:

1. Determine the effect of 3-D printing on the TCON process and resulting composites.
2. Incorporate cubic spinels—magnesium aluminate and aluminum oxynitride, specifically—into interpenetrating phase composites as the sole ceramic phase.
3. Compare the grain boundaries of an aluminum-alumina IPC to those contained in one of aluminum and a cubic spinel.

All objectives were—to an extent—achieved. There is, however, significant future work to be done and that will be discussed below.

In terms of the first objective, only a few 3-D printed precursors survived the TCON process. As a result, only a small number of $MgAl_2O_4$/Al IPCs were subjected to both scanning electron microscopy and mechanical properties testing. Moreover, only one shape—the pellet—was investigated. To better understand the affect 3-D printing has on IPCs, significantly more shapes must be printed and transformed. Beyond pellets, test bars and cubes should also be manufactured. After transformation, the pellets will undergo more substantial compressive testing. The test bars and cubes will be used for three point bending and determination of Young's Modulus respectively. As slip casting

is the standard method for shaping TCON precursors, $MgAl_2O_4$/Al composites must be produced from slip cast preforms with the same shapes and dimensions as those that were 3-D printed. Final composites may then be compared via mechanical properties testing and scanning electron microscopy. This will provide an effective method for determining how these different shaping methods affect final composite microstructure and strength.

While magnesium aluminate was successfully incorporated into IPCs as the sole ceramic phase, aluminum oxynitride failed to form. Reactive metal penetration of SiAlONs proved ineffective and this is attributed to an erroneous phase diagram, as well as temperature limitations during transformation. To overcome such flaws, a new synthesis is proposed in Reaction Scheme 7.1.

Reaction Scheme 7.1: $3SiO_2 + 2AlN + 4Al \rightarrow 2AlN + 2Al_2O_3 + 3Si$

A 3:2 molar ratio of silica and aluminum nitride may be combined into a precursor material. Then, when transformed in Fireline's kilns at 1200 ˚C, the silica becomes alumina. The AlN, in contrast, is an inert additive bound by the newly formed alumina and aluminum networks. After transformation, this composite will then be subjected to a secondary sintering under an inert atmosphere. Looking back to the AlON phase diagram in Chapter 6 (Fig. 6), it becomes clear that 1800 ˚C should be sufficient to fuse the alumina and aluminum nitride into the desired aluminum oxynitride phase (Reaction Scheme 7.2).

Reaction Scheme 7.2: $Al_2O_3 + AlN \rightarrow Al_3O_3N$

While this temperature is significantly above aluminum's melting point (660 ˚C), it is believed that little of the metal would vaporize during the secondary sintering. The small diameter of the metal ligaments, in theory, will prevent the loss of aluminum anywhere

but the sample's surface. Though more complicated than the original SiAlON method, this synthesis provides a unique alternative for future work.

To best prove the hypothesis that spinel/Al IPCs possess better packing at grain boundaries, significant transmission electron microscopy must be undertaken. Specifically, the ceramic-metal interfaces of Al_2O_3/Al and $MgAl_2O_4$/Al composites should be investigated by phase contrast TEM. This allows for imaging at near atomic levels, and will best show any voids and defects in atomic packing. Only by this method may the hypothesis be effectively proven.

Composites are an expansive and unique class of materials science. Here, unique interpenetrating phase composites were formed via reactive metal penetration and the TCON process. All three of the primary objectives were met to some extent, and the $MgAl_2O_4$/Al composites proved to be an interesting new material. Substantial work must still be done, however, before it may be used in the many ballistic, automotive, and refractory applications characteristic of interpenetrating phase composites.

References

1. Kaw, A. K. *Mechanics of Composite Materials*; Taylor & Francis: Boca Raton, FL, 2006.
2. Klement, R.; Rolc, S.; Mikulikova, R.; Krestan, J. Transparent Armour Materials. *Journal of the European Ceramic Society*. **2008**, *28*, 1091–1095.
3. History of Recent Science & Technology. Composites Overview. http://tinyurl.com/lgqnt5u (accessed Feb 27, 2015).
4. Wu, C.; Han, G. Synthesis of an Al_2O_3/Al Co-Continuous Composite by Reactive Melt Infiltration. *Materials Characterization*. **2007**, *58*, 416–422.
5. Liu, W.; Koster, U. Criteria for Formation of Interpenetrating Oxide-Metal Composites by Immersing Sacrificial Oxide Preforms in Molten Metals. *Scripta Materialia*, **1996**, *35*, 35-40.
6. Omatete, O.; Janney, M. Gelcasting: From Laboratory Development Toward Industrial Production. 1995.
7. Wang, N.; Wang, Z.; Weatherly, G. C. Formation of Magnesium Aluminate (Spinel) in Cast SiC Particulate-Reinforced Al(A356) Metal Matrix Composites. *MTA Metallurgical Transactions A*. **1992**, *23*, 1423–1430.
8. White, M. A. *Physical Properties of Materials*; CRC Press: Boca Raton, FL, 2012.
9. Breslin et al. Processing, Microstructure, and Properties of Co-Continuous Alumina-Aluminum Composites. *Materials Science and Engineering*, **1995**, *195*, 113-119.
10. del Rio et al. Co-Continuous Composites for High Temperature Applications. *Materials Science and Engineering*, **2007**, *463*, 115-121.
11. Kaczmar et al. The Production and Application of Metal Matrix Composite Materials. *Journal of Materials Processing Technology*, **2000**, *106*, 58-67.
12. Daehn, et al. Elastic and Plastic Behavior of a Co-Continuous Alumina/Aluminum Composite. *Acta Materialia*. **1996**, *44*, 249–261.
13. Hoffman et al. Fracture Behaviour in Metal Fibre Reinforced Ceramics. *Acta Materialia*. **1997**, *45*, 3609–3623.
14. Mattern et al. Preparation of Interpenetrating Ceramic-Metal Composites. *Journal of the European Ceramic Society*, **2004**, *24*, 3399-3408.
15. San Marchi et al. Alumina–Aluminum Interpenetrating-Phase Composites with Three-Dimensional Periodic Architecture. *Scripta Materialia*. **2003**, *49*, 861–866.
16. Murthy et al. Orientation and Grain Boundary Microstructure of Alumina in Al/Al_2O_3 Composites Produced by Reactive Metal Penetration. *Journal of the American Ceramic Society J American Ceramic Society*. **2005**, *88*, 2902–2907.
17. Vecchia et al. Co-Continuous Al/Al_2O_3 Composite Produced by Liquid Displacement Reaction: Relationship Between Microstructure and Mechanical Behavior. *Journal of Materials Science*, **2003**, *38*, 3567-3577.
18. Saiz, E.; Tomsia, A.P. Kinetics of Metal-Ceramic Composite Formation by Reactive Metal Penetration of Silicates with Molten Aluminum. *Journal of the American Ceramic Society*, **1998**, *81*, 2381-2393.
19. Yamanaka et al. Influence of Preform Preparation Condition on Infiltration of Molten Aluminum. *Journal of Material Processing Technology*, **2007**, *187*, 530-532.

20. Peters et al. Advanced Ceramic Composites for Improved Thermal Management in Molten Aluminum Applications. *The Minerals, Metals & Materials Society*, **2009**, 241-247.
21. Wegner, L.; Gibson, L. The Mechanical Behaviour of Interpenetrating Phase Composites – I: Modelling. *International Journal of Mechanical Sciences*. **2000**, *42*, 925–942.
22. Henri, G. Manufacture of Articles from Substances Containing Silica. Patent No. 2702750, Feb. 22, 1955.
23. Li, J.-G. Wetting of Ceramic Materials by Liquid Silicon, Aluminium and Metallic Melts Containing Titanium and Other Reactive Elements: A Review. *Ceramics International*. **1994**, *20*, 391–412.
24. Naga et al. Properties of Ceramic-Metal Composites Formed by Reactive Metal Penetration. *American Ceramic Society Bulletin, 86*, 9301-9307.
25. Newkirk, M.S.; Dizio, S.F. Novel Ceramic Materials and Methods for Making Same. Patent No. 4713360, Sept. 17, 1985
26. Chidambaram et al. A Thermodynamic Criterion to Predict Wettability at Metal-Alumina Interfaces. *Metallurgical Transactions*, **1992**, *23*, 215-222.
27. Avraham, S.; Kaplan, W.D. Reactive Wetting of Rutile by Liquid Aluminum. *Journal of Materials Science*, **2005**, *40*, 1093-1100.
28. Delannay et al. The Wetting of Solids by Molten Metals and its Relation to the Preparation of Metal-Matrix Composites. *Journal of Materials Science*, **1987**, *22*, 1-16.
29. Zhou, X.; Hosson, J. D. Reactive Wetting of Liquid Metals on Ceramic Substrates. *Acta Materialia*. **1996**, *44*, 421–426.
30. Eustathopoulos, N. Dynamics Of Wetting in Reactive Metal/ Ceramic Systems. *Acta Materialia*. **1998**, *46*, 2319–2327.
31. Kaiser, A.; Lutz, R. Uniaxial Hydraulic Pressing as Shaping Technology for Advanced Ceramic Products of Larger Size. http://tinyurl.com/htzuocy.
32. Current Status of Ceramic Injection Moulding, http://tinyurl.com/hn3kgkw (accessed Apr 21, 2016).
33. Stanimirović, Z; Stanimirović, I. Ceramic Injection Molding. *Intech*. http://tinyurl.com/h3c4lrf (accessed May 1, 2016).
34. Multi-mold Precision Industry Co.,Ltd., http://www.multi-mold.com/moldtech.asp (accessed Apr 25, 2016)
35. Slip Casting. Swerea IVF Product Sheet. *www.swerea.se/en/file/1070/download?token=COxLr4Rf*
36. Smith, W. F. *Principles of Materials Science and Engineering*; McGraw-Hill: New York, 1990.
37. Slip Casting. Encyclopedia Britannica Online, http://www.britannica.com/technology/slip-casting (accessed Apr 25, 2016).
38. Gilissen et al. Gelcasting, a Near Net Shape Technique. *Materials & Design*. **2000**, *21*, 251–257.
39. Hotza, D.; Greil, P. Review: Aqueous Tape Casting of Ceramic Powders. *Materials Science and Engineering: A*. **1995**, *202*, 206–217.
40. Comparison of Different Shaping Technologies for Advanced Ceramics Production. ResearchGate, http://tinyurl.com/zp5haz6 (accessed Apr 21, 2016).

41. Mason, T. O. Advanced Ceramics. Encyclopedia Britannica Online, http://www.britannica.com/technology/advanced-ceramics (accessed Apr 25, 2016).
42. Typical Forming Process of Fine Ceramics. http://global.kyocera.com/fcworld/first/process04.html (accessed Apr 25, 2016).
43. Revolutionary Additive Manufacturing: An Overview. Academia.edu, http://www.academia.edu/12462648/revolutionary_additive_manufacturing_an_overview (accessed Apr 21, 2016).
44. Withell et al. Porous Ceramic Filters through 3D Printing. *Proceedings of the 5th International Conference on Advanced Research in Virtual and Rapid Prototyping, Leiria, Portugal, 28 September - 1 October, 2011 Innovative Developments in Virtual and Physical Prototyping*. **2011**, 313–318.
45. Low-Cost 3D Printing of Controlled Porosity Ceramic Parts. *International Journal of Automation Technology IJAT*. **2012**, *6*, 618–626.
46. Wong, K. V.; Hernandez, A. A Review of Additive Manufacturing. A Review of Additive Manufacturing, http://www.hindawi.com/journals/isrn/2012/208760/ (accessed Apr 21, 2016).
47. Solid Freeform Fabrication Proceedings, https://idc.sutd.edu.sg/wp-content/uploads/sites/10/2015/04/2004-solid-freeform-fabrication-proceedings.pdf (accessed Apr 21, 2016).
48. CUSTOMPART. 3D Printing. http://www.custompartnet.com/wu/3d-printing (accessed April 25, 2015).
49. Silva, V. D. da. *Mechanics and Strength of Materials*; Springer: Berlin, 2006.
50. Green, D. J. *An Introduction to the Mechanical Properties of Ceramics*; Cambridge University Press: Cambridge, 1998.
51. Farrar, R. A. *The Mechanical Properties of Materials*; Methuen Educational: London, 1971.
52. Roylance, D. Stress-Strain Curves, http://tinyurl.com/79jxtbl (accessed Apr 25, 2016).
53. Wilkins, M. L. Mechanics of Penetration and Perforation. *International Journal of Engineering Science*. **1978**, *16*, 793–807.
54. Davidge, R. W. Strength and Toughness in Ceramic Systems. *Phil. Trans. R. Soc.* **1983**, *310*.
55. Aksel, C.; Riley, F. L. Young's Modulus Measurements of Magnesia–Spinel Composites Using Load–Deflection Curves, Sonic Modulus, Strain Gauges and Rayleigh Waves. *Journal of the European Ceramic Society*. **2003**, *23*, 3089–3096.
56. Lundberg et al. Impact of Metallic Projectiles on Ceramic Targets: Transition between Interface Defeat and Penetration. *International Journal of Impact Engineering*. **2000**, *24*, 259–275.
57. Hansen, N. Hall–Petch Relation and Boundary Strengthening. *Scripta Materialia*. **2004**, *51*, 801–806.
58. Hansen, N. The Effect of Grain Size and Strain on the Tensile Flow Stress of Aluminium at Room Temperature. *Acta Metallurgica*. **1977**, *25*, 863–869.
59. Krell et al. Advanced Spinel and Sub-mm Al_2O_3 for Transparent Armour Applications. *Journal of the European Ceramic Society*. **2009**, *29*, 275–281.

60. Bhaduri, S.; Bhaduri, S. Microstructural and Mechanical Properties of Nanocrystalline Spinel and Related Composites. *Ceramics International*. **2002**, *28*, 153–158.
61. PA347 Grain Boundaries
62. Prielipp et al. Strength and Fracture Toughness of Aluminum/Alumina Composites with Interpenetrating Networks. *Materials Science and Engineering: A*. **1995**, *197*, 19–30.
63. Sigl et al. On The Toughness of Brittle Materials Reinforced with a Ductile Phase. *Acta Metallurgica*. **1988**, *36*, 945–953.
64. Myers, K. (2011) Investigation of Novel Precursor Routes for Incorporation of Titanium Alloys and Nano-Sized Fractures into Ceramic-Metal Composites Formed via the TCON Process. Master's Thesis, Youngstown State University, OH, U.S.A.
65. Denmeade, J. (2013) Investigation of Novel Precursor Routes for Incorporation of Oxynitride Spinel Phases into Ceramic-Metallic Composites Formed via the TCON Process. Master's Thesis, Youngstown State University, OH, U.S.A.
66. Tessier et al. Nanocrystalline β-Sialon by Reactive Sintering of a SiO_2–AlN Mixture Subjected to High-Energy Ball Milling. *Journal of Alloys and Compounds*. **2005**, *391*, 225–227.
67. Pichlbauer et al. Preparation of -sialon Bonded Al_2O_3-Refractories in Different Atmospheres. *Ceramic Materials.* **2011**, *1*, 11-15.
68. The Symmetry of Crystals. Bravais lattices http://www.xtal.iqfr.csic.es/cristalografia/parte_03_4-en.html (accessed Jun 7, 2016).
69. X-ray Powder Diffraction (XRD) http://serc.carleton.edu/research_education/geochemsheets/techniques/xrd.html (accessed Jun 7, 2016).
70. Powder X-ray Diffraction http://chemwiki.ucdavis.edu/core/analytical_chemistry/instrumental_analysis/diffraction/powder_x-ray_diffraction (accessed Jun 7, 2016).
71. What is Powder Diffraction? http://pd.chem.ucl.ac.uk/pdnn/powintro/powdiff.htm (accessed Jun 7, 2016).
72. Brief Review of Structure in Materials. http://nptel.ac.in/courses/113104005/lecture1/1_9.htm (accessed May 1, 2016).
73. Crystal Geometry Equations for XRD. Princeton. http://tinyurl.com/honfqqx (accessed May 2, 2016).
74. Goldstein, J. *Scanning Electron Microscopy and X-Ray Microanalysis*; Kluwer Academic/Plenum Publishers: New York, 2003.
75. Leng, Y. *Materials Characterization: Introduction to Microscopic and Spectroscopic Methods*; J. Wiley: Singapore, 2008.
76. Brief Introduction to Scanning Electron Microscopy (SEM). University of California, Merced, http://cfamm.ucr.edu/documents/sem-intro.pdf (accessed Apr 22, 2016).
77. Hafner, B. Scanning Electron Microscopy Primer. University of Minnesota. http://www.charfac.umn.edu/sem_primer.pdf (accessed May 1, 2016).
78. Microscopy. Canadian Center for Welding + Joining, http://www.ualberta.ca/~ccwj/teaching/microscopy/ (accessed May 1, 2016).

79. Mccauley et al. AlON: A Brief History of its Emergence and Evolution. *Journal of the European Ceramic Society* **2009**, *29* (2), 223–236.
80. Solomon, C. V. et al. High Resolution Electron Microscopy and Crystallographic Analysis of the Ceramic/Metal Interface in an Al2O3/Al-7.5 Wt% Fe Composite Produced by Reactive Metal Penetration. *Proceedings of ALC'13*.